Spectral Decomposition of Wavelength Dispersive X-Ray Spectra: Implications for Quantitative Analysis in the Electron Probe Microanalyzer

G. Remond
Bureau de Recherches Géologiques et Minières, France

J. L. Campbell
University of Guelph, Ontario

R. H. Packwood
CANMET-EMR, Ontario

M. Fialin
Université P. et M. Curie, Paris

Utah State University
MERRILL-CAZIER LIBRARY

SPECTRAL DECOMPOSITION OF WAVELENGTH DISPERSIVE X-RAY SPECTRA:
IMPLICATIONS FOR QUANTITATIVE ANALYSIS IN THE ELECTRON PROBE MICROANALYZER

G. Remond[*,1], J.L. Campbell[2], R.H. Packwood[3] and M. Fialin[4]

[1]Bureau de Recherches Géologiques et Minières, Orléans, France
[2]College of Physical and Engineering Science, University of Guelph, Guelph, Ontario, Canada
[3]Metals Technology Laboratories, CANMET-EMR, Ottawa, Ontario, Canada
[4]URA 736 - CNRS , Université P. et M. Curie, Paris, France

Abstract

The line shapes of $K\alpha$, $L\alpha,\beta$ and $M\alpha$ X-ray peaks of pure elements were analyzed by means of commercial wavelength dispersive spectrometers (WDS) attached to an electron probe micro-analyzer (EPMA). A pseudo-Voigt function, i.e., a linear combination of Gaussian and Lorentzian distributions, was used as a fitting profile for the X-ray peaks, with Gaussian offsets incorporated in the short wavelength (high energy) side to describe the observed asymmetry.

The asymmetry of X-ray peaks resulting from both instrumental distortions and satellite bands may lead to discrepancies in quantitative analysis with the EPMA as a function of the procedure used for deriving X-ray intensities from WDS spectra, e.g., peak height, peak area, or peak decomposition. These effects have been illustrated by analyzing gold-copper metallic alloys and minerals containing gold at trace levels.

Key Words: Diagram lines, non-diagram lines, multiple ionizations, Coster-Kronig transitions, self-absorption, Johann mounting, focusing defects, peak height, peak area, peak decomposition.

*Address for correspondence:
G. Remond,
B.R.G.M. - Département DR/GGP,
B.P. 6009
45060 Orléans, France

Phone number: 33 38 64 31 23
FAX number: 33 38 64 39 25

Introduction

The modern computer-controlled electron probe micro-analyzer (EPMA) for spatially resolved chemical analysis by X-ray spectrometry (XRS) offers capabilities for repetitive analyses on a routine basis in a variety of materials. Using wavelength dispersive spectrometers (WDS), it is usually accepted to measure the intensity of an X-ray emission as the peak height of the emission line. The net intensity is obtained by measuring the total number of counts for the monochromator set at the Bragg angle corresponding to the analyzed emission, followed by changing the monochromator position to measure the continuous emission occurring on each side of the peak. The approach based on X-ray peak height measurement in WDS analysis has been proved experimentally to be sufficient for quantitative analysis of major constituents in a variety of materials. This approach remains valid only as long as the peak height remains proportional to the integrated peak area and as long as no chemical peak shift exists between the X-ray emission line measured at the surface of the specimen and the reference material successively. Thus, the peak height intensity measurement is more particularly questionable for the case of soft X-rays such as L X-ray emission spectra of first series transition elements and K X-ray emission spectra of low atomic number elements. For these soft X-rays, valence electrons are involved in the X-ray radiative transitions, and the observed X-ray peak shapes and positions will reflect the electronic structure of the compound containing the analyzed elements.

In practice, with the EPMA, in order to account for a possible departure of peaks from symmetry, it is possible to use area/peak factors (APF) which permit the transformation of conventional peak height measurements into area measurements. This is equivalent to measuring areas as described by Bastin and Heijligers [3, 4] and by Pouchou and Pichoir [56]. Empirical correction factors are also commonly used in the presence of peak overlaps as discussed by Roeder [66] for the case of the analysis of rare-earth bearing compounds.

To be corrected by the use of predetermined coefficients, the raw intensities must be acquired with the same instrumental and experimental conditions as used for determining the coefficients. In addition, for the case of the analysis of soft X-rays, these coefficients characterizing the peak profile are dependent on the matrix and must be determined for each analyzed element in a variety of compounds. Recalibration procedures during quantitative analysis may be used for correcting peak shifts resulting from instrumental factors or from chemical binding effects. Marion and Vannier [48] have suggested that two successive measurements on each side of the expected peak maximum should be made and the actual peak maximum be derived from a theoretical description of the peak around its maximum. They showed that this procedure accounted for small non-reproducibilities in the monochromator positioning or for small chemical shifts but did not account for large peak shape changes between X-ray spectra such as those reported by Fialin *et al.* [26], by Solberg [76] for the case of the F Kα emission peak in a variety of minerals, and by Fialin [24] and Remond *et al.* [63] for the case of Zn Lα in pure zinc, zinc oxide and zinc sulfide.

For the reasons mentioned above, peak area measurement or multiple least squares fitting techniques to process digitally recorded wavelength dispersive spectra should be preferred to peak height measurement. Using modern computer controlled EPMAs, peak area can be easily achieved by integrating the number of counts in each successive channel analyzed by displacing the monochromator step by step. However, this procedure does not allow one to separately treat the instrumental factors and the physical mechanisms producing the observed X-ray peak profile.

Modern EPMAs are generally equipped with spectrometers having crystal monochromators of the Johann type. With this mounting, the focusing conditions are not satisfied over the total surface of the bent crystal. The response function (or diffraction pattern) from a curved crystal has been discussed by Cauchois and Bonnelle [14], and the origins of focusing defects leading to pronounced asymmetry on the short wavelength side of X-ray peaks (occurring at low Bragg angles) are summarized in **Appendix**.

An X-ray emission line (or diagram line) resulting from a transition between two levels in the energy-level diagram is frequently accompanied by satellites (or non-diagram lines), i.e., X-ray lines whose energies do not correspond to the difference of two energy levels. The satellite lines have weak intensities and occur generally on the high energy side of the diagram emission line, i.e., on the short wavelength side of the peak. These satellite lines have been intensively studied since the 1930's-1940's, beginning with the detailed works of

Parratt [54, 55] and Randall and Parratt [59]. The origins of satellite lines resulting from electronic rearrangement concomitant with the ionization process and during the de-excitation mechanisms of the ionized atoms have been recently reviewed [11, 23, 35] and are summarized in **Appendix**.

Depending upon the origins of the satellite lines, their energy separation distances from their parent diagram lines may range from a few eV to a few hundreds of eV, and they may have weak intensities. The contribution of the satellite lines to the observed X-ray peak profile will depend on the energy resolution and sensitivity of the spectrometer used. In addition, the small satellite features may sometimes be hidden by instrumental distortion as a function of the energy (wavelength) of the analyzed X-ray emission lines. Although the energy resolution of an energy dispersive spectrometer (EDS) is very poor with respect to the natural width of X-ray lines, it has been shown that instrumental factors leading to distortions on the low energy side of peaks as well as low energy radiative Auger contributions must be added to the fitting function used to derive reliable intensities from EDS spectra [12, 13]. It has also been shown [44, 45] that the contribution of satellite lines to the total intensity of an X-ray emission line cannot be neglected when calculating theoretical X-ray intensities to be used in a standardless method for EDS microanalysis [44, 45, 56, 57].

The resolution of a commercial WDS attached to EPMAs is intermediate between an EDS and high resolution spectrometers based on double monochromators or gratings which are used for accurate analyses of satellite lines. **It is the objective of this paper to discuss how instrumental factors and satellite lines may affect WDS X-ray peak profiles and consequently may lead to inaccurate data because of the possible non-proportionality between the measured X-Ray intensity and the number of emitting atoms as a function of the procedure used to derive X-ray intensities from experimental spectra**.

It is also the purpose of this paper to investigate the line shape of K, L and M X-ray peaks obtained with an automated EPMA equipped with WDS's. The observed width of X-ray peaks from pure elements will be discussed taking into account the intrinsic resolution of the spectrometer and the natural width of the analyzed emission lines, respectively. Departure of peaks from symmetry, resulting from the presence of tailing effect on the short wavelength side (high energy side of peaks), will be discussed in terms both of spectral distortions resulting from instrumental factors and of the existence of non-diagram lines. The non-diagram bands isolated from WDS X-ray spectra will be compared with experimental and theoretical data on X-ray emission

mechanisms occurring in the presence of multiple vacancy configurations. The dependence of the intensity of high energy satellites upon the specimen composition will also be illustrated and discussed as a function of the procedure used for X-ray peak intensity measurements in quantitative analysis with the EPMA, i.e., peak height, peak area and peak decomposition. Examples of analyses of Cu-Au alloys and minerals containing gold at trace levels will be given.

Methods and Materials

Instrumentation

The computer and microprocessor controlled Cameca microprobes (Camebax Microbeam and SX 50) installed at the joint Bureau de Recherches Géologiques et Minières (BRGM)-Centre National de la Recherche Scientifique (CNRS) laboratory were used. The monochromators mounted on the spectrometers are of the **Johann type**, i.e., the plane crystal is simply cylindrically bent to twice the focal circle radius.

First and second reflection orders of K, L and M emission lines were analyzed by means of a **LiF** (200), a **PET** (002), a **TAP** ($10\bar{1}1$) and a W/Si multilayer monochromator. When possible, the same X-ray peak was analyzed using two different monochromators in order to show the dependence of the peak profiles upon the Bragg angle. Pure elements, natural sulfides and gold-copper alloys were analyzed.

The X-ray peaks of interest were digitally recorded moving the monochromator step by step. For each channel the counting time was one second. For studying peak shape profiles, the electron beam intensity was adjusted in order to have similar statistical precision for most of the analyzed peaks. Before displaying the X-ray peaks, the measured intensity in each channel was corrected for dead time.

For some of the measurements, a **quartz** monochromator ($10\bar{1}1$ planes) was installed in **the Johansson mounting**. In this mounting, the crystal is first ground with a radius of curvature equal to that of the focusing circle and then bent to a radius of twice that value. For this purpose, the Cameca MS 46 instrument at the Ecole Nationale Supérieure de Mécanique et des Microtechniques in Besançon (France) was used. The characteristics of the Johann and Johansson mounting types are summarized in the **Appendix**.

Spectra Processing

The line shape of a WDS X-ray peak is generally intermediate between a Gaussian and a Lorentzian distribution. The observed peak profile, $P(\lambda)$, was described by a pseudo-Voigt function, i.e., a linear combination of a Gaussian and a Lorentzian distribution:

$$P(\lambda) = C_g\, G(\lambda) + C_l\, L(\lambda), \qquad (1)$$

where $O < C_g < 1$ and $C_l = 1 - C_g$ are the contributions of the Gaussian $G(\lambda)$ and Lorentzian $L(\lambda)$ of same half-width and centered at the same position [50, 60].

When studying X-ray peaks from pure elements or elements present with high concentrations in compounds, the intensity of the continuous emission underlying the analyzed X-ray peaks was approximated by a linear function. When analyzing for elements present at low concentrations, the continuous emission distribution was treated.

The X-ray emission diagram lines are presumed to be symmetrical. In order to correct the excess width resulting from tails occurring either on the low or the high energy side of peaks, one approach consists of subtracting the mirror image of the high energy side (or low-energy side) from the low (or high) energy side. Subtracting the mirror image of one side of the peak is only feasible in the absence of peak overlap and when the peak profile is perfectly known. In other words, this approach is only applicable when a spectrometer of very high resolution is used. In such a case, the emission lines may be described by a pure Lorentzian.

Automated EPMAs are equipped with monochromators having energy resolution broader than the intrinsic width of the analyzed X-ray lines. Thus, unless the response function of the spectrometer is accurately known, the method based on subtracting the mirror image of one side of the peak from the other cannot be applied to extract fine structures from peaks.

Similarly, unless the origin of the observed satellites or tails is physically identified, the analytical description of these features can only be empirical. In order to account for departure from symmetry of the peaks, Huang and Lim [34], using equation 1 as the fitting function, varied the half-width of the Gaussian and Lorentzian distributions with respect to the maximum peak position. This approach, which is very close to that of subtracting the mirror image of half a peak, requires that the C_g and C_l coefficients in equation 1 be already determined.

We used an approach consisting of empirically adding Gaussian offset(s) to equation 1. In order to reduce the number of variables in the fitting procedure some parameters were coupled to others. For this purpose, the α_2-α_1 separation distance and the relative intensity of these two components were set at their theoretical values. X-ray energies were obtained from the data of Doyle *et al.* [22] or calculated as binding energy differences. The $K\alpha_2/K\alpha_1$ and $L\alpha_2/L\alpha_1$ intensity ratios were derived from data of Scofield [72, 73]. The $M\alpha_2/M\alpha_1$ intensity ratios were obtained from Chen and Crasemann [17]. For each analyzed peak, the fitting procedure was conducted by varying the value of the C_g and C_l

coefficients in equation 1 until the best quality of fit was obtained. The adjustment of fit of the experimental data to the model function was done with an automated fitting program developed by Massiot [50], minimizing the root-mean-square deviation (SD):

$$SD = [\Sigma\{P'(\lambda_i)^2 - P(\lambda_i)^2\}^{1/2}] / n, \qquad (2)$$

where n is the number of data points, $P'(\lambda_i)$ is the number of counts at channel i, and $P(\lambda_i)$ is the value of the model function at that point i. The method utilized an iterative non-linear least-squares fitting process **starting from an initial estimated solution.**

Examples of High Energy Non-Diagram Lines

General results

In order to illustrate the change in the peak shape as a function of the analyzed radiative transition, the S Kα, Nb Lα and Au Mα emission lines, whose energies are similar (2.308 keV, 2.166 keV, and 2.123 keV, respectively), were digitally recorded and processed. These X-ray peaks were analyzed using a PET (002) monochromator. The corresponding Bragg angles for the first order reflection were located midway within the Bragg angle domain imposed by the mechanical limitations of the monochromator displacement within the spectrometer.

As shown in Figure 1, the S Kα, Nb Lα and Au Mα peaks exhibited satellite peaks and asymmetrical shape on their short wavelength side.

The S $K\alpha_{1,2}$ doublet: As shown in Figure 1a, the unresolved S $K\alpha_{1,2}$ peaks are accompanied by a peak of small intensity whose wavelength does not correspond to a diagram line and was assigned to a satellite line labelled S KL. Assuming that the S $K\alpha_1$ and S $K\alpha_2$ diagram peaks are symmetrical, the best fit was obtained for $C_g = 0.6$ in equation 1. The residuals between the calculated and the experimental data showed the existence of a second satellite peak labelled S KX. Each of the satellite peaks was described by a Gaussian offset in the fitting function. The separation distance between the satellite peaks and the S $K\alpha_1$ peak was 0.00348 nm (15 eV) and 0.000865 nm (3.7 eV), respectively.

The Nb $L\alpha_{1,2}$ peaks: The unresolved Nb $L\alpha_{1,2}$ peaks (Fig. 1b) also exhibited an asymmetrical shape. The high energy tail was described by the sum of two Gaussian offsets Nb $L\alpha S_1$ and Nb $L\alpha S_2$, respectively. The separation distances of these bands from the Nb $L\alpha_1$ diagram line were 0.00202 nm (7.6 eV) and 0.00430 nm (16 eV), respectively. The best fit was obtained for $C_g = 0.4$ in the fitting function.
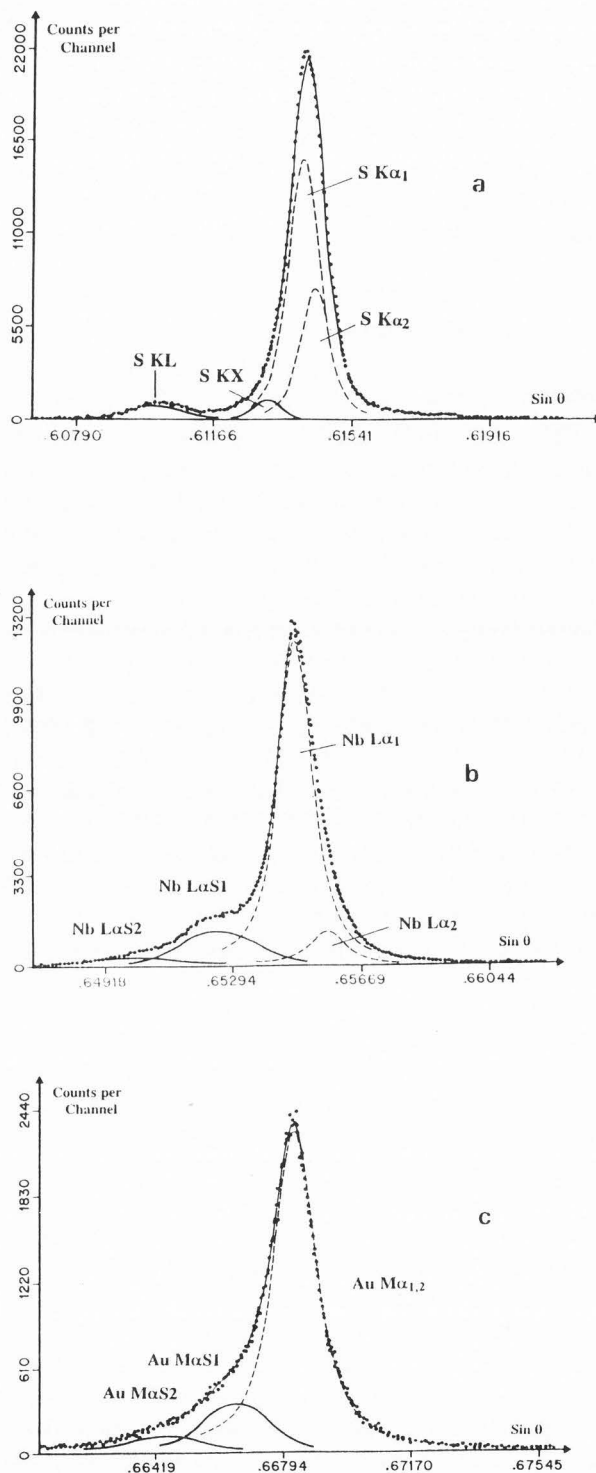

Figure 1. Results of fitting to the S Kα (**a**), Nb Lα (**b**) and Au Mα (**c**) spectral peaks. All have similar energies and were analyzed with a PET (002) monochromator (from ref. [57]).

92
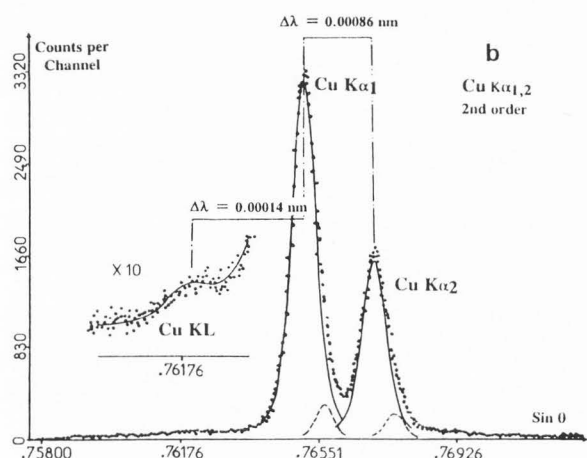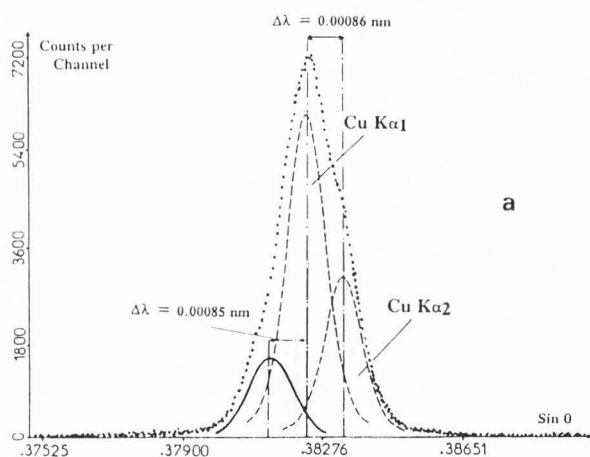
Figure 2. Results of fit to the Cu $K\alpha_{1,2}$ emission peaks analyzed with the LiF (200 planes) monochromator: (**a**) first order reflection, and (**b**) second order reflection.

The Au $M\alpha_{1,2}$ Peaks: The Au $M\alpha$ peak (Fig. 1c) exhibited a long tail on its short wavelength side. The residual between the total peak and the Au $M\alpha$ diagram line exhibited a strongly asymmetrical feature which was described by the sum of two Gaussian offsets. The separation distance between the maximum of this non-diagram emission band and the Au $M\alpha$ peak was 5.6 eV. The best fit to experimental data was obtained by setting $C_g = 0.30$ in equation 1.

The small features observed on the high energy side of the S $K\alpha$, Nb $L\alpha$ and Au $M\alpha$ peaks most probably resulted from the existence of non-diagram lines rather than instrumental effects associated with the mounting of the monochromator within the spectrometer. The effect of the Bragg angle upon the observed line shape is illustrated in Figures 2 and 3 for the case of the first and
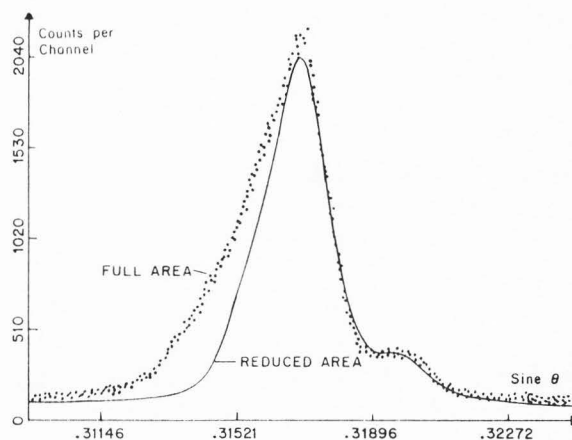
Figure 3. Line shape of the Au $L\alpha_{1,2}$ peaks analyzed using the full area of a LiF (200 planes) monochromator and after reducing the active area of the same monochromator (the LiF crystal is of the Johann type).

---

second order reflections of the Cu $K\alpha_{1,2}$ and Au $L\alpha_{1,2}$, respectively, when analyzed with the LIF (200) monochromator.

As shown in Figure 2a, the Cu $K\alpha_{1,2}$ peak occurring in first order reflection (at a Bragg angle $\theta = 22.5°$) is asymmetrical. The tail on the short wavelength side of the $K\alpha_{1,2}$ doublet was described by adding a Gaussian offset to the fitting function. The quality of the fit was greatly improved by adding two Gaussian offsets describing the long wavelength (low energy) tails of the $K\alpha_1$ and $K\alpha_2$ peaks. As shown in Figure 2b for the second order reflection (at $\theta = 45°$), no additional Gaussian was required to describe the short wavelength side of the peaks. However, Gaussian offsets of small amplitude were added to the main pseudo-Voigt profile in order to better describe the long wavelength (low energy) side of the $K\alpha_1$ and $K\alpha_2$ peaks. Since the high resolution Cu $K\alpha$ study of Maskil and Deutsch [49] reveals no low-energy non-diagram lines with relative intensities greater than 10^{-4}, these low-energy offsets must be regarded simply as unexplained empirical features of the profile.

As mentioned in **Appendix**, asymmetry of peaks is expected due to focusing defects resulting from operating the monochromator at low Bragg angles. The effect of the geometrical factors on the monochromator is illustrated in Figure 3 for the case of the Au $L\alpha$ emission peak. Two LiF (200) monochromators were used. The active length along the focal circle of one of the monochromators was reduced by covering the edges of the crystal with narrow bands of lead. The width of the lead strips (~ 2 mm) was chosen in order to obtain a

Table 1. Energy shift resulting from multiple hole configuration for S Kα (2307 eV). Calculations performed by Dr. B. Crasemann.

Additional hole	Calculated energy domain	Average energy separation (eV)[1]
2s	2302-2341	14.5
2p1/2	2311-2333	15.0
2p3/2	2307-2334	13.5
3s	2296-2321	1.5
3p1/2- p3/2	2301-2315	1.0

[1]From S Kα diagram peak.

----

compromise between the gain in wavelength resolution and the losing detection efficiency. The experimental Au Lα$_{1,2}$ peaks, analyzed by means of the two LiF monochromators (Bragg angle = 18.5°), are shown in Figure 3. Reducing the active area of the crystal resulted in a less pronounced peak asymmetry than that observed when using the total area of the monochromator. This observation is consistent with the broadening of peaks resulting from the focusing defect in the median plane of the monochromator occurring at low Bragg angles, i.e., at short distance of the point source from the monochromator (see equation 20 in **Appendix**). This effect explains the asymmetrical shape on the high energy side of the first order Cu Kα line (Fig. 2a). The asymmetry vanishes when measuring the second order reflection of the Cu Kα line (Fig. 2b), i.e., when increasing the distance of the point source from the monochromator. **In the remaining results presented below, only the LiF monochromator with the reduced area was used.**

K Lines

When 1s and 2p vacancies are created simultaneously, the 2p vacancy has a relatively long life-time compared to that of the 1s vacancy. Thus, the inner vacancy de-excites in presence of a spectator hole which produces a change in the electrostatic potential leading to shifts in the energy levels. The energy shifts for the Kα lines are given by:

$$\Delta K\alpha = (\Delta E)_{1s} - (\Delta E)_{2p} \qquad (3)$$

The energy shifts were kindly calculated for us by Dr. B. Crasemann (Department of Physics, University of Oregon, Eugene, OR 97403, USA). For the case of S Kα, they are given in Table 1. Because of the large number of atomic transitions involved in each case, the
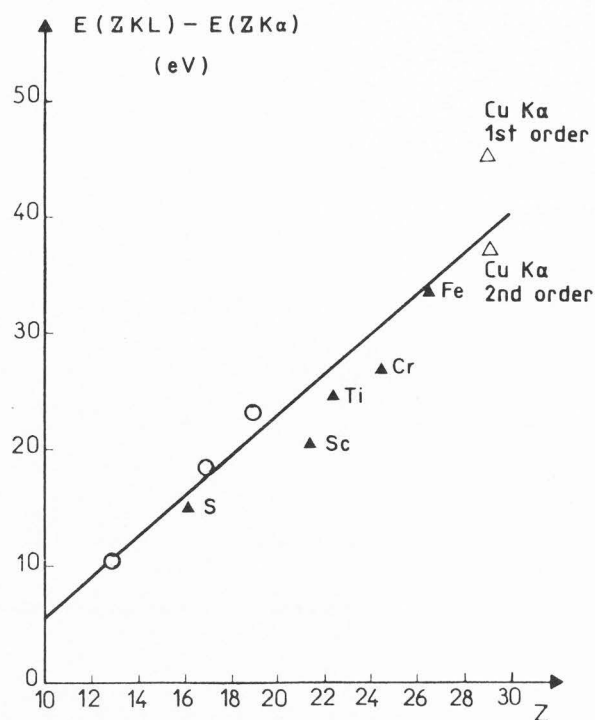
Figure 4. Energy separation distances in eV between the Z KL and Z Kα parent line as a function of the atomic number Z. Notice that for Z > 26, the satellite lines are hidden by the spectral distortion resulting from the monochromator mounting. Circles: Watson *et al.* cited in [8]; solid line: Bhattacharya *et al.* [8]; and triangles: this study.

----

satellite lines resulting from the presence of outer vacancies consist of a number of features closely spaced and only the envelope of these was observed. The 15 eV separation between the satellite labelled S KL (Fig. 1a) and the S Kα peak corresponds to the energy shift predicted for a 2s or 2p spectator vacancy. It is tempting to assign the second S KX "satellite" (Fig. 1a) as due to a 3s or 3p vacancy (S KM), but the energy separation is larger than calculated values and both the separation and the intensity excess larger than the values measured in the very high resolution work of Parratt [54]; this feature undoubtedly contains the S KM satellite, but it probably also reflects a slight imperfection in the line shape function.

As shown in Figure 4, the KL satellite position we measured relative to that of the parent Kα line for S, Sc, Ti, Cr and Fe exhibits a linear relationship as a function of the atomic number. The measured energy separation distances for the analyzed elements are consistent with the values derived from the experimental data of Watson
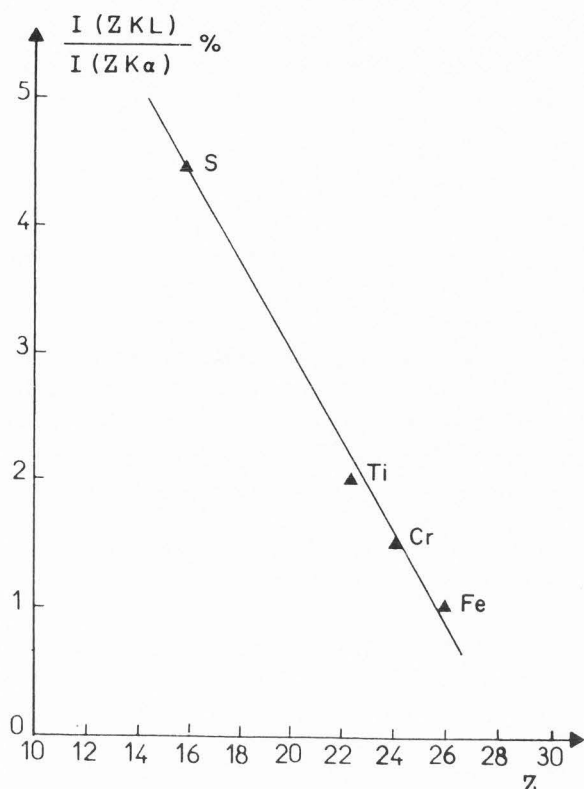
Figure 5. Measurements of Z KL to parent line Z Kα intensity ratios as a function of the atomic number (Z) of the analyzed elements.

---

et al. cited in [8] for Al, K and Cl and the calculated values of Bhattacharya *et al.* [8] for atomic numbers ranging from 10 to 30.

As shown in Figure 5, our data show a linear decrease of the KL satellite to Kα parent line intensity ratios as a function of the atomic number ranging from Z = 16 to Z = 26. The intensity ratios are in agreement with the measured data of Parratt [54] and with the theoretical predictions of Aberg [1].

Data in Figures 4 and 5 also show that the energy separation distance and the satellite intensity for Cu Kα derived from the second order reflection are consistent with the linear variations obtained for the other Kα lines. Data derived from the first reflection of Cu Kα peak do not satisfy these linear variations, indicating that the asymmetry of the Cu Kα emission peak is not purely a satellite band and that an instrumental factor probably contributes to the observed peak shape of the fundamental Cu Kα line as previously mentioned by comparing the first and second order reflections of the Cu Kα line analyzed with the LiF (200) monochromator (see Fig. 2).
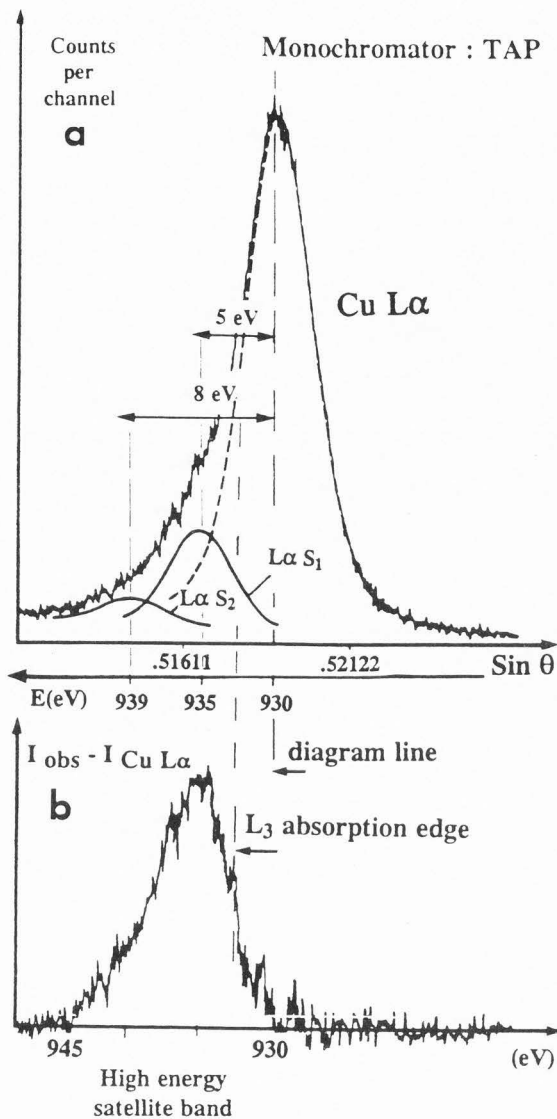
Figure 6. (a) Result of fit to the Cu Lα$_{1,2}$ emission peak for a pure Cu target analyzed with a TAP monochromator (incident energy: 15 keV). (b) Difference of observed and calculated intensities for Cu Lα.

Lα,ß Emission lines of pure elements

To obtain a good fit of the analytical profiles to the experimental data for Lα$_{1,2}$ emission peaks, Gaussian offsets were required on the short wavelength side of the peaks. Depending upon the atomic number of the analyzed elements, the weak high energy satellite bands were either partly resolved from the Lα diagram peak (see Fig. 1b for the case of Nb) or were unresolved leading to the development of a broad tail on the short
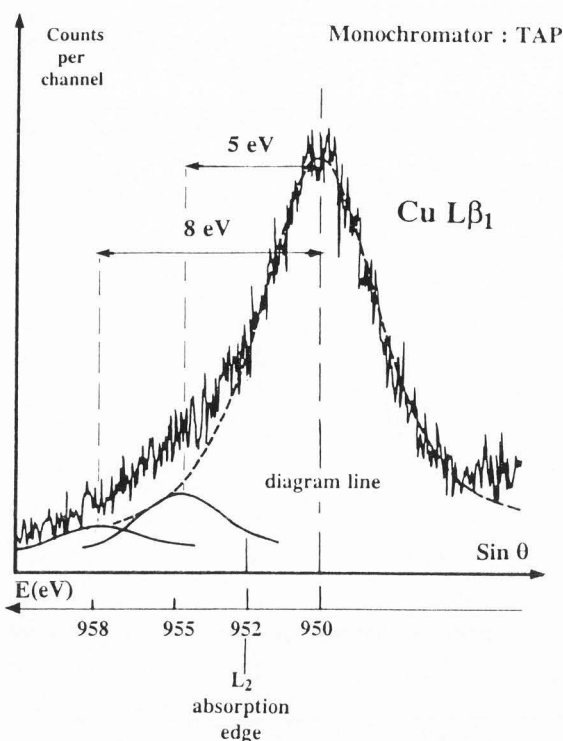
Figure 7. Result of fit to the Cu $L\beta_1$ emission peak for a pure Cu target analyzed with a TAP monochromator (incident energy: 15 keV).
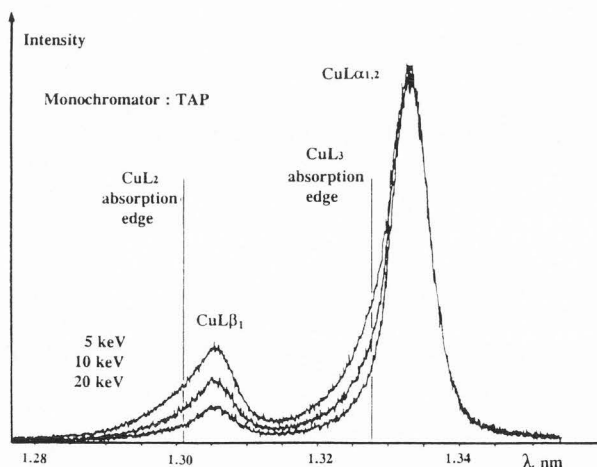
Figure 8. Cu $L\alpha,\beta$ line shape changes as a function of the incident energy (pure Cu specimen).

----

wavelength side of the peak as for the case of Cu $L\alpha$ (Fig. 6). In addition, for some of the analyzed elements, the $L\alpha$ emission shape was found to vary with the incident energy.

First-transition series metals. As shown in Figure 6, for a 15 keV incident energy, the Cu $L\alpha$ emission bands (L_3-$M_{4,5}$ transition) for a pure copper target using a TAP monochromator were found to be asymmetrical. Two Gaussian offsets were used in the fitting procedure to describe the tail occurring on the high energy side of the Cu $L\alpha_{1,2}$ peak. According to data of Doyle *et al.* [22], the Cu $L\alpha_1$ and Cu $L\alpha_2$ peak positions are given at the same value. The observed Cu $L\alpha_{1,2}$ peak was solved as a single peak in the fitting procedure. As shown in Figure 6, the two Gaussian offsets of the same width and different intensities were distant by 5 eV and 8 eV from the parent peak (930 eV), respectively. These values are consistent with those reported by Bonnelle [10, 11] and the calculated data by Kawai and Maeda [37] who showed that the high energy shoulder of the $L\alpha$ spectrum of divalent copper consists of several lines within the energy domain 932-935 eV.
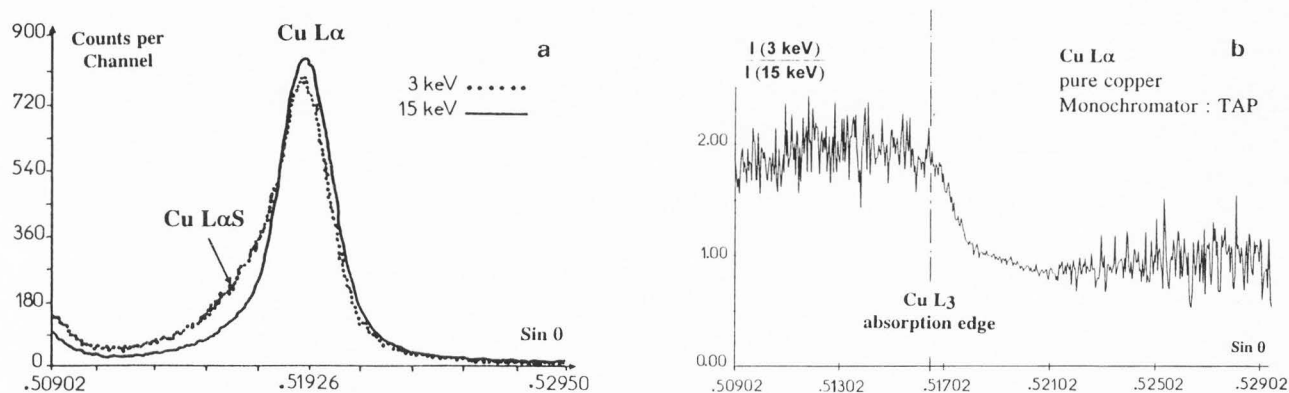
The $L\beta_1$ diagram line corresponds to the L_2-M_4 radiative transition. When a hole is present in the L_1 subshells, the L_1 vacancies can move to the L_2 subshell by L_1-L_2M Coster-Kronig transitions, leading to a de-excitation process of the L_2 hole in the presence of an outer M vacancy. Figure 7 shows a high energy satellite of the $L\beta$ diagram line for a pure copper specimen and a 15 keV incident energy. The high energy tail was solved as the sum of two Gaussian offsets distant from the diagram $L\beta_1$ line by 5 eV and 8 eV, respectively.

As reported by Fabian [23], the fine structure observed on the high-energy side of the peak in the $L\alpha,\beta$ emission of transition elements is attributed mostly to satellite emission lines arising from multiple vacancy (or multiple ionization) states produced by Auger transitions involving the initial L_1 and L_2 excited states. The threshold excitation technique (see **Appendix**) provides information on the mechanisms involved in the production of satellite lines. In the present study, the threshold excitation mode could not be used for the analysis for the Cu $L\alpha,\beta$ emissions since the L_1, L_2 and L_3 thresholds (1.099 keV, 0.9526 keV and 0.9328 keV, respectively) are too close to each other to permit accurate adjustment of the incident energies to these values by means of the EPMA.

However, as shown in Figure 8, the line shape of the Cu $L\alpha,\beta$ peak measured at the surface of a pure Cu target was found to be different when the electron energy was increased from 5 keV up to 20 keV. The high energy satellite was more clearly visible for a 5 keV incident energy than for a 20 keV incident beam. In addition, the $L\alpha/L\beta$ intensity ratio changed as a function of the incident energy, resulting from self-absorption as shown in Table 2. The absorption path-length increases when the incident energy is increased leading to a higher attenuation of the $L\beta$ intensity peak with respect to that

Table 2. Effect of self-absorption on the CuLα and CuLβ emission peaks as a function of the incident energy.

Ep (keV)	Satellite to parent line intensity ratios (%)		Lα/Lβ intensity ratios (%)	
	(Cu Lβ S / Cu Lβ)	(Cu Lα / Cu Lβ)	(Cu Lβ + Cu Lβ S) / (Cu Lα + Cu Lα S)	(Cu Lβ / Cu Lα)
5	26.6	27.7	28.2	28.4
10	19.6	12.9	18.0	17.1
20	13.5	2.5	9.6	8.7

Figure 9. (a) Cu Lα line shape changes as a function of the incident energy; and (b) effect of differential absorption of the Cu Lα satellite band and Cu Lα diagram lines obtained by taking the ratio of intensities I(3 keV)/ I(15 keV) measured at the surface of a pure Cu target excited at 3 keV and 15 keV, respectively.

of the Lα line. As shown in Figures 6 and 7, the L_3 and L_2 absorption edges lie between the non-diagram emission bands and the Lα and Lβ diagram lines, respectively, and differential absorption for these components is expected as a function of the incident energy as shown in Table 2. According to Hanzely and Liefield [31], the decrease in the satellite intensity, when the beam energy is increased, may be attributed to preferential self-absorption of the generated satellite photons by the matrix, since the absorption path-length is increased when the primary beam energy is increased.

The intensity of the Cu Lα spectrum induced by a 3 keV incident electron beam was normalized to that of the data acquired for a 15 keV primary beam energy, and the normalized intensity ratio I(3 keV) / I(15 keV) was studied as a function of wavelengths as shown in Figure 9. The jump in the I(3 keV) / I(15 keV)) corresponds to the Cu L_3 absorption edge occurring at 933 eV (1.328 nm).

The L_3 absorption edge for copper lies between the Cu Lα emission peak and the maximum intensity of the satellite band. Thus, a differential absorption by the target will affect the generated Cu Lα diagram and

satellite photons. Increasing the absorption path-length by increasing the incident energy will lead to a higher absorption effect for the satellite photons than for the Cu Lα photons, and the measured satellite to diagram line intensity ratio will decrease when the incident energy is increased as observed in Figure 9. Thus, the variations of the I(3keV) / I(15keV) versus wavelength represent the selective absorption of copper as a function of photon energies within a narrow domain containing the Cu L_3 absorption edge. Similarly, the L_2 absorption edge should be revealed by studying the satellite to L_1 line intensity ratios measured as a function of wavelength for two different values of the incident energy.

The Zn Lα emission band for pure Zn was also found to be asymmetrical [24, 63]. Results of the fit indicated that the tail can be decomposed into bands centered at 2.5 eV and 6 eV above the Zn Lα parent line position [63], respectively. These results are consistent with the two satellites experimentally observed by Leiro [46] while studying the fourth order reflection of the fluorescence Zn Lα emission. The area of the satellite band, measured for a 20 keV incident energy, represented ~ 24% of the total Zn Lα emission band intensity,

**Table 3.** Relative intensity of the satellite relative to that of Zn Lα as a function of the energy.

| | Incident energy (keV) | | |
	10	15	20
I (Zn Lα S) / I (Zn Lα + Zn Lα S) %	27	26	23.7

in agreement with calculated enhancement of Lα intensities due to non-radiative processes during electron bombardment [45]. Decreasing the incident energy did not significantly change the Zn Lα line shape resulting from self absorption for the Zn Lα and Zn Lß emission by the matrix. As shown in Table 3, the intensity ratio between the satellite and the Zn Lα parent line exhibited a slight change as a function of the incident energy. The small dependence of this intensity ratio upon the incident energy results from the absence of differential absorption for the diagram and non-diagram lines along the absorption path-length, the L_3 absorption edge for Zn lying above the energy of the shoulder to the Lα emission band. However, the intensity of the satellite band was found to vary with the specimen composition as discussed by Remond *et al.* [63].

Elements with Z > 36: Most of the quantitative work on a routine basis with the EPMA is carried out with incident beam energies ranging from 15 keV to 30 keV. These excitation conditions are suitable for the analysis of L lines whose energies lie between a few keV and 12 keV in order to keep the incident energy approximately 3 to 4 times greater than the L_3 ionization threshold for maximizing the ionization cross-section. Taking into account the mechanical limitations for the monochromator displacements, Lα lines for elements Z = 39 (Y) to Z = 52 (Te) are usually measured using a PET monochromator.

To obtain a good fit of the analytical profiles to the experimental data for $L\alpha_{1,2}$ emission peaks of elements in the atomic number range 39 to 52, two Gaussian offsets $L\alpha S_1$ and $L\alpha S_2$ were required on the short wavelength side of the peak, as illustrated in Figure 1b for the case of Nb. The observed satellite structure corresponds well to the higher-resolution observations of Juslen *et al.* [36], who observed five satellite lines which fell into two broad groupings that may be identified with the two features noted here. In the Nb case, our Gaussian offsets were displaced from $L\alpha_1$ by 7.5 and 16.5 eV, while the equivalent shifts deduced the better-resolved spectra of Juslen *et al.* [36] and Putila *et al.* [58] are about 8.5 and 15 eV. The spectra of Juslen *et al.* [36] correspond to those taken in the classic work of Randall and Parratt [59].
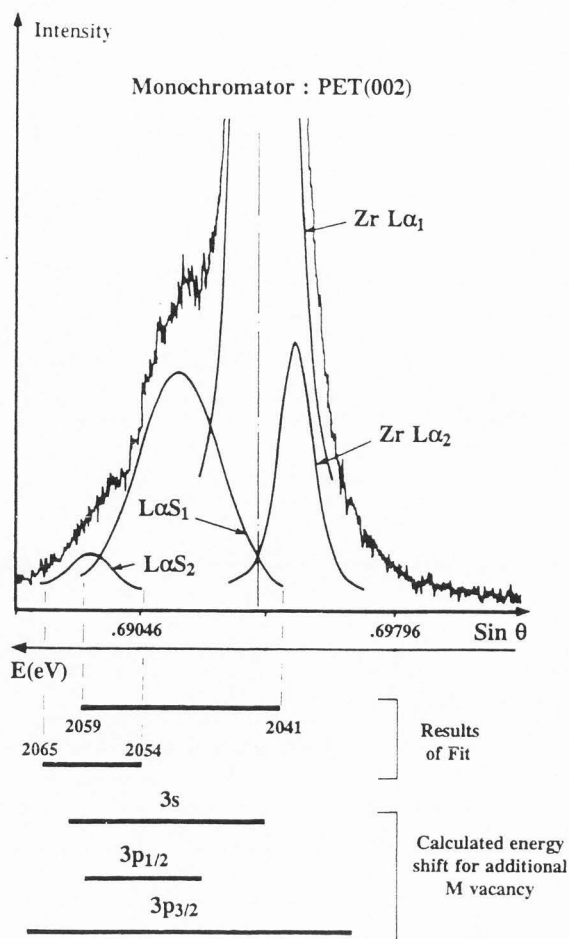
Figure 10. Result of fit to the Zr $L\alpha_{1,2}$ emission peak and calculated satellite energy domains resulting from additional vacancies in the M subshells (calculations carried out by Dr. B. Crasemann).

Results in Table 4 show that the same two groups of satellite bands $L\alpha S_1$ and $L\alpha S_2$, distant by about 7-8 eV and 12-17 eV, respectively, from the main Lα diagram line, also exist for the pure elements Y (Z = 39), Mo (Z = 42) and Rh (Z = 45) analyzed in the present study.

The energy separation distance of 7-8 eV for the main compound satellite feature suggests that it arises from de-excitation of the L_3 vacancy in the presence of an additional spectator vacancy in the M shell. In addition, as illustrated in Figure 10 for the Zr Lα emission band, the energy widths of the measured $L\alpha S_1$ and $L\alpha S_2$ satellite bands are consistent with the calculated energy widths resulting from the de-excitation of a L_3 vacancy

Table 4. Energy separations and intensities of the Lα S1 and Lα S2 Gaussian offsets to Lα diagram lines derived from 20 keV electron induced X-ray spectra of some pure elements.

| Emission line | Separation distance (in eV) | | {I(LαS$_1$ + LαS$_2$) / I(Lα$_{1,2}$)} % | |
	(LαS$_1$ - Lα)	(LαS$_2$ - Lα)	(a)	(b)
Y Lα (1922 eV)	7.4	14.2	14.8	15.5
Mo Lα (2292 eV)	7.8	18.0	18.1	16.9
Rh Lα (2698 eV)	7.0	11.6	21.1	19.1

(a) Intensity of the Lα S1 and Lα S2 satellites calculated using the FWHM of the Gaussian offsets as independent variables in the fitting procedure; and (b) FWHM of the Gaussian offsets set as coupled variables in the fitting procedure.

Table 5. Energy ranges in eV for satellite lines resulting from an additional vacancy in M subshells calculated by Dr B. Crasemann.

Emission line	3s hole	2p 1/2 hole	3p3/2 hole
Zr Lα	(2043-2062)	(2048-2060)	(2034-2069)
Nb Lα	(2162-2183)	(2168-2187)	(2153-2198)
Mo Lα	(2292-2309)	(2296-2312)	(2281-2328)
Rh Lα	(2700-2715)	(2700-2715)	(2689-2727)

Table 6. Observed energy domain in eV containing the Lα S$_1$ and Lα S$_2$ bands.

Emission line	(Lα S$_1$) eV	(Lα S$_2$) eV
Y Lα	(1921-1936)	(1933-1940)
Zr Lα	(2041-2059)	(2054-2063)
Nb Lα	(2163-2184)	(2177-2187)
Mo Lα	(2291-2314)	(2306-2319)
Rh Lα	(2696-2715)	(2694-2727)

Table 7. Observed intensities of the Lα S$_1$ and Lα S$_2$ satellite features relative to the Zr Lα$_{1,2}$ emission band as a function of the incident electron beam energy.

Primary energy (keV)	{I(Zr LαS$_1$) / I(Zr Lα$_{1,2}$)} %	{I(Zr LαS$_2$) / I(Zr Lα$_{1,2}$)} %
10	12.8	2.6
15	12.7	3.5
20	13.4	2.6
25	12.5	2.8
Average	12.9 ± 0.3	2.9 ± 0.3

in presence of an additional 3s, 3p1/2 or 3p3/2 hole (calculations performed by B. Crasemann). Table 5 presents theoretical energy ranges for X-rays emitted in the presence of spectator vacancies in the M$_1$, M$_{2,3}$ and M$_{4,5}$ subshells; there is good agreement between these figures and the observed satellite band widths for 39 < Z < 45 shown in Table 6. In comparing these numbers, it must be remembered that in the ground state these atoms have two open subshells; thus, transitions occur between many different initial and final states, and the observed satellite structure is broad and complex. Krause et al. [42] suggested that the weaker satellite feature displaced by about 15 eV may be due in part to the de-excitation of LMM triple-vacancy states. They also calculated the energy shifts that would result from an N spectator vacancy; the result of 0.5-1 eV indicates

that the de-excitation of L$_3$MN states will result in a satellite that is not distinguishable from the diagram line.

The L$_1$-L$_3$M$_{4,5}$ Coster-Kronig transition is not energetically allowed for all elements, and Hartree-Fock calculations indicate that a cut-off occurs at Z = 51. Since the other processes cited as responsible for the satellites are second-order processes, then for Z < 51, the Coster-Kronig transitions will be the predominant source of satellites. We compared our measured satellite intensity ratios to experimental and theoretical data from the literature. They are in fair agreement with the results of Juslen et al. [36] and Putila et al. [58] using 40 keV electrons, and those of Doyle and Shafroth [21] using 2.5 MeV protons. Despite the differences in excitation mode and energy, there is in common a significant drop in the satellite intensity ratio at Z = 50.

The uncertainty of our measured ratios is estimated as about 3-5% by comparing the data obtained from the fitting procedure when the widths of the Gaussian offsets were kept as coupled variables or allowed to be independent. Results in Table 4 show that the intensity ratios of the LαS$_1$ and LαS$_2$ satellites to the total intensity of the Lα emission band remained constant for elements 39 < Z < 42. These ratios also remained constant when the incident beam energy was increased from 10 keV to 25 keV, i.e., for incident energies much higher than the excitation threshold of the L$_3$ subshell of the analyzed elements.
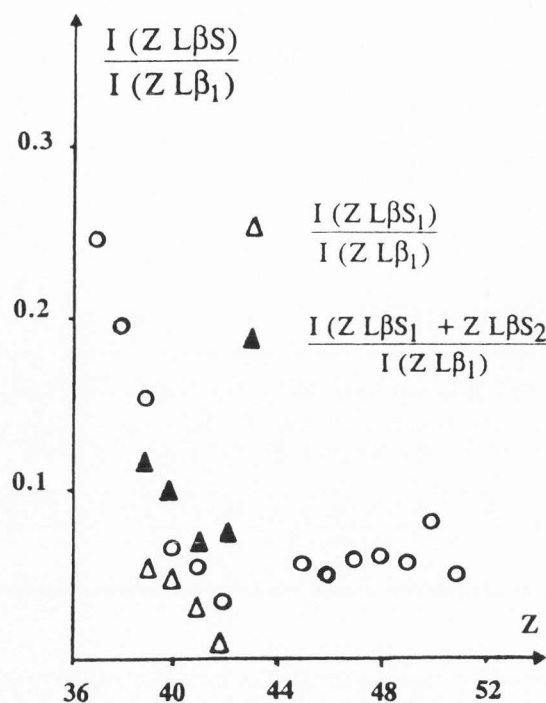
Figure 11. I(LαS/ILα) satellite to diagram line intensity ratios as a function of the atomic number (Z). Circles: data according to Doyle and Shafroth [21] derived from 2.5 MeV proton induced X-ray spectra; triangles: data derived from 20 keV electron induced X-ray spectra in the present study.

Table 8. Observed high energy $L\beta$ satellite to $L\beta_1$ diagram line separations in eV for 20 keV electron induced X-ray spectra of Y, Nb and Zr.

Atomic numbe	Measured energy separations (eV)	
	$(L\beta S_1 - L\beta_1)$	$(L\beta S_2 - L\beta_1)$
39 (Y)	4.2	9.9
40 (Zr)	4.3	10.2
41 (Nb)	4.6	10.2

Results in Table 7 illustrate the satellite to diagram peak intensity ratio as a function of the incident energy for the case of Zr Lα (2.042 keV). The total intensity for the satellite features $L\alpha S_1 + L\alpha S_2$ relative to the Zr $L\alpha_{1,2}$ band is found to be independent of the incident energy, allowing for the uncertainty in the fitting procedure. The Zr L_3 absorption edge occurs at 2.220 keV. The energy separation (Zr L_3 - Zr Lα) is much greater
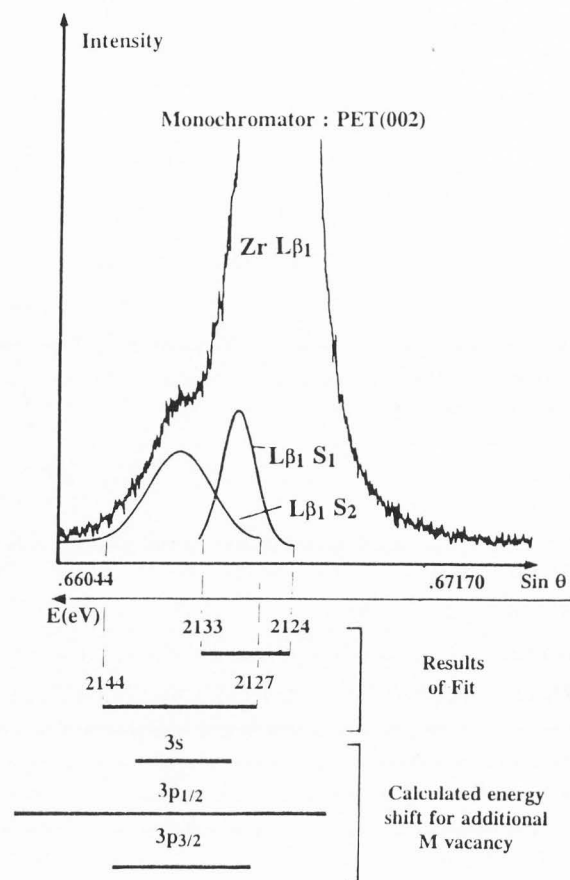
Figure 12. Result of fit to the Zr $L\beta_1$ emission peak and calculated satellite energy domains resulting from additional vacancies in the M subshells (calculations carried out by Dr. B. Crasemann).

----

than the separation between the non-diagram and the diagram Zr Lα lines, and the differential absorption increases simultaneously for both the diagram and non-diagram bands when the incident beam energy is increased.

Let $n_3(L_3)$ be the number of diagram X-rays originating from a single hole in the L_3 subshell, $n'_3(L_3M)$ the number of satellites originating from a double hole configuration in the L_3 and M shells, $n'_3(LN)$ the number of satellites originating from double holes in the L_3 and N shells and $n''_3(L_3MM + L_3MN)$ the number of satellites originating from the triple hole L_3MM and L_3MN configurations. The intensity of each corresponding X-ray line is proportional to the number of singly, doubly or triply ionized states. Thus, according to Krause *et al.* [42], if all the satellite structures were

separated from the parent line their total intensity I(sat) relative to that of the true diagram emission line $I(L\alpha_{1,2})$ should be:

$$\{I(sat) / I(L\alpha_{1,2})\} =$$
$$\{n'_3(L_3M) + n'_3(LN) + n''_3(L_3MM + L_3MN)\}/n_3(L_3). \tag{4}$$

In fact, only the satellites resulting from a double hole configuration in the L_3 and M shells have a sufficient energy separation to be distinguished from the parent diagram line. The number of satellites $n'_3(L_3N)$ and $n''_3(L_3NN)$ resulting from double and triple hole states in the L_3 and N shells cannot be distinguished experimentally from the diagram $n_3(L_3)$ X-rays, so that the observable satellite $\{I'(L\alpha_{1,2})\}$ to $L\alpha$ parent line intensity ratio should be:

$$\{I(sat) / I'(L\alpha_{1,2})\} =$$
$$\{n'_3(L_3M) + n''_3(L_3MM + L_3MN)\} /$$
$$\{n_3(L_3) + n'_3(L_3N) + n''_3(L_3NN)\} \tag{5}$$

These two ratios were calculated by Krause et al. [42] for the Zr L spectrum induced by 9 keV electrons, using a variety of initial L subshell vacancy distributions and Coster-Kronig probability values. The best agreement between measured and calculated observable satellite to diagram ratio was obtained with an initial vacancy population $L_1:L_2:L_3 = 0.9:1:2$; the measured ratio was 18% and our present value of 15.8% (Table 8) is in fairly good agreement. Xu [80] has criticized the procedure by which Krause et al. [42] held $L_2:L_3$ constant during their solution and his analysis suggests $L_1:L_2:L_3 = 0.7:1.0:2.2$. There is as yet insufficient information in the literature on electron ionization cross-sections at energies near threshold for us to make a definitive selection, from which a more accurate satellite intensity ratio might be derived. In addition, the L_1 Coster-Kronig yields are not yet precisely known. For these reasons, we must be satisfied with the measured values (Table 8) of satellite to diagram intensity ratios and with the observation that, given the present data, theory predicts values that are not dramatically different from these as illustrated in Figure 11.

As shown in Figure 12, for the case of Zr $L\beta_1$, the measured energy shifts for the $L\beta S_1$ and $L\beta S_2$ offsets with respect to the Zr $L\beta_1$ diagram line are consistent with the calculated shifts on the basis of an additional M vacancy. However, assuming that the outer hole resulted from Coster-Kronig transitions, a single satellite band would be expected since only the L_1-$L_2M_{4,5}$ Coster-Kronig transition may affect the initial L_2 vacancy. As for the case of the satellite of higher energy associated
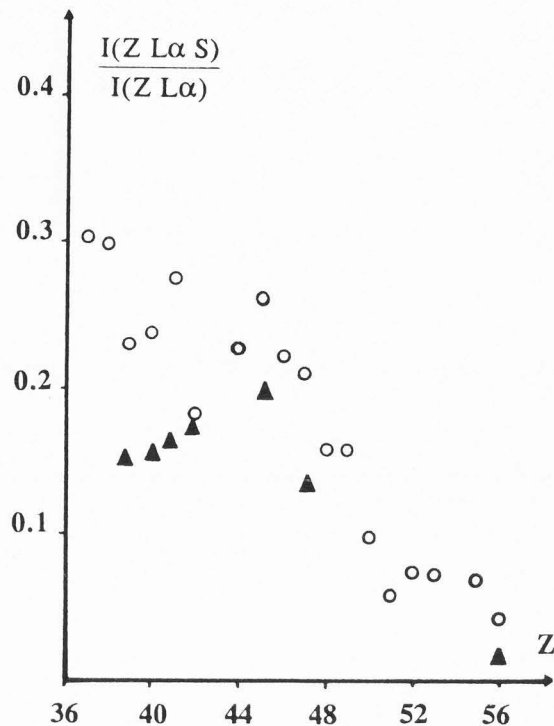

Figure 13. I($L\beta$ S) satellite to I($L\beta$) diagram line intensity ratio as a function of the atomic number (Z). Circles: data according to Doyle and Shafroth [21] derived from 2.5 MeV proton induced X-ray spectra; and triangles: data derived from 20 keV electron induced X-ray spectra in the present study.

----

with the Zr $L\alpha$ parent line, the higher energy satellite to the $L\beta$ diagram line may be associated with transitions in triple hole states such as LMM or LMN configuration resulting probably from a cascade mechanism such as L_1-L_2M (or N) $\to$ L_2M (or N) $\to$ L_3M (or N). As shown in Figure 13, the observed satellite intensities were also found to be consistent with the data reported by Doyle and Shafroth [21] and the value of 8.7% published by Krause et al. [42] for the case of the Zr $L\beta$ emission spectrum produced by a 9 keV incident electron beam.

In the present work, using the PET monochromator, the two satellite features to the short wavelength side of $L\alpha,\beta$ peaks ceased to be resolvable at Z = 47; Gaussian offsets used for correcting the asymmetry of peaks could no longer be proposed. These measurements suggested that, for $L\alpha$ lines of elements Z > 47 occurring at Bragg angles lower than 30°, the satellite emission bands were hidden by spectral distortion resulting from instrumental factors as will be discussed later.
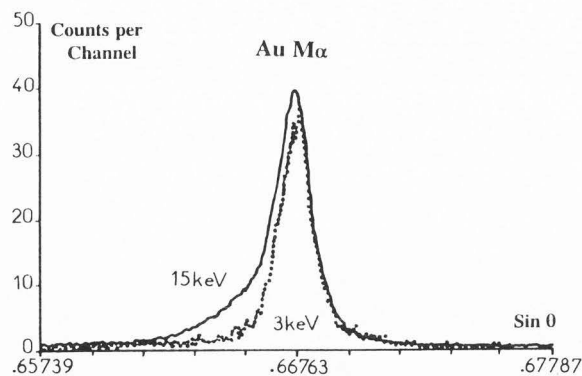
Figure 14. Line shape changes of the Au Mα emission peak as a function of the incident electron energy. The 3 keV incident energy is lower than the M_1 and M_2 ionization thresholds (see text).

Elements with Z > 56: In practice, Lα emission lines for elements Z > 56 (Ba) are detected with LiF (200 planes) monochromators. For the rare-earth elements 57 < Z < 71, the L emission spectra are complex. In addition to high energy satellites resulting from mechanisms giving rise to multiple outer vacancies, non-diagram lines may also occur on the low energy side of X-ray peaks involving transitions originating from the incompletely filled 4f levels. Using the same fitting function (equation 1) as that used in the present work, Remond *et al.* [62] showed that the envelope of the low-energy satellite bands is detected by the use of the LiF monochromator. The energy separation distances between the satellite bands and the parent line were found to be consistent with the calculated data available in the literature [69, 78].

A high energy tail also became apparent for Lα emission bands occurring at Bragg angles lower than 30°. The asymmetry became very pronounced for Lα emission peaks of elements of high atomic number such as Z > 74 (W). In addition, for these elements, the first and second order reflections led to very different observed peak shapes. The contribution of high energy satellite lines to high energy Lα lines occurring at low Bragg angles will be discussed later taking instrumental factors into account.

M Satellite lines

Results in Figure 1c showed that the Au Mα peak analyzed with a PET monochromator was asymmetrical because of a broad tail on its short wavelength side. The tail occurring on the short wavelength side of the Au Mα peak was described as the sum of two Gaussian offsets of same width. The separation distance between

Au $M\alpha_1$ and Au $M\alpha_2$ is equal to 5 eV. According to Chen and Crasemann [18], the intensity of the $M\alpha_2$ line relative to the $M\alpha_1$ line is only 1.9 %, and so the contribution of the $M\alpha_2$ peak was omitted in the analytical description of the observed Au Mα photon distribution. The best fit was obtained for a value $C_g = 0.4$ in the fitting function. The difference spectrum between the experimental data and the pseudo-Voigt profile consisted of an asymmetrical peak which was described by the sum of two Gaussian offsets of equal width (see Fig. 1c). The separation distance between the maximum of the satellite band and the Au Mα peak was 6 eV (0.00162 nm). The intensity of the tail represented 17 % of the total intensity of the AuMα emission peak. Similar data were obtained from the Hg Mα and Pt Mα spectra.

As shown in Figure 14, a less pronounced asymmetry of the Au Mα emission peak of a pure Au target was obtained for a 3 keV incident energy, than that observed when a 15 keV incident beam was used. The excitation energy thresholds for the M_5 to M_5 subshells are 3.425 keV (M_1), 3.150 keV (M_2), 2.743 keV (M_3), 2.291 keV (M_4) and 2.206 keV (M_5), respectively. Thus, a 3 keV incident energy is sufficient to provoke the Au Mα emission involving the initial hole in the M_5 subshell. Additional vacancies in the M_3 and M_4 subshells may also be induced leading to possible outer N vacancies resulting from Coster-Kronig transfer of the type M_3-M_5N_x. The slight asymmetry of the Au Mα peak measured at the 3 keV threshold may result from the de-excitation of the M_5 shell in presence of outer vacancies induced by simultaneous ionization process or induced by Coster-Kronig transfer of M_3 and M_1 vacancies to the M_5 subshell.

The M_1 and M_2 subshells are excited by the 15 keV incident energy and the resulting inner vacancies can move to the M_5 subshell according to Coster-Kronig mechanisms with the production of outer holes. The pronounced observed asymmetry of the Au Mα peak may reasonably be assigned to the development of high energy satellites resulting from the de-excitation of the M_5 level in the presence of additional outer N vacancies consistent with the calculation performed by Keski-Rahkonen and Krause [39] for the case of the U Mα emission (see Table 9).

For incident energies above the M_1 subshell excitation threshold, high energy Au MαS satellites will develop. The satellite to Au Mα intensity ratios were studied as a function of the absorption path-length for the generated photons within the pure gold target. For this purpose, the incident electron energy was increased from 5 keV to 8 keV, 10 keV, 12 keV, and 15 keV, successively. As shown in Table 10, the energy separation distance between the satellite maximum position and the Au

Table 9. Calculated energy shifts en eV of double hole satellites relative to the UMα parent line according to Keski-Rahkonen and Krause (39).

Level of the second hole	N_1	N_2	N_3	N_4	N_5	N_6	N_7
Satellite to UMα separation (eV)	9.4	10	7.5	8.4	7.7	7.4	6.9

Table 10: Observed high energy satellite energy differences and intensities with respect to the Au Mα emission peak as a function of the incident electron energy.

	Incident energy (keV)				
	5	8	10	12	15
Au MαS - Au Mα (eV)	5.40	5.46	5.43	5.49	5.21
{I(Au MαS) / I(Au Mα)} %	15.5	15.7	16.4	16.5	17.0

Mα parent line remained independent of the incident energy. The small increase of the intensity ratios as a function of the incident energy is more probably due to an increase of the statistical precision of the measured intensities rather than to interactions between the generated photons with the matrix.

The line shape of the residuals between the observed photon distribution and the Au Mα diagram emission peak is very consistent with the data reported by Laakkonen and Graeffe [43]. Using a Cr X-ray fluorescence tube and a high precision double-crystal spectrometer, these authors showed that the Mα and Mβ peaks for Au, Th and U are accompanied by asymmetrical fine structures extending up to 15 eV above the parent lines. These authors also showed that the satellite intensity relative to the total emission intensity was 0.50, 0.38 and 0.33 for Au, Th and U, respectively.

Although the satellite intensities have a large uncertainty owing to the large number of variables in the fitting procedure, the Au MαS satellite to parent line intensity ratio we measured was lower than the value reported by Laakkonen and Graeffe [43] for the case of the Au Mα emission induced by X-ray photons. Similarly, the 33% relative satellite intensity for the U Mα emission induced by X-ray fluorescence reported by Laakkonen and Graeffe [43] is higher than the value reported by Keski-Rahkonen and Krause [39] who studied the U Mα and U Mβ X-ray spectra from a thick metallic target excited by 12 keV electrons using the PAX (photoelectron spectrometry for the analysis of X-rays) technique. The high energy satellite structures lying 6-12 eV above the peaks were reported to be ~ 11% relative to the intensity of the parent lines, i.e., a third of the value obtained for the case of X-ray photon excitation.

According to the calculations performed by Keski-Rahkonen and Krause [39], a 50 eV separation distance between the Mα peak and its satellite would result from the M_5 hole de-excitation in the presence of a second hole in the M shells. A simultaneous vacancy in the M_5 shell and one of the seven N subshells would lead to energy shifts as shown in Table 9.

Besides radiative transitions in the presence of preferentially created M_5N hole states, additional holes may also be created in the O, P and Q shells by a shake-off mechanisms in which the N vacancy resulting from $M_{4,5}N_x$ Coster-Kronig transfer is moved to the outer shells before the radiative decay of the $M_{4,5}$ hole. Additional holes in O, P or Q shells will lead to satellite lines occurring only a few tenths of one eV above the Mα diagram line. Although these structures cannot be distinguished from the main Mα peak, about 20% of the Mα peak intensity is due to these shake-off satellite contributions [39].

The large number of possible multiple vacancies in the N shells, created predominantly by Coster-Kronig transitions in the M subshells, will lead to high energy satellite peaks but only the envelope of these satellites is observed.

Contribution of Instrumental Distortions to the Shape of Non-Diagram and Diagram-Lines

The shape of the S Kα, Nb Lα and Au Mα diagram peaks (Figs. 1a, 1b and 1c) of similar energy analyzed with the PET monochromator were found to be very different. For the S Kα peaks a set of values $C_g = 0.6$ (i.e., $C_1 = 0.4$) were used to correctly describe the K$\alpha_{1,2}$ peak shape indicating a more pronounced Gaussian shape of the Kα lines than for the case of the Lα and Mα peaks which were characterized by higher Lorentzian contributions, i.e., $C_1 = 0.6$ for Nb Lα and 0.7 for Au Mα.

The proportion of Gaussian and Lorentzian distributions in the peak profiles (equation 1) is a function of the
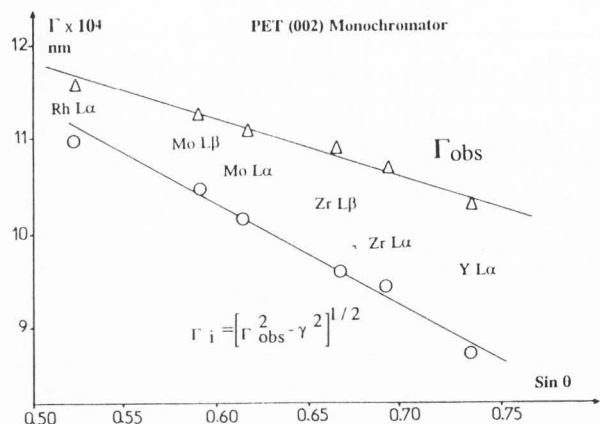
Figure 15. Calculated full-width at half-maximum and instrumental response function for X-ray diagram lines occurring at Bragg angles > 30° with a PET (002) monochromator.
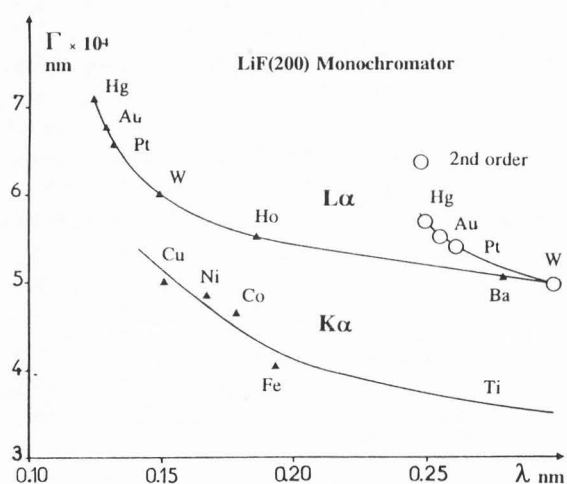
Figure 16. Calculated full-width at half-maximum of Kα and Lα diagram peaks (pseudo-Voigt profile, equation 1) analyzed using a LiF (200) monochromator.

----

intrinsic properties of the analyzed emissions, i.e., of the energy subshells involved in the analyzed radiative transitions. Accounting for the difference of natural width for K, L and M diagram lines of similar energies [68], the line shape of a L emission peak is expected to be more Lorentzian than that of the Kα line analyzed with the same monochromator, consistent with the values of the C_g parameter used in the fitting procedure. Studying the fine structure of L X-ray spectra of the lanthanide elements (incompletely filled 4f shell), Salem

and Scott [69] fitted their experimental data using the sum of two Lorentzian distributions. Salem *et al.* [70] described the Kß X-ray spectra of transition elements (incompletely filled 3d shell) by the sum of two Gaussian distributions.

Neglecting the contribution of the natural width of the observed peak width may lead to spurious decomposition of complex peaks using the fitting procedure. Studying L X-ray spectra of rare-earth elements, Remond *et al.* [62] showed that using the same width for all L X-ray peaks equal to that observed for the intense Lα peak resulted in description of the Lß₃ emission as a doublet. The natural width of the Lß₃ emission line is about twice that of the Lα emission peak. Taking account of this difference in the fitting procedure led to a correct description of the Lß₃ emission as a single peak.

In order to account for the natural width observed in L X-ray spectra of the lanthanide elements, Remond *et al.* [62] replaced the observed width, used as a variable in the fitting function (equation 1), by quadratic addition of the instrumental resolution Γ_i and natural width γ, according to:
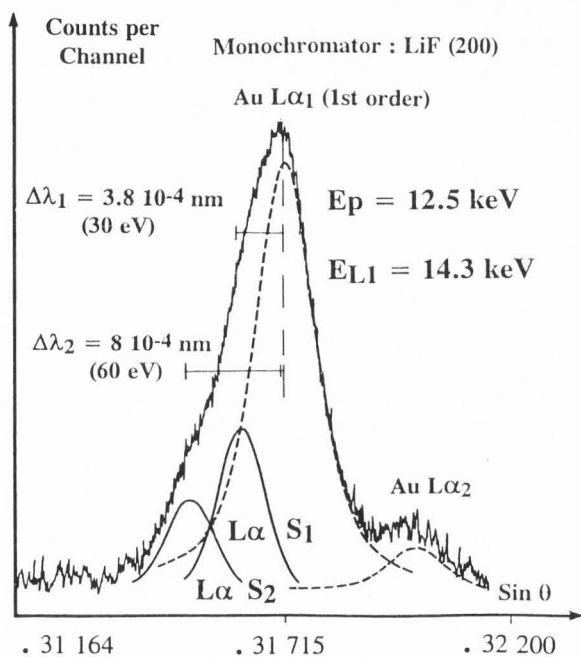
$$\Gamma = (\Gamma_i^2 + \gamma^2)^{1/2}. \tag{6}$$

The intrinsic widths for the Kα and Lα lines where derived from the data published by Salem and Lee [69]. From these data, a linear relationship was observed of the emitter, ranging from Z = 20 (Ca) to Z = 28 (Ni). An estimated intrinsic width of ~ 0.4-0.5 eV for the S Kα line was estimated from this linear relationship. The intrinsic width of the S Kα line is thus negligible with respect to the observed width of 3.7eV (8.7 x 10⁻⁴ nm) derived from the fitting procedure. Thus, the calculated 3.7 eV width mainly represents the instrumental resolution of the PET monochromator at the measured energy of the S Kα (2308 eV). We can reasonably assume that the instrumental resolution is slowly varying within the narrow analyzed Bragg angle domain containing the Nb Lα peak (2196 eV) and the Au Mα emission line (2123 eV). The predicted width of the experimental Nb Lα peak according to equation 19 should be 4.1 eV which differs by less than 3% of the observed peak width which is 3.97 eV.

Using the value of 3.7 eV for the energy resolution of the PET monochromator, an estimate was made for the natural width of the Au Mα peak (2123 eV). The measured peak width (Γ = 0.00126 nm, i.e., 4.58 eV) corrected for the contribution of the short wavelength satellite lines was used in equation 6. The calculated intrinsic width for the Au Mα line was found to be 2.7 eV which is very close to the 2.5 eV intrinsic width reported by Laakkonen and Graeffe [43]. After correction for asymmetry by adding Gaussian offsets to the fitting

Table 11. Spectral decomposition for the Au Lα first order of reflection analyzed with a LiF (200) monochromator (Johann mounting) as a function of the incident energy.

Ep keV	Width of the pseudo-Voigt profile (nm) x 10^4	Width of the Gaussian (nm) x10^4	Distance (in nm) of Gaussian offsets from the maximum of the pseudo-Voigt profile x 10^4		Area of the Gaussian offsets relative to the total Au Lα peak area
12.5	6.2	4.75	3.8	8.2	24.8 %
15	6.3	5.60	3.7	8.3	31.4 %
20	6.2	5.80	3.9	8.5	31.9 %

Figure 17. First order reflection of the Au Lα$_{1,2}$ emission band analyzed with the LiF (200) monochromator and a 12.5 keV incident energy (just above the Au L$_3$ excitation threshold).

----

function, the width of Lα, and Lβ$_1$ peaks occurring at Bragg angles greater than 30° exhibited a linear variation as a function of the analyzed wavelengths as shown in Figure 15. From all analyzed L X-rays peaks, the resolution Γ$_i$ of the spectrometer equipped with a PET monochromator was calculated using equation 6. As shown in Figure 15, a linear relationship was found to exist between the instrumental resolution Γ$_i$ and the analyzed L emission peak wavelengths occurring between Bragg angles ranging from 30° to 49°. For

Bragg angles lower than 30°, a departure from the linear variation was observed.

The dependence of the peak shape with the Bragg angle is illustrated in Figure 16 for the case of Kα and Lα emission peaks analyzed with a LiF (200 planes) monochromator.

After the observed asymmetry of peaks was corrected by adding Gaussian offsets to the pseudo-Voigt function (equation 1) used to describe each analyzed diagram emission, whose shape is assumed to be symmetrical, the width of the peaks decreased exponentially for peaks occurring at Bragg angles lower than 30°. This angle is significant since above this, both Kα and Lα width varied linearly as a function of wavelength. The exponential decrease of peak width for wavelengths < 0.17 nm probably resulted from the sum of several effects which were incompletely described by the adding of Gaussian offsets to the pseudo-Voigt profile (equation 1) of the diagram lines.

Differences in the line shape for first and second order reflections have been illustrated in Figure 2 for the case of the Cu Kα$_{1,2}$ peaks analyzed with the LiF (200) monochromator. Similar differences have been observed for the case of the Au Lα$_{1,2}$ emission peaks as shown in Figure 17. In order to evaluate the role of instrumental factors and the presence of satellite lines, the first and second reflection order of the Au Lα$_{1,2}$ emission were analyzed using the threshold excitation mode.

For the LiF (200) crystal, the first order reflection for the Au Lα emission occurs at Bragg angle θ = 18.5°. In order to avoid high energy satellites resulting from Coster-Kronig transitions, the electron energy was first adjusted to 12.5 keV, a value just above the L$_3$ excitation threshold (11.9 keV) and below the excitation thresholds of the L$_1$ and L$_2$ subshells (14.3 keV and 13.7 keV, respectively). As shown in Figure 17, in the absence of production of high energy Coster-Kronig satellites, the Au Lα peak was found to be asymmetrical. Two shoulders are visible on the tail occurring on the short wavelength side of the measured Au Lα peak using

105
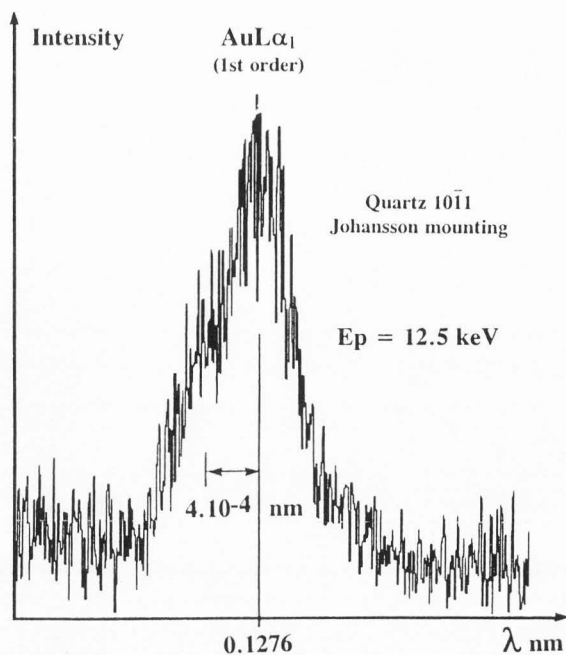
Figure 18. First order reflection of the Au $L\alpha_{1,2}$ emission band analyzed with a quartz $(10\bar{1}1)$ monochromator and a 12.5 keV incident energy (just above the Au L_3 excitation threshold).

----

the LiF (200) monochromator. In order to obtain a satisfactory fit, two Gaussian offsets of equal width were used to describe the tail observed on the short wavelength side of the Au $L\alpha_1$ peak. The best fit to the experimental data was obtained by setting $C_g = 0.35$ in the pseudo-Voigt function (equation 1) used to describe the diagram line. The incident electron energy was then increased to 15 keV and 20 keV, values higher than the L_1 excitation threshold for Au. The measured Au $L\alpha$ peaks were processed as mentioned above. Results of the fits are shown in Table 11.

From data in Table 11, it can be seen that the calculated width of the emission peak described by a pseudo-Voigt profile (equation 1) remained independent of the incident energy as expected for a diagram line. The measured wavelength separation distances between the Gaussian offsets and the Au $L\alpha$ diagram line were constant for all incident energies used. The width of the two Gaussian offsets was found to be 17% lower for the 12.5 keV incident energy with respect to that obtained when using incident energy higher than the L_1 and L_2 excitation thresholds. Simultaneously, the total area of the two Gaussian offsets relative to the total measured peak area was ∼ 20% lower for data obtained with a 12.5 keV incident energy than for higher incident

energies.

For incident energies just above the L_3 excitation threshold, the area of the high energy tail represents ∼ 25% of the total area of the Au $L\alpha$ emission band, Coster-Kronig transitions being not permitted for the incident energy used, so this high energy tail more probably results from instrumental distortion rather than satellite lines associated with multiple ionization processes. As shown in Figure 18, asymmetry of the Au $L\alpha$ emission peak was also observed when using a quartz $(10\bar{1}1)$ monochromator installed within the Johansson mounting type spectrometer. In this mounting, the Bragg conditions are satisfied for all beams impinging the crystal surface. However, the asymmetrical shape is not a result of a misalignment of the Johansson quartz monochromator because the same high energy tail to the Au $L\alpha_1$ peak was observed for all quartz crystals installed on several EMPA's. The focusing defect along the focal circle (see equation 20 in **Appendix**) resulting from departure from the Bragg conditions for X-rays incident far from the center of the crystal does not exist for the Johansson mounted quartz crystal while this effect is pronounced for the Johann LiF monochromator. However, common to both monochromator geometries is the **focusing defect arising from the thickness** of the crystal (see equation 19 in **Appendix**) leading to a change of the incident angle as a function of depth inside the crystal. Accounting for the low Bragg angle corresponding to Au $L\alpha$, the focusing defect due to the thickness of the monochromator is large for both crystals used.

Increasing the incident energy above the L_1 excitation threshold leads to an increase of the area of the high energy tail. This increase may result from the presence of satellite lines. However, it is not possible to separately solve the two contributions to the tail, i.e., instrumental distortions, and satellite, by empirically adding Gaussian offsets in the fitting procedure.

The predominance of instrumental distortion over satellite lines leading to the high energy tail to the Au $L\alpha$ emission peak is supported by comparing data in Figure 19 with the Au $L\alpha$ second order reflection analyzed with the same LiF monochromator. The Au $L\alpha$ (2nd order) peak, measured using a 12.5 keV incident energy, was correctly described by a single pseudo-Voigt profile. The best fit was obtained by setting $C_g = 0.6$ in the fitting function (equation 1). The peak width was found to be $5.18 \ 10^{-4}$ nm. These values were kept as constant in the fitting procedure applied to spectra obtained when using a 15 keV and 20 keV incident energy successively. The difference between the experimental data and the calculated pseudo-Voigt profile showed a residual on the short wavelength side of the peak as illustrated in Figure 19 for the case of the second order reflection for the Au $L\alpha$ emission peak observed for a

20 keV incident electron beam. This high energy feature probably corresponds to satellites resulting from mechanisms involving multiple outer vacancies.

For X-ray peaks occurring at Bragg angles lower than 30°, the spectral distortion resulting from the Johann mounting of the LiF monochromator can be reasonably assumed to contribute more to the asymmetry of peaks than does the existence of satellite lines such as those associated with Coster-Kronig transitions for the case of L X-ray emission spectra.

At Bragg angles greater than 30°, since the instrumental distortions are minimum, the width of L X-ray peaks remained larger than that of K X-ray peaks of similar energy. This difference is consistent with the difference in natural width of K and L emission lines.

However, the calculated instrumental resolution values Γ_i, were found to be different by applying equation 6 to K and L X-ray spectra analyzed with the LiF monochromator. The instrumental resolution derived from L spectra was higher than that derived from K spectra, even when using the threshold excitation mode in order to reduce the contribution of Coster-Kronig transition to the asymmetry of $L\alpha$ peaks. Thus, rather than an incomplete correction of instrumental distortion, the difference in the calculated Γ_i values more probably resulted from an overestimation of the calculated width of the $L\alpha$ peaks described by the pseudo-Voigt profile, subsequently minimizing the intensity of the non-diagram line. From the processing of Ti $K\alpha_{1,2}$ data using equation 6, we derived the instrumental resolution Γ_i. This value was set as a constant in the pseudo-Voigt profile to generate second order reflection for the Au $L\alpha$ diagram-line. The difference between the observed profile (2nd order reflection) and the calculated diagram-peak profile revealed a high energy tail whose area represented about 20% of the total area of the second order reflection for the Au $L\alpha$ emission band. This intensity ratio is consistent with the Au $L\alpha$ intensity enhancement due to Coster-Kronig transitions calculated by Lábár [44, 45].

In fact, based on equations 4 and 5, only a fraction of satellites can be observed while the others coincide with the so-called diagram line which is never a pure diagram-line, i.e., a line arising from a single electron jump in a single-hole state. Shake-off and Coster-Kronig processes contribute to the total satellite production. For L X-ray spectra, the observable satellites result mainly from LM states (Coster-Kronig transitions) and those which cannot be distinguished from the major peak arise from LN states. The "observed" or so-called diagram line consists of the pure diagram line and fine structures which, as mentioned in Krause et al. [42], might appropriately be called "parasites". Krause et al. [42] also showed that even in the absence of Coster-
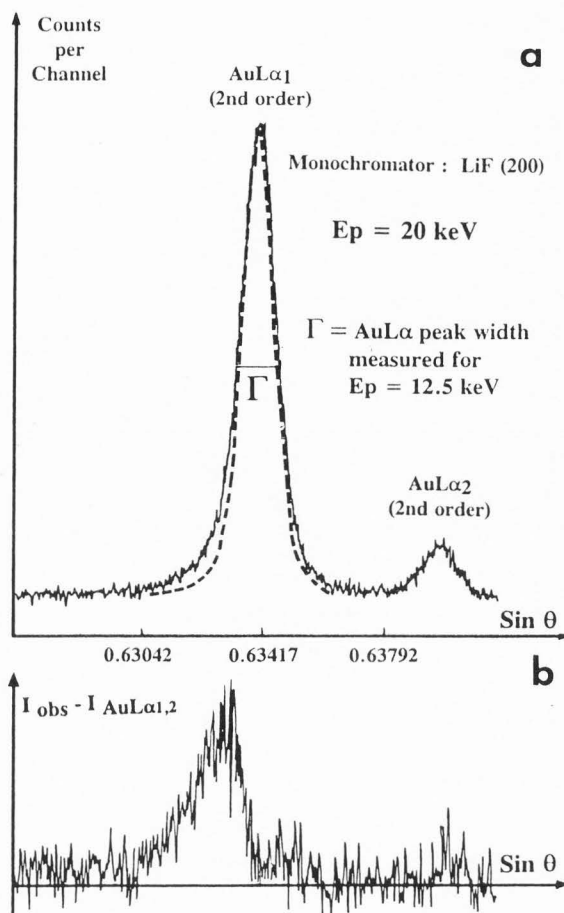
Figure 19. Second order reflection of the Au $L\alpha_{1,2}$ emission band analyzed with the LiF (200) monochromator, and a 20 keV incident energy. **(a)** Results of fit, and **(b)** residuals using the peak width calculated for the 2nd order Au $L\alpha_{1,2}$ peak analyzed at 12.5 keV incident energy.

Kronig transitions, systematics of shake-off will lead to substantial interference of parasite peaks with the analyzed L X-ray emission peak. In addition to the impossibility of experimentally measuring the pure diagram line and parasite line intensities, the latter contribute to distortions in the line shapes.

Practical Implications for X-Ray Intensity Measurements in Quantitative Analysis With the EPMA

Most of the $K\alpha$, $L\alpha$ and $M\alpha$ emission bands obtained with the spectrometers of an automated EPMA exhibited asymmetrical shapes resulting from either spectral
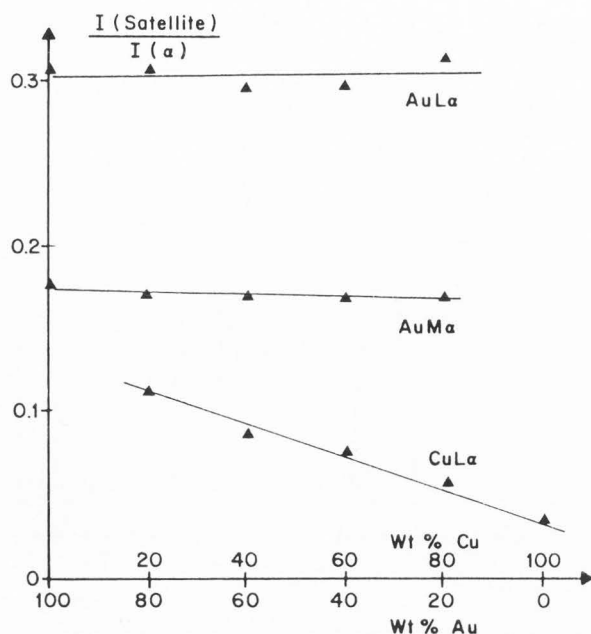
Figure 20. Au Lα, Au Mα and Cu Lα satellite to diagram line intensity ratios, respectively, as a function of the Cu-Au alloy composition.

----

distortion and/or the presence of high energy non-diagram lines. We investigated the influence of the asymmetry of peaks on the reliability of quantitative data using the three following approaches to derive X-ray peak intensities to be used in quantitative data processing procedures:

- peak height measurement by setting the monochromator at the Bragg angle and by varying the position to the nearby background;

- peak area of the diagram line derived from the fit of the experimental data to the pseudo-Voigt profile; and

- peak area of the total emission peak including both the diagram and the non-diagram lines.

Examples of copper-gold alloys

The Cu-Au SRM 482 reference alloys [47] were analyzed. Pure Cu and Au specimens were used as standards. The concentrations were obtained, by applying to the measured intensities, the PAP model [56] included in the data reduction software available with the EPMA used.

As shown in Figure 20, the Au Lα satellite to the Au Lα peak intensity ratio was found to be constant for all analyzed Cu-Au alloys. As previously discussed, the high energy tail to the Au Lα peak analyzed with the LiF monochromator is the sum of non-diagram lines

resulting from multiple hole configuration and of spectral distortion resulting from the monochromator mounting, simultaneously. The wavelength positions of both the diagram Au Lα peak and the Gaussian offsets are higher than that of the Au L$_3$ absorption edge, and no differential absorption by the matrix will affect the intensities of the pseudo-Voigt profile and Gaussian offsets. The contribution of the instrumental distortion to the observed tail is not affected by the matrix. Thus, for a given position of the monochromator, the intensity of the tail will remain proportional to the intensity of the diagram line.

As shown in Figure 20, the satellite intensity with respect to that of the Au Mα peak remained approximately constant when Cu-Au concentrations varied. The average mass absorption coefficient for Au Mα emission increases from 1431 for pure Au to 1853 for the specimen containing 20 wt% Au and 80 wt% Cu. Au Mα and satellite intensities are subjected to self-absorption within the targets of different composition, but no differential absorption occurs. Both Au Mα (0.584 nm or 2123 eV) and its satellite band (from 0.5807 nm to 0.5825 nm or from 2128 eV to 2135 eV) are located on the same side of the Au M$_5$ absorption edge (0.562 nm or 2206 eV). The absorption effect will thus remain in the same order of magnitude for both Au Mα and the satellite photons of equivalent energies and the satellite to Au Mα intensity ratios will remain independent of the absorption factor of the Cu-Au alloys.

The Cu Lα emission peak was analyzed at the surface of the pure Cu and the set of Cu-Au alloys using a 15 keV incident energy and a TAP monochromator. As shown in Figure 20, the intensity ratio between the non-diagram Cu LαS band and the Cu Lα diagram peak decreased linearly when the Cu concentration within the analyzed alloys was increased.

The error in deriving intensities from the fitting procedure mainly results in the uncertainty in choosing the value of C$_g$ in the pseudo-Voigt function (equation 1). It has been shown that a change in C$_g$ does not appreciably change the calculated peak width, but the shape at the valley of the peak strongly depends on that value. Consequently, the characteristics of the Gaussian offset(s) vary as a function of the C$_g$ value selected in the fitting function. The uncertainty in the fit is more particularly important for the case of satellite bands fully unresolved from the parent peak. **Describing the tail by Gaussian offsets is purely empirical**, and there is no physical criterion to either select the number of offsets to be used or to reduce the number of variables. For the case of the asymmetrical Cu Lα emission band, the error in the non-diagram to diagram intensity ratios was estimated to be ∼ 5% as a function of the variables used in the fitting procedure. However, the error in the

Table 12. Measured Cu concentrations in the SRM 482 Au-Cu alloys as a function of the procedure used for the Cu Lα intensity measurement. Incident energy: 15 keV. Standard: pure Cu. Data reduction by means of the PAP program [56].

Cu nominal wt %	Peak height wt %	Diagram peak area wt %	Total peak area wt %
80	80.5	80.1	81.5
60	60.6	60.2	61.2
40	40.9	40.3	42.2
20	20.6	20.5	21.9

Cu Lα intensity measurement is lower than the variation of the satellite Cu Lα intensity ratio we observed as a function of the analyzed Cu-Au alloys. Thus, the variations shown in Figure 20 for the intensity ratio between the satellite and the Cu Lα peak must be regarded as an effect of the specimen composition rather than an effect resulting from data processing. In pure Cu, the satellite band Cu LαS is preferentially absorbed relative to Cu Lα (see Fig. 6). Therefore, as we replace Cu by Au in the alloy (and Au has almost the same attenuation for Cu LαS and Cu Lα), the differential attenuation effect will decrease, and the ratio (ICu LαS/ICu Lα) should increase as we observed in experiments.

Although the origins of the high energy tail to the Au Lα and Au Mα peak are different, i.e., mainly instrumental distortion for the Au Lα peak and non-diagram band for the Au Mα peak, the intensity ratio between the Gaussian offsets and the pseudo-Voigt profile (equation 1) remained independent of the Cu-Au alloy composition. Consequently, **the measured Au concentration remained independent of the analytical procedure (i.e., peak height, diagram peak area, and total peak area) used to derive the X-ray intensities from the Au Lα and Au Mα emission spectra** on the pure Au element and the alloys.

Based on Figure 20, variations of the measured Cu concentrations in the Cu-Au alloys are expected to vary as a function of the analytical procedure used for obtaining the Cu Lα intensities. The Cu concentration in the set of Cu-Au alloys measured for a 15 keV incident energy are given in Table 12.

Table 12 shows that the nominal and measured Cu weight concentrations were in a good agreement using the Cu Lα intensity derived either from the peak height measurement procedure or the calculated peak area of the diagram Cu Lα emission. Using the total Cu Lα peak area, i.e., diagram Cu Lα peak and its high energy satellite band, led to a deviation between the calculated Cu concentrations and those obtained when neglecting
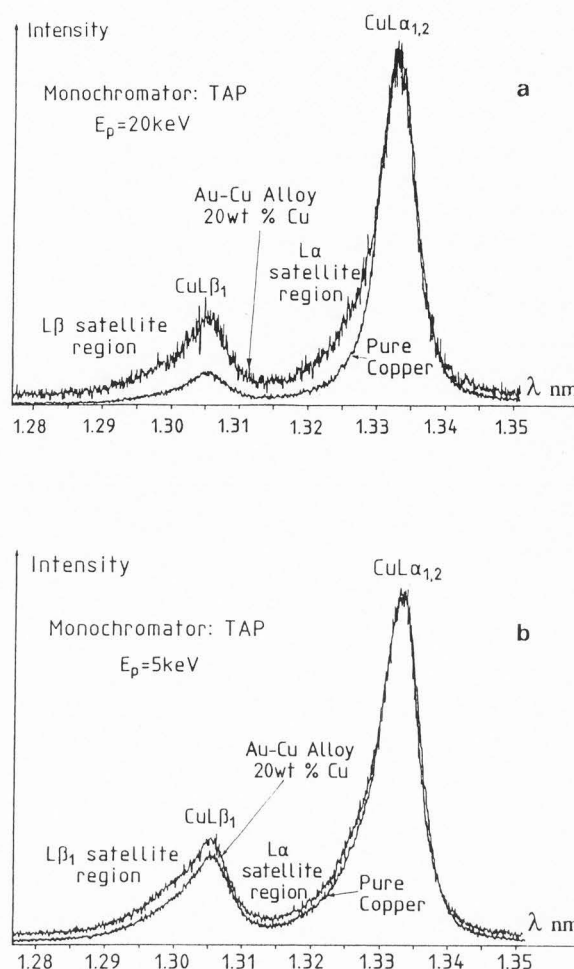
Figure 21. Cu Lα,β emission spectra of a pure copper target and a 20 wt% Cu in a Cu-Au alloy as a function of the incident energy (E_p): (a) 20 keV, and (b) 5 keV.

the contribution of the satellite intensity. The deviation between the two sets of calculated Cu fractions increased from 1.8% to 7% when the Cu concentrations decreased from 80 wt% to 20 wt%. These variations are consistent with those expressing the satellite to the Cu Lα intensity ratios (see Figure 20).

Using the total Cu Lα emission band area in the quantitative analytical procedure leads to a deviation between the calculated and the measured Cu concentrations. This deviation increases when the Cu concentration decreases because the non-diagram intensity relative to that of the diagram peak is lower for the pure Cu used as standard (strong differential absorption effect) than for the Cu-Au alloys.

It has been shown that the differential absorption for the Cu Lα diagram emission line and its high energy

109
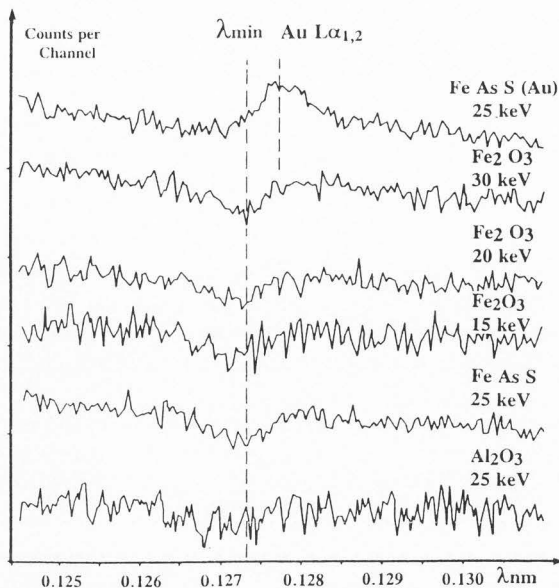
Figure 22. Continuous emission for several specimens and incident energies analyzed with the LiF (200) monochromator within a wavelength domain centered at the Au Lα emission peak.
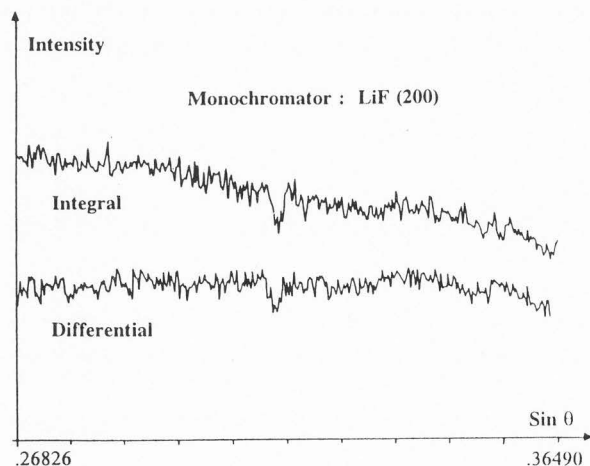
Figure 23. Continuous intensity distribution within a wavelength domain centered at the Au Lα emission peak position recorded by using the integral and differential mode of the pulse height analyzer.

----

satellite band are also functions of the incident energy, i.e., the absorption path length. Thus, for a given composition of the alloy, the deviation between the theoretical and calculated Cu concentrations will increase when

the incident energy is increased. This effect is shown in Figure 21 comparing the Cu Lα,ß emission spectra of pure Cu and a Cu-Au alloy specimen. However, reducing the incident energy, i.e., reducing the sampling depth below the specimen surface, will lead to measured data very sensitive to surface composition changes which may result from mechanical polishing or beam damage [61, 63].

Gold analysis at trace levels

The continuous emission associated with the Au Lα peak: We investigated the effect of the intensity measurement procedure when analyzing the Au Lα emission peak in specimens containing Au at trace levels. For this purpose, the shape of the continuous emission associated with the Au Lα peak was first carefully analyzed.

As shown in Figure 22, a sharp decrease in the continuous intensity was observed at $\sin\theta = 0.31650$, i.e., $\theta = 18.42°$. The position of the "hole" in the continuum remained independent either of the incident energy or of the nature of the specimen analyzed with the LiF monochromator. The "hole" in the background intensity did not result from multiple order reflections of the continuum intensity since the "hole's" position should vary as a function of the incident energy. Furthermore, the existence of the "hole" should be removed from the spectrum by energy discrimination using the automatic control of the pulse height analyzer (PHA) as a function of wavelength. As shown in Figure 23, the "hole" was still present using either the integral or differential acquisition mode successively. Only the slope of the continuum average intensity distribution versus wavelength was changed.

The position of the anomalous feature on the background intensity distribution does not exactly match the absorption edge of elements of components which could act as a filter along the X-ray path. We also verified that the "hole" occurred at the same position when the argon-methane gas was replaced by xenon in the proportional gas flow detector. In addition, the "hole" was not observed when analyzing the same wavelength domain with a quartz (10$\bar{1}$1) monochromator.

For all observations mentioned above, the presence of the "hole" at $\sin\theta = 0.31650$ must be associated with the LiF monochromator. However, this effect is not an artifact resulting from defects in the particular monochromator used because the same shape of the continuum was observed for all LiF monochromators installed on several EPMAs. The observed effect must be regarded as resulting from some intrinsic property of the actual crystal.

For the LiF (200) monochromator, the Bragg angle $\theta = 18.42°$ corresponding to the "hole" is significant

Monochromator : LiF (200)
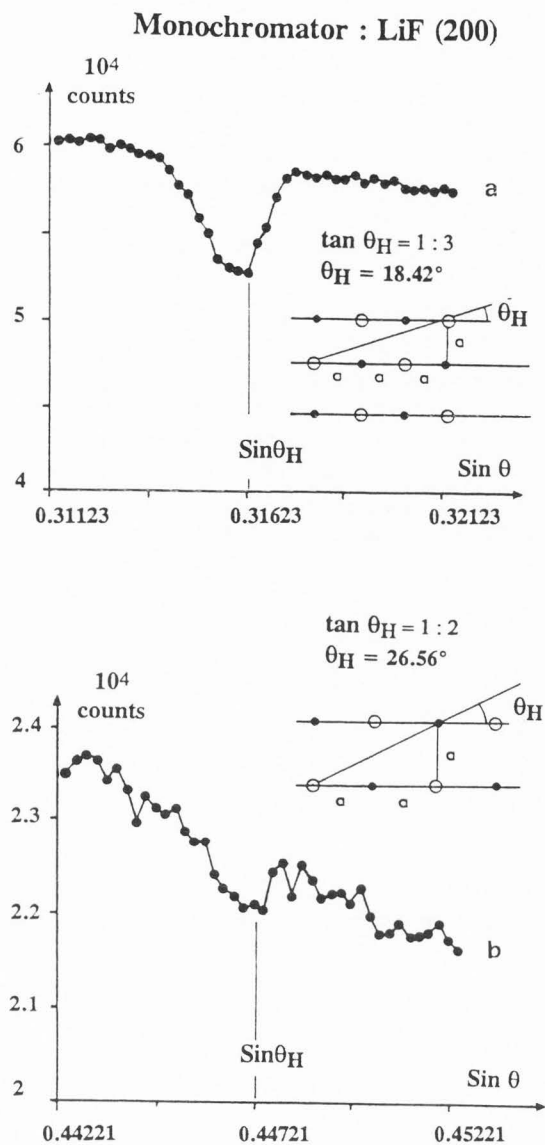
Figure 24. Experimental continuous intensity measurement around a Bragg angle value equal to (a) $\tan\theta = 1:3$, and (b) $\tan\theta = 1:2$.

---

because tangent θ (= 18.42°) = 0.333, meaning that there will be strong interference effects between X-ray photons and the scattering centers on the individual planes of the LiF monochromator as illustrated in Figure 24. The same effect should take place in other directions of special significance to the crystal lattice, i.e., the sharp decrease in intensity should also be observable with the LiF monochromator around the $\sin\theta$ values of 0.707, 0.447 and 0.245 corresponding to $\tan\theta = 1:1$, 1:2 and 1:4, respectively. As shown in Figure 24, a "hole" in the continuous spectrum was again observed near $\sin\theta = 0.4472$, i.e., $\tan\theta = 1:2$. However, the
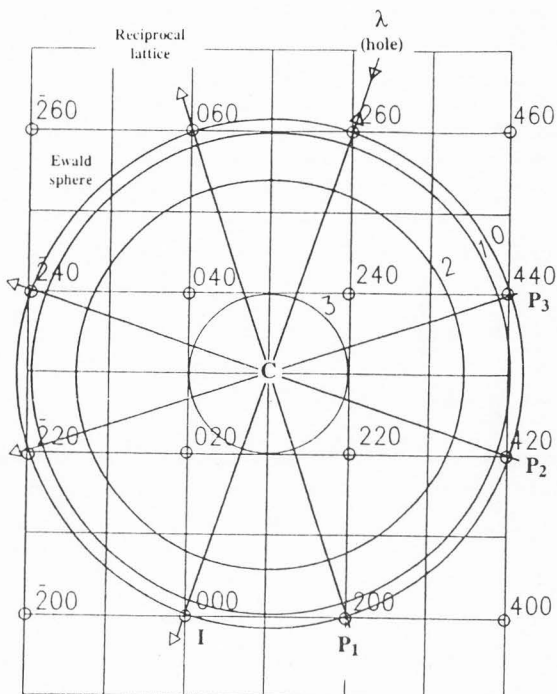
Figure 25. Graphical determination of the (hkl) planes of a LiF monochromator bent along the (200) planes, leading to multiple diffraction at Bragg angle corresponding to the "hole" in the continuous emission. C: location of the crystal; I: origin of the reciprocal lattice; CI: incident beam; and CP1, CP2, ...: X-ray beams diffracted by (200), (420), ... planes.

same features, expected around $\tan\theta = 1:1$ and 1:4, were not observed. The presence of the "hole" in the intensity distribution of the continuous emission can be related to multiple reflections on planes differently orientated below the monochromator surface according to a mechanism previously reported by Renninger [65]. Recently, Self *et al.* [74] calculated the positions of "holes" occurring at specific wavelengths in the continuous spectrum by considering diffraction from crystallographic planes different from the (200) of the LiF monochromator. For $2\theta = 36.87°$, corresponding to the "hole" in the background shown in Figure 22, Self *et al.* [74] calculated (see equation 22 in **Appendix**) that the diffracted intensity on the (200) planes decreases by an amount equal to the intensities diffracted in other directions by the (420), (006), (206), ($\bar{2}$04), (404) and ($\bar{2}$02) planes. The existence of the "hole" occurring at $\theta = 18.42°$ by using the LiF (200) monochromator can be easily illustrated from a crystallography viewpoint by using the reciprocal lattice of the LiF monochromator and the Ewald
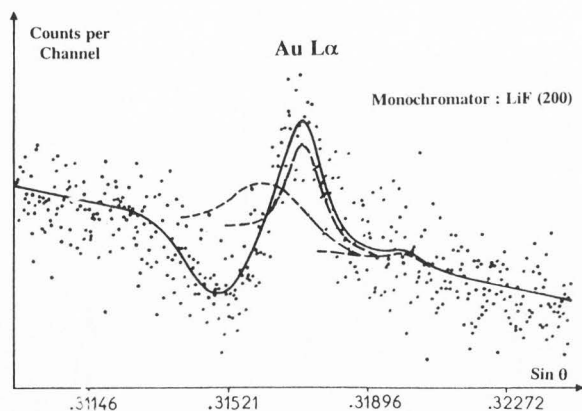
Figure 26. Au Lα emission peak {LiF (200) monochromator} measured at the surface of a gold ion implanted arsenopyrite (AsFeS) specimen. Results of fit including the pseudo-Voigt profile for the Au Lα diagram peak, a Gaussian offset representing the focusing defect due to the monochromator, and a Gaussian offset of negative amplitude representing the "hole" in the background.

----

sphere. Figure 25 illustrates the reciprocal lattice and the Ewald sphere for the particular incident wavelength corresponding to the "hole" in the continuous emission. This wavelength is reflected by the (200) lattice planes of the monochromator, the (200) reciprocal lattice point being located on the Ewald sphere. As shown in Figure 25, several reciprocal-lattice points, e.g., 420, 440, 220, ..., are also located on the Ewald sphere and multiple reflections may occur. A part of the intensity of the X-ray beam, CP_1, diffracted by the (200) planes is diverted to enhance the intensities of the diffracted beams marked CP_2, CP_3, ... in Figure 25.

Contribution of the continuous emission to the Au Lα peak shape: The hole at $\theta = 18.42°$ in the continuous emission of any specimens analyzed with the LiF (200) monochromator occurs in a wavelength domain containing to the Au Lα emission band.

Since the position of the anomalous continuum intensity decrease is a property of the monochromator, we derived an analytical expression for the continuum distribution within a narrow wavelength domain centered at the Au Lα peak position. For this purpose, Au free pyrite (FeS_2) and arsenopyrite (AsFeS) specimens, oxides, and pure elements were analyzed, and their continuum distributions $B(\lambda)$, within the wavelength interval 0.1246 nm $< \lambda <$ 0.1306 nm (i.e., 0.32944 $<$ $\sin\theta <$ 0.32444), were digitally recorded and processed using equation 7 as a fitting function:

$$B(\lambda) = a\lambda + b - H_H \exp[-\ln 2\{(\lambda-\lambda') / \Gamma_H\}^2], \quad (7)$$

where a is the slope of the average linear variation of the continuum intensity, b its ordinate at the origin of the scan ($\sin\theta = 0.3094$), H_H is the amplitude of a Gaussian distribution centered at the "hole" wavelength λ' and having a half-width (Γ_H) at half-maximum.

As shown in Figures 22 and 26, the position of the feature of negative amplitude with respect to the average linear distribution of the continuous emission intensity is very close to the position of the Gaussian offset describing the tail on the short-wavelength side of the Au Lα peak. At low Au concentrations, i.e., at low Au Lα peak to background ratios a change of the Au Lα peak shape, height and position may thus occur with respect to the Au Lα emission band of a pure Au specimen.

In order to obtain experimental X-ray spectra characteristic of Au present at trace levels (a few thousands of ppm), a Au ion implanted arsenopyrite (AsFeS) was analyzed. By varying the incident electron beam energy, thus varying the depth distribution of the X-ray excitation with respect to the depth distribution of the ion implant, the apparent Au concentrations were varied.

The Au implantation was 10^{15} atoms/cm². The depth distribution of the Au implant was derived from secondary ion mass spectrometry carried out by Chryssoulis *et al.* [19]. The maximum of the implant corresponding to 0.45 wt% of Au was located 236 nm below the specimen surface. The Au implant extended down to 400 nm in depth and was correctly approximated by the following Gaussian distribution:

$$C_A (\rho z) = C_0 \exp\{-K^2(\rho z-\rho z_0)^2\}, \quad (8)$$

i.e., a Gaussian of height C_0, centered at mass depth ρz_0 and having a full width at $1/e$ given by $2/K$.

In order to predict the Au Lα intensity which would be measured at the surface of the ion implanted specimen, the depth distribution of the Au concentration (equation 8) was combined with an analytical description of the depth ionization distribution as discussed by Packwood [52], Packwood and Remond [53] and Remond *et al.* [64].

The calculated Au weight concentrations predicted to be observed at the surface of the Au ion implanted arsenopyrite specimen were 0.15%, 0.21% and 0.25% for 25 keV, 20 keV and 15 keV electron beam energies, respectively [64]. The shape of the observed Au Lα emission peak as a function of the Au concentrations were studied, and the calculated concentrations were compared to the measured values derived from several Au Lα intensity measurement procedures. A pure metallic Au specimen was used for standardization and quantitation.

Table 13. Effect of the particular method used for estimating the Au Lα intensity on quantitative Au analysis in a Au implanted arsenopyrite (AsFeS) specimen. All data derived from the same spectrum measured for a 15 keV incident energy. See Fig. 27 for symbols used.

Calculated Au wt %	Measured Au concentrations			
	Peak height		Peak area	
	H_p-H_D	H_D	N_D-N_G	$N_D+N_G-N_H$
0.25	0.19	0.25	0.26	0.06

A difference equal to $24 \cdot 10^{-5}$ of the $\sin\theta$ value was observed between the Au Lα maximum position measured at the surface of the pure Au and the Au implant specimen, successively. The peak position observed for the case of the ion implanted is the net result of the true Au Lα emission peak and the "hole" in the continuous emission leading to a shift of the observed peak maximum with respect to that of the pure Au specimen. The peak position difference corresponds to a variation $\Delta I/I = 5\%$ for the intensity of the Au Lα peak measured at the surface of the Au implanted arsenopyrite specimen. The error in the measured concentration resulting from the shift between the peak maximum for the unknown and reference compounds successively was found to be lower than the error resulting from statistics and heterogeneity of the Au implanted distribution.

In order to avoid the effect of heterogeneities when comparing several intensity measurement procedures, all quantities shown in Figure 27 describing the symbols used for peak height and peak area measurements were derived from a single spectrum (Fig. 26). Quantitative data are shown in Table 13 for the case of the Au implanted arsenopyrite specimen analyzed with a 15 keV incident energy.

Using the peak height procedure, two measurements were performed. The first approach consisted in measuring the average number (H_T) of counts at the peak maximum, the intensity of the background (H_B) being obtained by linear interpolation of the two average values measured on both extremes of the digitally recorded scan shown in Figure 26. The second peak height measurement corrected for the background which resulted from using the calculated amplitude of the pseudo-Voigt profile (equation 1) describing the Au Lα diagram line in the fitting procedure.

Two different approaches were also used to obtain peak areas accounting for the existence of spectral distortions or ignoring their presence. Because the pseudo-Voigt profile has a symmetrical shape, the peak amplitude H_D or the peak area N_D of the Au Lα diagram peak will lead to the same quantitative results. As already shown for the case of the analysis of Cu-Au
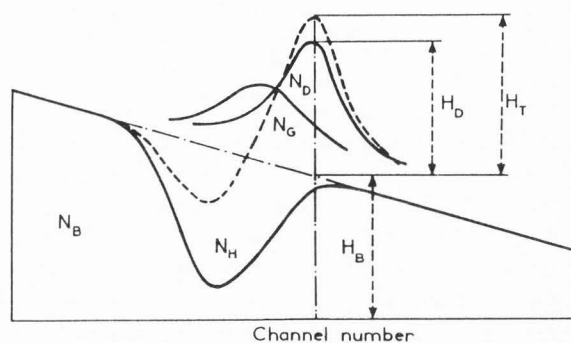
Figure 27. Symbols used for the intensity measurement of the Au Lα emission peak shown in Figure 26. H: peak height; and N: area of the components resulting from the fitting procedure.

---

alloys, the amplitude of the Gaussian offset correcting the focusing defect remained proportional to that of the Au Lα diagram peak (see Fig. 20). Consequently, using the total area $N_D + N_G$ of both the pseudo-Voigt profile and the instrumental Gaussian offset above the calculated background intensity (Gaussian offset with negative amplitude added to the linear function), led to good agreement with the expected Au concentrations derived from calculations as shown in Table 13.

Because the "hole" in the background and the asymmetry of the Au Lα peak occur within the same wavelength domain, these two features **cannot be experimentally distinguished** by a step by step analysis of the Au Lα peak. A peak area measurement procedure would consist of summing the number of counts at the successive channels analyzed by stepping the monochromator and in subtracting the background intensity assumed to linearly vary within the analyzed wavelength domain. The net integrated background intensity is equivalent to $N_B - N_H$, and the net integrated peak area N_I which should be measured is equivalent to:

$$N_I = N_D + N_G - N_H, \qquad (9)$$

using the notations in Figure 27.

As shown in Table 13, the use of integrated peak areas led to deviations between the measured and calculated Au concentrations. It has been shown that for a 25 keV incident energy, leading to an apparent Au concentration of ~ 0.15%, the method based on peak integration led to a negative Au Lα intensity [60]. The particular example of analysis of Au at trace levels indicates that the aim of improving the statistical precision by the use of peak integration may be accompanied in some circumstances by a decrease in the accuracy of quantitative data.

Discussion and Summary

Wavelength dispersive X-ray emission peaks obtained by means of the EPMA have been shown to be adequately described by a pseudo-Voigt function (equation 1), i.e., a linear combination of a Gaussian and a Lorentzian distribution, with the same amplitude and width, centered at the same wavelength and in relative proportion of C_g and $(1-C_g)$, respectively. The K, L and M X-ray emission peaks of pure elements were analyzed using LiF (200), PET (002) and TAP ($10\bar{1}1$) monochromators, respectively. These crystals were set on the Johann type mounts within the spectrometers of the EPMA. Most of the analyzed peaks exhibited weak features on their short wavelength side (high energy side). In most instances, these features were not resolved from the main X-ray peak whose shape was asymmetrical resulting from a shoulder on the high energy side. Gaussian offsets were empirically added to the pseudo-Voigt fitting function to account for the small bands leading to the asymmetry of peaks.

The two possible origins for the high energy shoulders were discussed, i.e., instrumental distortions and spectroscopic effects leading to the production of non-diagram (satellite) lines.

Due to the complex nature of the refractive index for X-ray frequencies, the diffraction pattern for a cylindrically bent crystal (Johann mounting) is asymmetrical. The major source of line broadening is the focusing defect arising from X-rays impinging the monochromator far from its center, and a pronounced **asymmetry on the short wavelength side** of the diffraction pattern occurs **at low Bragg angles** (see **Appendix**). Line broadening must be minimized when using X-ray diffraction spectrometry for measurements of the natural width of X-ray emission lines. For this purpose, experiments are carried out at very high Bragg angles. For spatially resolved qualitative and quantitative chemical analysis, modern computer controlled EMPA's are equipped with linear focusing spectrometers. Most of the available crystals are installed in the Johann mounting type. In order to keep the take-off angle of the analyzed X-rays with respect to the specimen surface constant, the monochromator is moved along a straight line originating at the beam spot (point source), the orientation of the crystal being changed along its trajectory. At low Bragg angles, the X-ray source is at a short distance to the monochromator. The rigorous focusing conditions are no longer satisfied and large variations of the Bragg angle values occur at the surface and in the thickness of the monochromator (see **Appendix**). **The intensity of the reflection band will become lower and broader when the distance between the point source and the monochromator is decreased, and a pronounced asymmetry on the short wavelength side of the diffraction pattern is expected at low Bragg angles**.

Comparisons between first and second order reflections given by the same monochromator and comparisons between peak profiles analyzed by two different monochromators showed that for emission peaks occurring at Bragg angles lower than 30°, the asymmetry mainly resulted from instrumental distortions and that possible high energy satellite lines were hidden by such effects. Multiple reflection on differently oriented planes below the monochromator surface may also lead to a decrease in intensity of the diffracted rays at **specific** Bragg angles (see **Appendix**). Such an effect has been shown to exist when analyzing the continuous emission in a narrow wavelength domain containing the Au Lα emission band with a LiF (200) monochromator.

For emission peaks not distorted by instrumental factors, the residual difference between the experimental data and the theoretical shape of the diagram emission peaks exhibited an asymmetrical shape. Most of the data available in the literature related to the production of high energy satellites are based on the analysis of X-ray emission spectra using ultra-high vacuum environment and high resolution spectrometers using gratings or double-crystal monochromators. It has been shown that satellite features from known physical phenomena are easily detected by the use of commercial EPMA designed for repetitive analysis on a routine basis. In such equipment, the monochromators have a resolution much larger than the intrinsic width of the analyzed X-ray emission lines. However, these available instrumental conditions were sufficient to detect structures representing the **envelope of satellite lines**.

For Kα emission peaks, the high energy satellites we measured were consistent with experimental and theoretical data on satellites associated with simultaneous vacancies in the K or L or M levels. The outer L or M vacancy produces a change in the electrostatic potential, leading to shifts in the energy levels. The energy separation between the satellites and the parent lines were found to increase linearly with atomic number.

For Lα,ß emission peaks of first series transition elements, high energy satellites have been detected. These features extended a few eV from the diagram Lα,ß lines. The energy separations we measured for the high energy satellite bands to the Cu Lα,ß and Zn Lα,ß parent peaks were found to be consistent with satellites resulting from a de-excitation mechanism of the L_3 and L_2 initial vacancies in the presence of outer vacancies created by shake-off or Coster-Kronig transitions. Owing to self absorption for the generated photons by the matrix, the intensity of the satellite band may vary as a function of the incident energy, i.e., the absorption path-length. When the L_3 and L_2 absorption edges lie

between the satellite bands and the $L\alpha$ and $L\beta_1$ diagram lines, respectively, the satellite band suffers a more pronounced attenuation than the parent peak. The intensity ratios between the non-diagram and diagram lines will strongly depend on the incident energy as we showed for the case of the Cu $L\alpha,\beta$ emission peaks analyzed with the TAP monochromator. For an element with $Z > 29$, the L_3 and L_2 absorption edges have higher energies than those of the satellite bands and the $L\alpha$ and $L\beta$ diagram peaks, and consequently, no differential absorption occurs as was the case for Zn $L\alpha,\beta$ peaks [24, 63].

For L emission peaks of elements $36 < Z < 56$, analyzed with a PET monochromator, the high energy satellite positions were consistent with calculated energy shifts resulting from outer vacancies. These multiple-vacancy states arise primarily due to the Coster-Kronig process. This attribute was supported by studying the satellite-to-parent line intensity ratios as a function of the atomic number of the analyzed elements. For atomic numbers $Z = 36$ to $Z = 56$, the $L\alpha$ satellite-to-diagram line ratios exhibited a sharp decrease for $Z \geq 49$, and the $L\beta$ satellite to diagram line ratio exhibited a jump near $Z \approx 39$. The discontinuous behavior of the intensity ratios corresponds to the L_1-$L_{2,3}M_{4,5}$ Coster Kronig transition thresholds. The L_1-$L_2M_{4,5}$ transitions are energetically allowed for $Z \leq 39$ and the L_1-$L_3M_{4,5}$ transitions for $Z \leq 49$.

For high energy $L\alpha$ X-ray lines of elements with high atomic number such as Au, Hg, Pt ... analyzed with the LiF (200) monochromator, it was not possible to accurately detect satellite lines. The first order reflection for these high energetic X-ray emissions occurs at Bragg angles lower than $30°$. Even using the excitation threshold conditions to selectively excite the L_1, L_2 and L_3 subshells, we were not able to differentiate the presence of high energy satellites from spectral distortions resulting from the monochromator. Furthermore, for these elements, high energy satellites resulting from Coster-Kronig transitions were not successfully resolved from the second order reflection lines which were expected to be free of instrumental distortions arising from their corresponding Bragg angles. As an example, the measured peak width of the Au $L\alpha$ second order reflection was found to be greater than that calculated by quadratic addition of the instrumental resolution and the intrinsic width of the emission line (equation 6). The observed excess of width have been tentatively attributed to unresolved high energy satellites resulting from Coster-Kronig transitions consistent with $L\alpha$ intensity enhancement due to Coster-Kronig non-radiative transition calculated by Lábár [45].

A Coster-Kronig mechanism within the M subshells has also been associated with the high energy satellite as illustrated for the case of the Au $M\alpha$ emission peak by

varying the incident electron energy with respect to the M_1 to M_2 energy ionization thresholds.

By varying the incident energy, it has been shown that the shape of X-ray emission bands was changed as a result of self-absorption for the diagram and the non-diagram lines by the matrix. **For metallic specimens**, the effect of self-absorption on the positions of the satellite peaks is relatively low. However, determining the relative intensities of diagram and satellite lines requires a reasonably detailed knowledge of the absorption edge structure as a function of energy in the region of interest. Two extreme situations must be considered for predicting the shape of an X-ray emission peak for a pure metallic target. The first corresponds to X-ray peaks exhibiting an asymmetrical shape resulting mainly from the presence of satellites whose intensities are submitted to self-absorption. The dependence of an X-ray peak upon self-absorption by the matrix is more particularly pronounced when an absorption edge lies between the satellite band and the diagram peak as we illustrated for the case of the Cu L emission band for pure Cu and metallic Cu-Au alloys. The second situation, leading to peak shape changes as a function of self-absorption phenomena, corresponds to satellite free X-ray spectra whose asymmetrical shape only reflects the absorption structure of the material as illustrated by Fischer and Baun [29, 30] for the case of the $M\beta$ and $M\alpha$ emission peaks of the rare-earth elements (0.76 nm $< \lambda < 1.499$ nm). The self-absorption effect has a strong influence on the peak shape and peak position and is often referred to as **"chemical effect"**. However, as discussed by Fischer and Baun [29, 30] the influences of chemical binding and self-absorption must be considered separately in order to obtain a reliable interpretation of band shapes, relative intensities, and wavelength shifts. When the bonding is **metallic**, there is only little change in the X-ray emission band position relative to that from the pure metal as we observed in the present study for the Cu $L\alpha$ emission band from pure Cu and Cu-Au alloys while the shape of Cu $L\alpha$ emission band was strongly dependent upon self-absorption by the matrix.

For **non-metallic** specimens, changes of the line shape (width and asymmetry) as a function of chemical bond occurring with the $K\alpha_{1,2}$ emission lines of the 3d and 4d elements have been reported by Finster et al. [27]. However, using EPMAs equipped with Johann type monochromators, $K\alpha$ and $K\beta$ peak shifts as a function of chemical bonding only become easily detectable for elements $Z < 22$ (Ti) analyzed with PET and TAP crystals. For these elements, the accuracy of quantitative EPMA data strongly depends upon the choice of the reference materials. In addition to peak shifts, peak shape changes are observed for low Z elements because $K\alpha$ transition concerns the valence electrons. This has

been illustrated by Fialin *et al.* [26], Fischer [28], and Solberg [76] for the case of F Kα emission, and by Fischer [28], and Fialin and Remond [25] for the case of the O Kα emission. Wavelength shifts and changes in shape of soft X-ray emission bands from the compound relative to the metals are a function of the amount of ionic character in the bond. The influences of chemical bonding and self-absorption of some long wavelength X-ray emission spectra such as Kα,β emission of elements Z < 14 and Lα,β emission spectra of first series transition metals, have been illustrated by Fabian [23], Fischer and Baun [29, 30], Henke and Taniguchi [32], and Holliday [33], among others.

While the detailed analysis of an X-ray emission peak may provide information on chemical bonding, the effect of the electronic structure on the shape of an X-ray emission band is a source of difficulty with quantitative analysis with the EPMA. For quantitative WDS X-ray analysis, the experiments showed that the peak height procedure for X-ray peak intensity measurement is a good enough approximation for most applications. This approach neglects X-ray peak alterations as a function of the electronic structure of the analyzed specimens. However, the error resulting from differences in X-ray emission spectra for the unknowns and the standards remains generally low because it is commonly accepted to use standards close in composition to those of chemically complex analyzed materials.
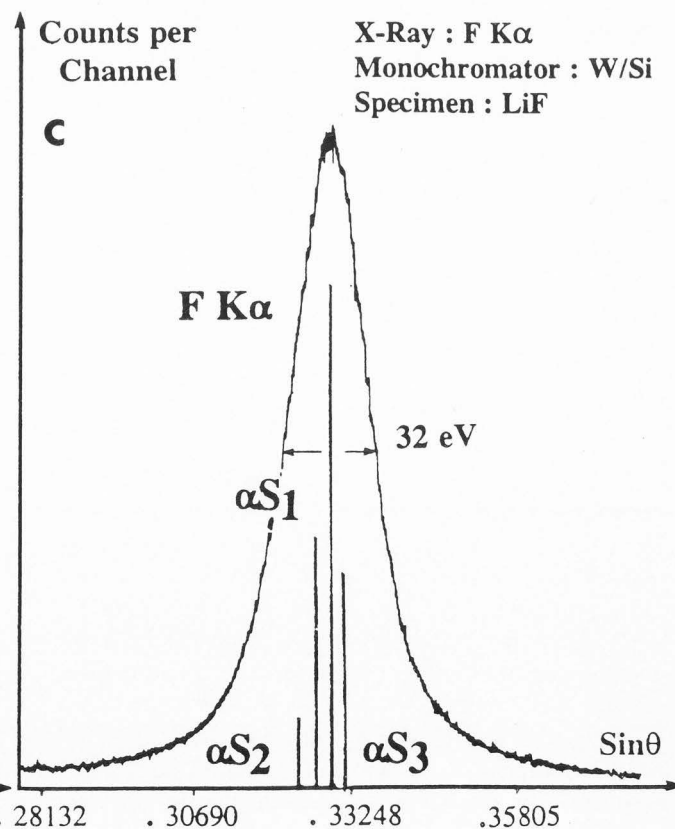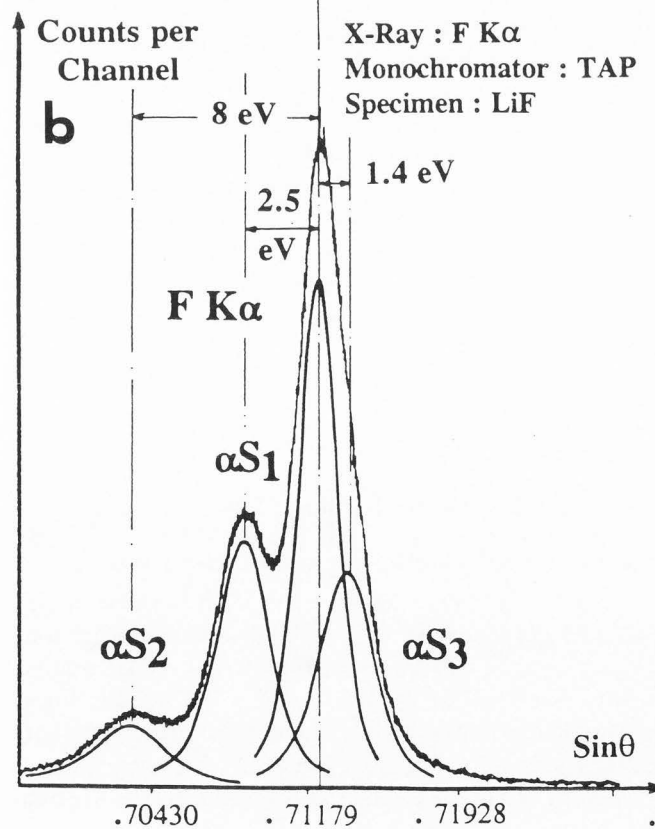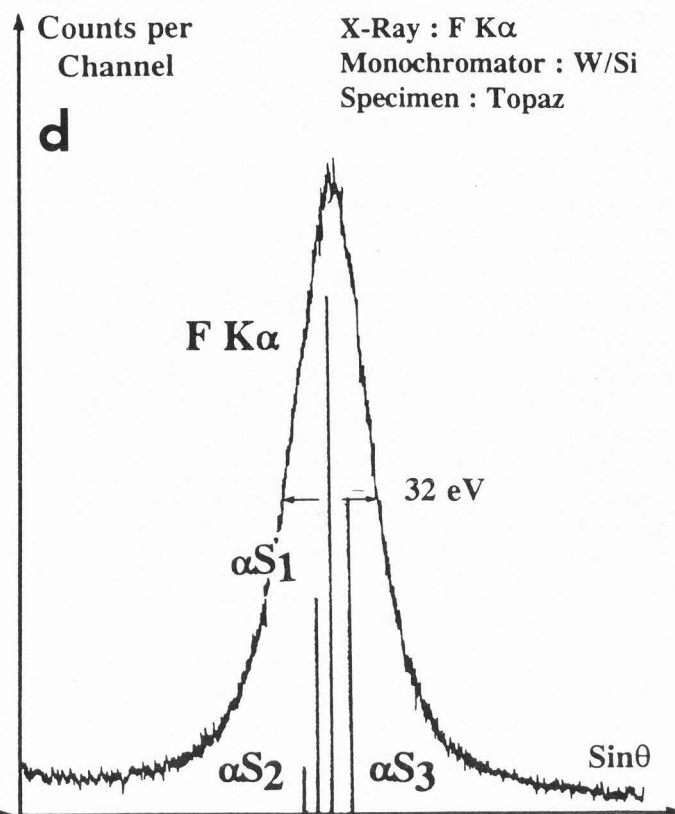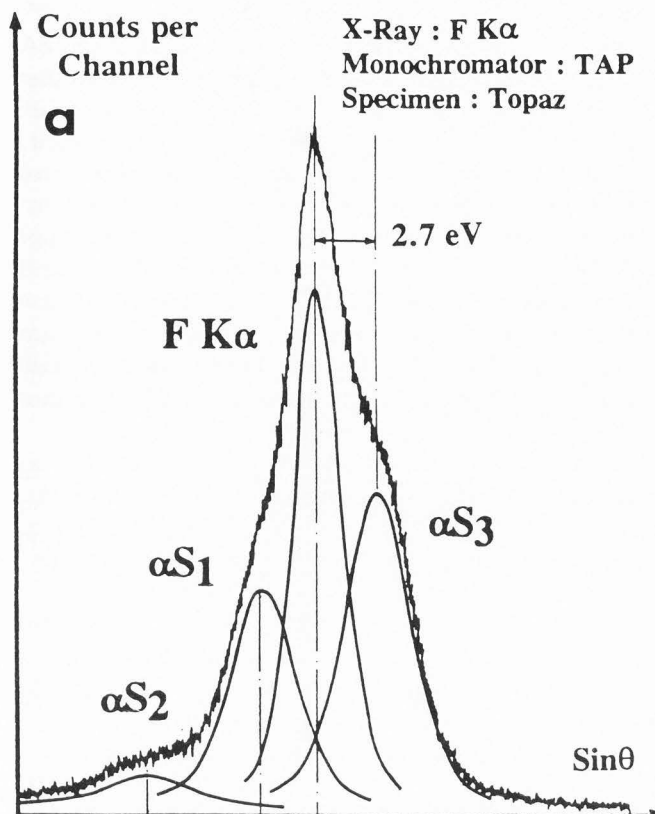
From a practical point of view, with modern computer-controlled EPMA, the **peak height** measurement in quantitative analysis should be replaced by that of **peak areas** obtained by summing the number of counts within each successive channel analyzed by stepping the monochromators. This will provide a more accurate representation of the quantity of interest, namely the total number of emitting atoms. Such a replacement is justified by the need for an improved accuracy in determination of trace and minor elements. Peak integration obviates the need for re-calibration when peaks are shifted in wavelength by chemical bonding. In this regard, two further consequences of bonding a specific element in different compounds should be noted. First, the altered outer electron states can result in a shift of intensities among the emission lines, and second, they can alter the Coster-Kronig rates which redistribute vacancies, with a resulting change in relative line intensities. The possibility of such intensity changes again argues for using standards that are chemically similar to the materials analyzed.

Peak integration would also be preferred in the presence of chemical shift to avoid recalibration to correct for peak shifts as illustrated by Remond *et al.* [63] for the Zn Lα emission peak measured in pure Zn, Zn oxide and Zn sulfide crystals. Peak integration has been

Figure 28 (on the facing page). F Kα line analyzed by means of (**a, b**) TAP monochromator and (**c, d**) W/Si multilayer synthetic crystal for (**a, c**) a LiF specimen; and (**b, d**) for a topaz $(Al_2SiO_4(F,OH)_2)$ specimen.

---

shown to be necessary for the analysis of the F Kα emission in a variety of minerals as illustrated by Fialin and Remond [25] and by Fialin *et al.* [26]. As shown in Figure 28a, for a topaz $(Al_2SiO_4(F,OH)_2)$ specimen, in addition to the high energy satellites resulting from multiple outer vacancies in the L subshells, a low energy satellite band (Fig. 28a) was also observed distant by 5 eV from the major F Kα line analyzed with a TAP monochromator. This low energy satellite was not detected on the F Kα spectrum measured from the surface of a LiF specimen (Fig. 28b). As shown in Figures 28c and 28d, none of the fine features was isolated from the F Kα peak analyzed with a W/Si multilayer monochromator leading to the same F Kα shape for all F bearing compounds. At this low Bragg angle (~ 18°), corresponding to the F Kα (λ = 1.83 nm) for the W/Si monochromator, the observed peak shape is the net result of instrumental distortions diagram and non-diagram emission bands. However, peak area by integrating the number of counts in the successive channels or by fitting the experimental data to a pseudo-Voigt function (equation 1) and Gaussian offsets is no longer applicable when strong self-absorption effects contribute to spectral distortions. Such a situation is often encountered for soft L X-ray emission bands of the first series transition elements. As shown in the present study for the Cu Lα emission in metallic alloys and by Fialin *et al.* [26] for the Cu Lα emission in a variety of Cu bearing minerals, the direct measurement of peak areas led to inconsistent measured and calculated k-ratios. Rather than to use the area-peak factor concept to account for the non-proportionality between peak height and peak area [3, 4], a method based on **peak decomposition** should be preferred in order to derive reliable X-ray peak intensities from complex X-ray emission spectra.

The use of a pseudo-Voigt function (equation 1) and Gaussian offsets has been proven to be sufficient to describe most of the observed X-ray spectra by means of the EPMA. However, in absence of theoretical data and an accurate knowledge of the response function of the monochromator, the spectral decomposition is difficult to apply. This is particularly true when extending the spectral decomposition procedure used in the present study to the soft X-ray domain analyzed with multilayer synthetic crystals as illustrated in Figure 28 for the F Kα emission band. The positions and intensity ratios of the satellite bands with respect to those of the diagram peak were derived from the F Kα emission spectra obtained

a

Counts per Channel

X-Ray : F Kα
Monochromator : TAP
Specimen : Topaz

2.7 eV

F Kα

αS₁

αS₂

αS₃

Sinθ

d

Counts per Channel

X-Ray : F Kα
Monochromator : W/Si
Specimen : Topaz

F Kα

32 eV

αS₁

αS₂   αS₃

Sinθ

b

Counts per Channel

X-Ray : F Kα
Monochromator : TAP
Specimen : LiF

8 eV

2.5 eV

1.4 eV

F Kα

αS₁

αS₂

αS₃

Sinθ

.70430   .71179   .71928

c

Counts per Channel

X-Ray : F Kα
Monochromator : W/Si
Specimen : LiF

F Kα

32 eV

αS₁

αS₂   αS₃

Sinθ

.28132   .30690   .33248   .35805

with the TAP monochromator. Keeping these values as constants in the fitting procedure of the F Kα spectrum analyzed with the W/Si monochromator did not lead to a satisfactory fit because the shape of the diagram line, i.e., the value C_g to be used in equation 1 remained unknown.

The intensity of an X-ray emission line, i.e., the area of the observed line shape must include both diagram and non-diagram contributions as discussed by Lábár [45] and by Pouchou and Pichoir [57] for the case of standardless quantitative analysis by means of an EDS. Because the energy resolution of WDS is greater than that of an EDS, the envelope of satellite lines is observed in WDS. Thus, **the theoretical description of an X-ray emission must account for absorption phenomenon modifying the intensity ratio between the non-diagram and diagram lines as a function of the incident energy and the matrix composition.**

For K, L and M soft X-ray bands, the effects of self-absorption upon the line shape and relative intensities of X-ray lines must be identified for predicting X-ray spectra. As noted already for the case of first series transition elements, the self-absorption effect can be approximated by measuring the observed intensity ratio of high to low energy generated spectra. This approach can be refined using a Phi(ρz) correction [44]. However, these calculations may become inaccurate for the case of insulating materials because the creation of electrical fields modifies the electron trajectories as discussed by Cazaux [15, 16]. This second step avoids the assumption that the low energy data are absorption free. A second alternative is to use thin films [71] which inherently have low absorption. Certainly such data have relatively small corrections for self-absorption and are generally the preferred source of spectra.

As a summary, the familiar peak height measurement to obtain X-ray peak intensity from WDS spectra is a sufficient approximation for most quantitative analysis purposes with the EPMA. However, it must be kept in mind that for obtaining a satisfactory accuracy of quantitative data the **use of appropriate standards is necessary in order to avoid errors resulting from peak shape changes and peak shifts** between the X-ray spectra. However, WDS **peak decomposition** should be preferred to empirical factors for correcting raw data for the case of severe peak overlap, e.g., L and M X-ray emission spectra of rare earth elements or for departure of peaks from symmetry, e.g., soft X-ray emission bands. Furthermore, **peak decomposition** should be preferred to peak area measurement in order to correct peak shape alterations resulting from matrix effects, e.g., **self-absorption and chemical effects**. In the conventional analytical schemes used for quantitative analysis with the EPMA, the

absorption correction factor is applied to the measured intensity derived either from the peak height or the peak area measurement procedure. A more accurate procedure should include the absorption correction into the spectral decomposition procedure in order to account for matrix effect on the X-ray line shape, i.e., the measured X-ray peak area. For this purpose, absorption free X-ray spectra of pure elements must be collected in order to obtain an accurate data base for generating theoretical X-ray spectra. These spectra, convoluted with the response function of the spectrometer and accounting for the matrix composition, should be used in a single least-square fitting procedure to improve the accuracy of WDS and EDS quantitative analysis in the soft X-ray region.

The observed X-ray intensity never results from a mechanism involving a single subshell. Both instrumental factors and satellites resulting from de-excitation mechanisms in the presence of multiple vacancies contribute to the observed X-ray line shape.

By the use of the monochromators available with commercial EPMA, it is often difficult to distinguish between both origins of the spectral distortions which are more or less pronounced depending upon the energy of the analyzed X-ray peaks and the specimen composition. For quantitative analysis with the EPMA, it is thus difficult to propose a unique answer, allowing us to decide when spectral decomposition must be used rather than peak integration in order to derive, from experimental measurements, quantities which are proportional to the number of the emitting atoms. Before starting an analytical procedure, it is necessary to carefully optimize: **i)** the choice of the X-ray line and consequently, the monochromator to be used in order to minimize peak broadening and asymmetry, and **ii)** the incident energy in order to minimize the self-absorption phenomenon because this effect selectively modifies the intensity and the shape of the diagram and non-diagram bands and varies with both the binding and the atomic number.

Appendix

Non-diagram lines: An overview

High energy satellites: Multiply-ionized atoms with simultaneous vacancies may lead to a broadening and a shifting to higher energies of X-ray peaks.

K Lines: Simultaneous vacancies may occur in the K shell and an outer shell due to either double ionization by the electron or to outer-shell shake-off that results from the filling of the K vacancy. The satellite lines resulting from the presence of outer vacancies consist of a number of closely spaced features. The energy separation distance between the satellite band and the Kα line

ranges from 10-40 eV for atomic number $12 < Z < 30$ (Watson *et al.* cited in [8]; Bhattacharya *et al.* [8]). Aberg [1] presented an extensive set of values for the relative intensity of the satellite decreasing from about 30% for $Z = 10$ to 0.5% at $Z = 30$.

Double ionization of the K-shell is also possible; the one electron de-excitation of the K^{-2} double vacancy results in a hypersatellite [2, 67] whose separation from $K\alpha$ is some 250 eV for the 3d transition elements [40]. However, the intensities of these hypersatellites are very weak. For example, Saijonma and Keski-Rahkonen [67] reported values of 10^{-5} to 10^{-4} for the intensity ratio of the $K\alpha$ hypersatellite/diagram intensity ratio in the electron bombardment of iron and chromium.

L and M lines: The de-excitation of an L or M level in presence of outer holes may also lead to the presence of high energy satellites to L or M X-ray peaks. The additional outer vacancies may result from Coster-Kronig transitions or shake-off mechanisms.

The $L\alpha,\beta$ lines for transition metals have been studied by Parratt [55] and Bonnelle [10]. Recent reviews of $L\alpha$ lines for these elements have been published by Bonnelle [11], Fabian [23], and Hanzely and Liefield [31]. According to these authors, several line shape distortions can be distinguished depending on the incident electron energy region.

1) The threshold excitation region: When the incident energy lies between the L_3 and L_2 energy thresholds, multiple vacancy satellites are largely reduced.

2) The satellite region: The $L\alpha$ diagram line becomes distorted by the progressive development of high energy satellites when the incident electron energy increases from the L_3 subshell threshold up to about three times that value. The fine structure observed on the high energy side of the $L\alpha$ peaks for transition elements using low incident energy (< 2 keV) is mostly attributed to a complex of satellite lines that arise from multiple vacancies. Two mechanisms can give rise to the LMM double vacancy state responsible for the satellite feature. The first is the direct indistinguishable process of shake-off. The second arises when an initial L_1 subshell vacancy is filled by an L_1-$L_3M_{4,5}$ Coster-Kronig transition.

3) The self absorption region: For incident energies greater than about 3 or 4 times the L_3 threshold energy, the fine structure vanishes and the effect is attributed to self-absorption. Increasing incident electron energy also increases the absorption path within the specimen of the generated X-ray photons and self-absorption removes the fine structure when a high incident energy is used. It was observed [23] that the ratio of the intensities for two extreme spectra, measured using high and low energies successively, gives a self-absorption spectrum.

Since the final states of the $L\alpha,\beta$ lines of the transition elements are valence hole states, the profiles of the $L\alpha,\beta$ emission spectra will change with the electronic structure of the material.

The X-ray satellite lines accompanying $L\alpha$ lines for elements $36 < Z < 56$ have been reviewed by Randall and Parratt [59]. As an order of magnitude, Olsen *et al.* [51] reported the energy separation distance between the satellite lines and the $L\alpha$ line to be 85 eV, 12 eV, and 5 eV for Sn when L_3 level de-excites in presence of an additional vacancy on the L_2, $M_{4,5}$ and N shells, respectively. Thus, three classes of satellites may result from double L_3L, L_3M and L_3N configuration, the latter one being generally unresolved from the diagram $L\alpha$ line. However, the unresolved satellites resulting from L_3N double holes may represent an important contribution to the intensity of the $L\alpha,\beta$ diagram lines [42]. High energy satellites, resulting from Coster-Kronig transitions, do not exist for all elements and the intensity of the satellites will exhibit cut-off thresholds at specific atomic numbers. In the electronic rearrangement concomitant to the initial ionization event, the shake-off process can have a significant role in some cases [41].

High energy satellite bands to $L\alpha,\beta$ lines have been observed under proton, heavy ion, photon, and electron irradiation, their intensities depending on the nature of the incident projectile.

Similarly, high energy satellites to $M\alpha$ lines of elements with high atomic number result from the M_5 hole de-excitation in presence of simultaneous vacancies in the M_5 and N subshells. Only the envelope of satellites resulting from additional vacancies in the M_5 subshell can be distinguished from the diagram line.

Low Energy Contributions: The radiative Auger effect (RAE) produces a broad structure in K X-ray spectra which is less energetic than the characteristic diagram K line [38, 75]. The RAE process results from a de-excitation of a K vacancy, similar to an Auger process with simultaneous emission of a bound electron and an X-ray photon. For atomic number $15 < Z < 30$, Keski-Rahkonen and Ahopelto [38], and Servomaa and Keski-Rahkonen [75] showed that the low energy structures associated with the $K\beta_{1,3}$ diagram line can be interpreted in terms of KMM radiative Auger effect. These structures have been observed for the case of photon, electron, or proton incident energy. Their intensities are in the order of magnitude of a few percent or less of the $K\beta_{1,3}$ line intensity and they extend over typically 200 eV in energy. Similarly, less-intense, low-energy structures associated with K lines may result from KLL and KLM radiative Auger effect.

Several theories are available to describe the $K\beta'$ low energy features associated with the $K\beta_{1,3}$ emission resulting from transitions involving the partially filled 3d
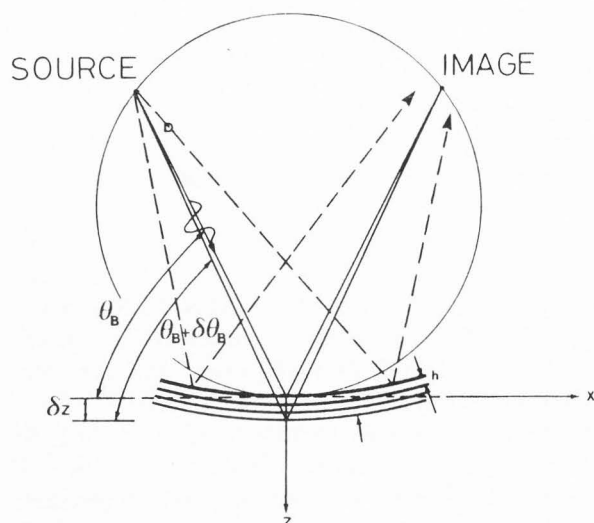
Figure 29. Focusing curved crystal monochromator of the Johann type.

----

shells of transition elements and their oxides. The Kβ' low energy bands are generally referred to as satellites although they are not satellites in the previous sense. The theories involve interaction between the electrons in the incomplete 3d shell and the hole in the incomplete 3p shell resulting from the K$\beta_{1,3}$ radiative transition. Salem *et al.* [70] showed that this interaction splits both 3p and 3d levels, causing a demultiplication of transitions. The Kβ' satellite has also been explained in terms of the plasmon oscillation theory [77]. During the X-ray emission process, the transition valence electron excites a plasmon in the valence band. The transition energy of the K$\beta_{1,3}$ line will thus be shared between the plasmon and the emitting photon which will be deprived of an energy equal to the plasmon energy. For the transition elements, the energy separation distance between the Kβ' satellite and K$\beta_{1,3}$ diagram line is in the order of magnitude of 10 eV and depends upon the chemical environment [79].

The theories concerned with the production of Kβ' satellite associated with the K$\beta_{1,3}$ line of transition elements were extended to the case of the L X-ray spectra of the lanthanide elements. The Lβ_2, Lβ_4, Lγ_1 and Lγ_2 emissions exhibiting low energy effects are associated with transitions involving the partially filled 4f shell. The energy separation distance between the low energy satellite and its parent line is in the order of magnitude of a few tens of eV [69, 78].

The energy separation distance and the relative intensity of the non-diagram lines and bands with respect to their parent lines depend upon the atomic number of the element and the nature of the incident energy. It is

thus impossible to propose a unique model summarizing the possible origins of satellite and other bands, keeping in mind that not all of the features mentioned above will be present simultaneously.

In practice, all of the emissions are characterized by an intrinsic width and only the convolution of these features with the spectral window (or energy response function) of the spectrometer will be observable. Thus, the ability to observe the non-diagram satellite bands will depend on the resolution and sensitivity of the spectrometer used.

Peak shape resulting from instrumental factors

The observed photon distribution P(E) within an X-ray emission peak is expressed as:

$$P(E) = \int L(E') F(E-E') dE', \qquad (10)$$

where L(E) is the physical photon energy distribution and F(E) is the instrumental response function, E is the energy of the X-ray line, and E' the variable energy. The response function, F(E), expresses the observed line shape of an incident monoenergetic photon assumed to have a natural width equal to zero or negligible with respect to the energy resolution of the spectrometer.

The X-ray spectrometers used with the EPMA are slitless focusing spectrometers using a crystal (or multilayer structures) bent to yield a concave cylindrical surface. The X-ray spectrometer is in a symmetrical Bragg configuration, i.e., the incident and "reflected" rays are located on the same side of the monochromator surface, the reflecting planes (hkl) being parallel to its surface.

In Johann mounting, a flat crystal is cylindrically bent to twice the focal circle radius so that the focusing conditions are only satisfied for X-ray beams incident at the "center" of the monochromator, i.e., the point where the focal circle is tangent to the crystal surface (Fig. 29). Deviation from the focusing condition will increase, the farther the incident X-ray beam is from the "center" of the monochromator. Away from the "center" of the crystal, the small distance between its surface and the focal circle will give rise to a focusing defect resulting in a broadening and a decrease in intensity of the observed X-ray peak.

The characteristics of a bent monochromator, such as angular and linear dispersion, resolving power and reflecting power, can be derived from those of a perfect plane crystal as discussed by Cauchois and Bonnelle [14]. Two theories are available to treat the diffraction of X-rays, i.e., the **kinematic** theory and the **dynamic** theory.

The kinematic theory of diffraction of X-rays by a crystal lattice is a geometrical theory based on the Laue interference condition expressed by the Bragg equation:

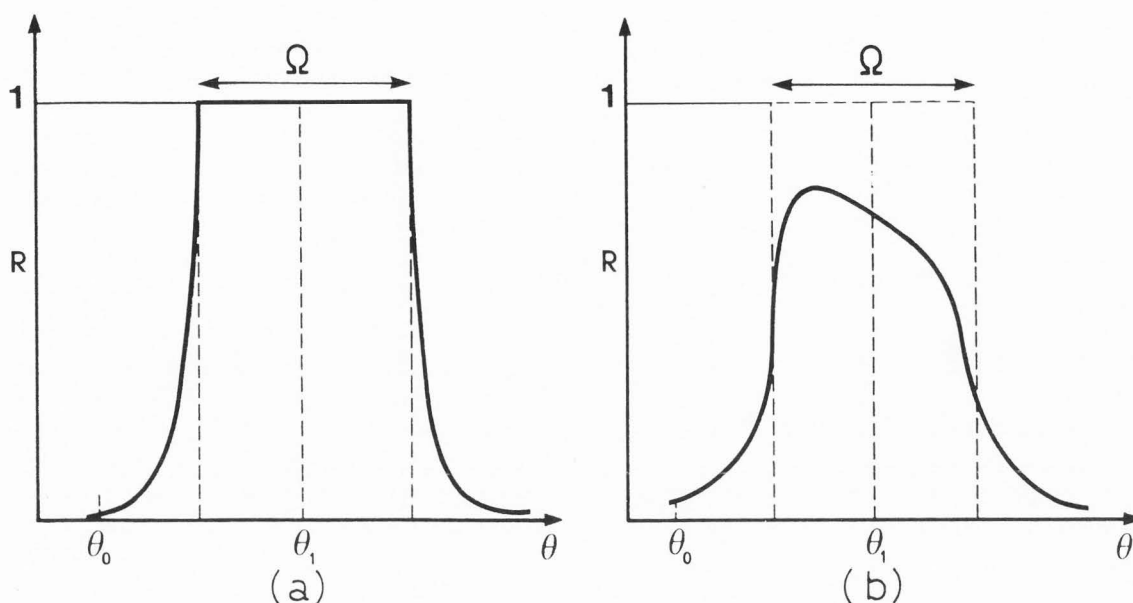$$m\lambda_B = 2d \sin\theta_B, \qquad (11)$$

Figure 30. Darwin band for a perfect plane crystal (**a**) without and (**b**) with absorption based on Cauchois and Bonnelle [14].
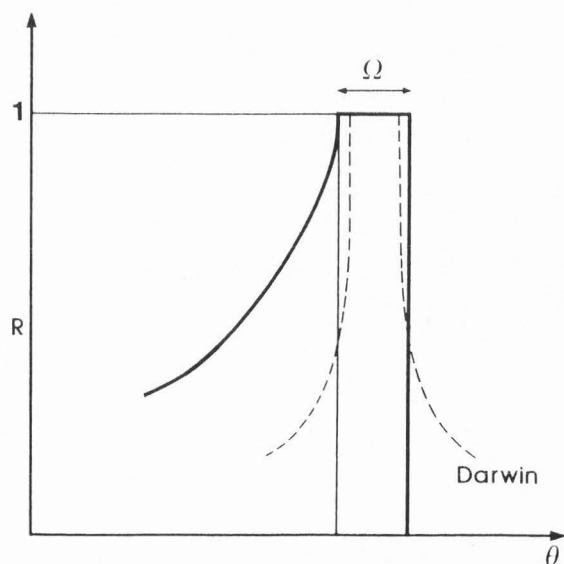

Figure 31. Diffraction pattern of a curved crystal based on Cauchois and Bonnelle [14].

----

where d is the spacing distance of the crystal, θ_B is the angle of incidence of the X-ray beam with respect to the crystal surface, and m is an integer corresponding to the order of reflection. In the kinematic theory, the **refraction index** of the medium for the incident beam is assumed to be **unity** so that the refraction and the absorption of waves are neglected. The kinematic theory

applies only if the crystal volume is small enough to neglect the phenomena mentioned above. The use of the dynamic theory is necessary for the case of a large perfect crystal.

For a large perfect crystal, it is necessary to take into account (**a**) the loss of intensity due to diffraction; (**b**) the phase difference between the incident wave reaching each plane and the wave scattered in the forward direction; and (**c**) the effect of multiple reflections.

For X-ray frequencies, the refractive index $\hat{n}$ is complex:

$$\hat{n} = n - i\beta. \tag{12}$$

The real part of the refractive index, n, is slightly lower than unity and the decrement $\delta = 1 - n$ characterizes the dispersion. The imaginary part, β, of the refractive index is the extinction coefficient. It is related to the ordinary linear absorption coefficient μ by:

$$\beta = (\lambda/4\pi)\,\mu. \tag{13}$$

The refractive index being complex, the extinction coefficient introduces a decrease of the amplitude of the waves passing through the crystal and phase changes between the incident and successively reflected waves. The refraction ($n = 1 - \delta$) and the absorption (extinction coefficient β) lead to a small angular shift of the reflectivity maximum position with respect to that derived from the Bragg relation (equation 11). The generalized Bragg law accounting for refraction resulting from the complex nature of the refractive index (equation 12) is:

$$m\lambda = 2d \{1-(d/\sin^2\theta)\} \sin\theta, \qquad (14)$$

where δ is the decrement to unity of the real part of the refractive index, and θ is the observed peak maximum.

By comparing equations 11 and 14, the shift of the "center" of the observed band (λ) from the Bragg value (λ_B) is:

$$(d\lambda/\lambda_B) = (\delta/\sin^2\theta_B). \qquad (15)$$

The observed peak profile will depend on the reflectance coefficient R (θ) of the crystal for the direction θ with:

$$R (\theta) = I_R/I_0, \qquad (16)$$

where I_R and I_0 are the intensities of the reflected and incident X-ray beams, respectively. The graph of R (θ) as a function of θ is the **diffraction pattern** of the crystal. The reflectance coefficient is a function of the refractive index.

Neglecting the absorption due to the photoelectric effect and the incoherent scattering, Darwin [20] studied diffraction by perfect crystals taking into account the three effects mentioned above. Darwin [20] showed that the reflection from a perfect crystal should be total over a narrow angular range Ω; outside this range the reflection diminishes rapidly and symmetrically. The Darwin diffraction pattern is shown in Figure 30a. Due to absorption resulting from the complex nature of the refractive index, i.e., extinction of the amplitude and phase changes between the waves, the diffraction pattern of a perfect plane crystal lies below the Darwin curve and has an asymmetrical shape as illustrated in Figure 30b.

The theories developed for a perfect plane crystal can be extended to the case of a bent crystal. In a symmetrical system, the curved Bragg planes are parallel to the crystal surface. As shown in Figure 29, the Bragg angle near the top surface is slightly smaller than that deeper into the crystal. The effect on Bragg reflection for monochromatic rays diverging from the source after reflection from an elastically bent perfect crystal is equivalent to the effect of a flat crystal with linearly varying Bragg spacing (see Fig. 29):

$$(dh/h) = \{(h \cos2\theta) / (D \sin2\theta)\}, \qquad (17)$$

where D is the distance of the point source from the first plane of the curved crystal.

The varying interplanar distance as a function of depth leads to a shift of the reflectance maximum with respect to that of the Bragg position and, an asymmetrical shape of the reflectance curve.

Approximating the Darwin curve for a perfect plane crystal by a rectangle of width Ω and assuming a constant mean value of the primary extinction coefficient

over this range, Cauchois and Bonnelle [14] showed that the resulting Darwin curve for the bent-crystal is made-up of adjacent rectangles of decreasing height as shown schematically in Figure 31. The asymmetrical-shaped diffraction pattern in Figure 31 represents the response function at the Bragg angle θ for a cylindrically bent perfect crystal.

The efficiency of curved crystals has been studied, among others, by Belin *et al.* [5] and by Berreman [6, 7] using the dynamical theory of X-ray diffraction. Figure 32a shows a typical computed curve of symmetrical point-to-point reflectance by a perfect crystal of uniform Bragg spacing.

For a crystal bent with a long radius of curvature, the reflectance curve remains very similar to the Darwin band of a flat monochromator. For short radius of curvature, the angle of reflection will change appreciably as a function of depth below the crystal surface leading to an exponentially decreasing tail (Fig. 32b). The tail exhibits oscillatory peaks resulting from interferences between rays reflected at different depths (Fig. 32b).

The calculated oscillatory features shown in Figure 32b have not been measured experimentally because of their very weak amplitudes. However, the average shape of the reflectance curve in Figure 32 derived from dynamic theory calculations [6, 7] is very similar to that shown in Figure 31 according to Cauchois and Bonnelle [14]. Based on this similarity, we will only recall the expressions for the broadening of the X-ray diffraction pattern calculated according to Cauchois and Bonnelle [14].

The total instrumental line width (ΔL) due to the curved crystal will be the sum of three terms:

$$\Delta L = \Delta L_1 + \Delta L_2 + \Delta L_3, \qquad (18)$$

where ΔL_1 represents the line width along the focal circle, ΔL_2 the line width resulting from the focusing defect for X-ray impinging the crystal far from its "center", and ΔL_3 is the line width resulting from the focusing defect due to the finite height of the crystal.

The line width ΔL_1 arises from the intrinsic nature of multiple reflections inside the monochromator. According to Cauchois and Bonnelle [14], the line width ΔL_1 along the focal circle, i.e., for rays incident near the "center" of the crystal so that the source and its image are on the same focal circle of radius R, is:

$$\Delta L_1 = R\Omega + (\cos\theta/2\mu) \ln2. \qquad (19)$$

The first term, $R\Omega$, corresponds to a symmetrical contribution to the shape of the observed line and the second term, $(\cos\theta/2\mu) \ln2$, expresses an asymmetrical tail occurring on the short wavelength side of the peak (see Fig. 31).

According to Cauchois and Bonnelle [14], the line width L_2, due to departure from the Bragg conditions in the median plane of the crystal, is given by:

$$\Delta L2 \approx (\vartheta^2/8R) \cot\theta, \qquad (20)$$

where ϑ is the linear opening of the crystal and R the focal circle radius.

For the point-to-point symmetrical Bragg case (Fig. 29), the gas-flow detector is placed at the point image of the point source, both of them being located on the same focal circle. All incident X-rays exactly satisfying the Bragg conditions are collected and the measured X-ray intensity is maximum. A small deviation from the Bragg conditions is equivalent to a slight change of the focal circle position, leading to a decrease of the collected intensity with respect to that which should be measured in the exact focusing conditions. The exact point-to-point focusing are no longer satisfied for X-rays originating from the point source located on the focal circle and impinging on the monochromator far from its "center" (see Fig. 29) or by slightly moving the point source outside the focal circle. Both focusing defects (in the depth and in the median plane of the crystal) will create a loss in the measured intensity and a broadening of the peak. The broadening will occur because the crystal, being at a given position, will reflect a broad range of wavelengths intersecting widely separated focal circles. Consequently, the response of the detector will be maximum only for those wavelengths that are reflected at the exact or near exact Bragg conditions for the crystal-detector assembly.

In addition to changes in the Bragg angles, both at the surface and in the depth of the crystal, for X-ray beams in the focal plane, Bragg angle changes will also occur in the direction normal to that plane. The effect of the height, h, of the monochromator is a line broadening called **fanning divergence**. This effect is low for the case of a point X-ray source, as with the EPMA, and may not be negligible for large sources such as in X-ray fluorescence. According to Cauchois and Bonnelle [14], the line width (ΔL_3), due to the height focusing defect is:

$$\Delta L_3 \approx (h^2/8R) \sec\theta \csc\theta \qquad (21)$$

For a symmetrical reflection geometry, the crystal opening leads to a focusing defect causing **asymmetrical broadening toward the short-wavelength side** [14]. The effects of divergence on Bragg conditions in the focal plane and the perpendicular direction may cancel each other as discussed by Birks [9], and it has been shown that the points satisfying the Bragg conditions are contained in a X-shaped area at the surface of a cylindrically bent crystal.
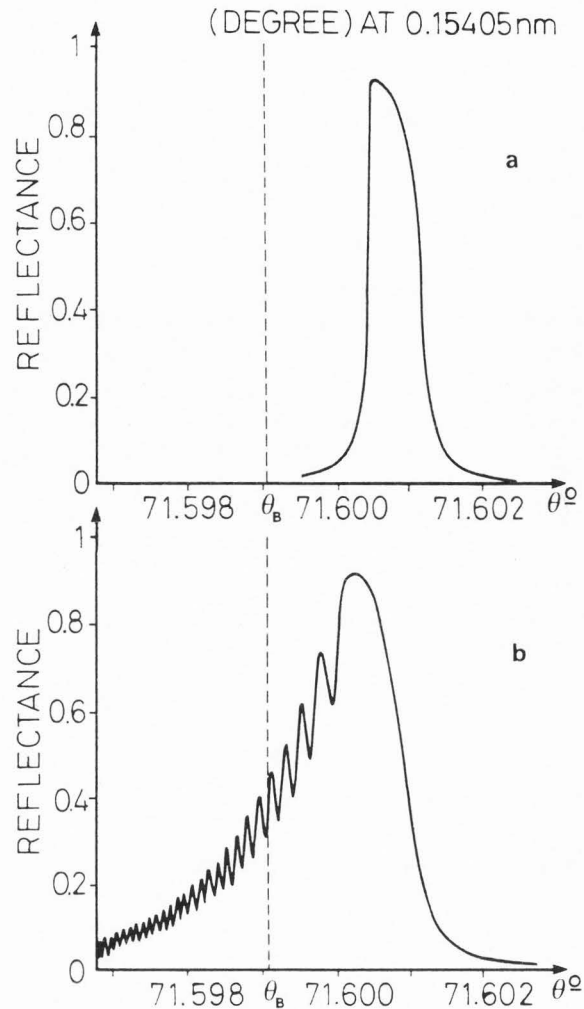
Figure 32. Darwin reflection band of (**a**) an ideal thick flat unstrained quartz monochromator (502 planes) around the Cu Kα_1 line, and (**b**) after bending the (502) planes quartz monochromator (based on Berreman [7]).

The asymmetry of the diffraction pattern given by a bent crystal results from focusing defects in all three dimensions of the crystal. As shown by equations 19, 20, and 21, the observed peak width varies as a function of the Bragg angle. The lower the Bragg angle, the higher is the line broadening due to focusing defects. Reducing the linear opening (equation 20) will minimize the focusing defect resulting from departure from a point-to-point focusing condition (point source and point image being both located on the focal circle) when a bent crystal is used. The line broadening ΔL_2 for X-rays far from the "center" of the crystal, cancels for

a curved crystal of the Johansson type, i.e., when the Bragg focusing conditions are satisfied for all X-rays impinging the crystal surface.

The line broadening ΔL_1 (equation 19) arises from the thickness of the crystal with respect of the penetration of the incident wave leading to multiple reflection of the X-rays on the successive planes. Interferences occur due to phase changes between the successive reflected X-rays. At high Bragg angles, or for high absorption of the incident photons, only the outer surface of the crystal reflects the beam, and the crystal behaves as a perfect crystal so that in equation 19 the second term is negligible. At low Bragg angles, or for high energy X-rays penetrating deep in the crystal, the second term in equation 19 is no longer negligible, and an asymmetric diffraction pattern is found. The line broadening (ΔL_1) due to the thickness of the crystal will affect all incident X-rays impinging upon the surface along the focal circle. Such a broadening effect will occur either for Johann or Johansson curved crystal mountings because the Bragg angle changes as a function of depth into the crystal.

Another source of line broadening contribution to the total instrumental line width, ΔL (equation 18), for a symmetrical reflection geometry using a bent monochromator is the possible reflection of the X-ray beams by crystallographic planes not parallel to the crystal surface. In a single crystal, diffraction can occur from any atomic plane. The simultaneous excitation of two or more reflections was observed by Renninger [65] and called "Umweganregung", i.e., "indirect reflection". The term "multiple reflection" is now more often used. The multiple reflection may lead to spurious behavior of the diffraction pattern. Anomalous intensity of the continuous emission occurring at specific wavelengths has been attributed to multiple reflections by Self *et al.* [74] for the case of LiF (200 planes) monochromator.

The monochromator is assumed to be bent along the (hkl) planes. If an X-ray beam makes an angle θ with the (hkl) planes and an angle θ' with the (h'k'l') planes, the same wavelength will be diffracted by the two sets of planes when:

$$2d \text{ (hkl) } \sin\theta = 2d'(h'k'l') \sin\theta'. \qquad (22)$$

In such a situation, diffraction by the (h'k'l') plane will cause a decrease in the intensity of the primary beam to be diffracted by the (hkl) planes.

Acknowledgements

References

[1] Aberg T (1927) Theory of multiple ionization processes. Proc. Int. Conf. Inner Shell Ionization Phenomena. U.S. Atomic Energy Comm. Conf. 720404. 1509-1542.

[2] Ahopelto J, Rantavuori E, Keski-Rahkonen O (1979) $K\alpha^h$ hypersatellite spectra in photon excitation and K shell double photoionization cross-section for transition metals Ti, Cr, Fe and Ni. Phys. Spectra 20, 71-74.

[3] Bastin GF, Heijligers HJM (1986) Quantitative electronprobe microanalysis of ultra-light elements. J. Micros. Spectrosc. Electron. 11, 215-228.

[4] Bastin GF, Heijligers HJM (1991) Quantitative electron probe microanalysis of ultra-light elements (Boron-Oxygen). In: Electron Probe Quantitation. Heinrich KFJ, Newbury DE (eds.). Plenum Press, New York, 145-162.

[5] Belin E, Zuckerman S, Sénémaud C (1984) Reflective properties of Beryl and Gypsum crystals in the 1 keV photon energy region. X-Ray Spectrom. 13, 46-48.

[6] Berreman DW (1976) Dynamical theory of X-ray diffraction in flat, focusing and distorted crystals by Abele's matrix method. Phys. Rev. B 14, 4313-4317.

[7] Berreman DW (1979) Curved X-ray monochromator efficiency. Phys. Rev. B 19, 560-567.

[8] Bhattacharya J, Laha U, Talukdar B (1988) Model for X-ray energy shifts for additional atomic vacancies. Phys. Rev. A 37, 3162-3168.

[9] Birks TS (1963) Electron probe microanalysis. In: Chemical Analysis, Vol. XVII. Elving PJ, Kolthoff IM (eds.). Interscience Publishers, New York, 73-92.

[10] Bonnelle C (1966) Contribution à l'étude des métaux de transition du premier groupe, du cuivre et de leurs oxydes par spectrométrie X dans le domaine de 13 à 22 Å (Contribution to the study of the first series metals, copper and oxides by means of X-ray spectrometry in the 13 to 22 Å). Doctorate Thesis, University of Paris. Masson and Co., Paris, France.

[11] Bonnelle C (1987) X-Ray Spectroscopy.

Annual Report C. The Royal Society of Chemistry, London, 201-272.

[12] Campbell JL, Wang JX (1991) Improved model for the intensity of low-energy tailing in Si(Li) X-ray spectra. X-Ray Spectrom. **20**, 191-197.

[13] Campbell JL, Perujo A, Millman BM (1987) Analytic description of Si(Li) spectral line shapes due to monoenergetic photons. X-Ray Spectrom. **16**, 195-201.

[14] Cauchois Y, Bonnelle C (1975) X-ray diffraction spectrometry. In: Atomic Inner-Shell Processes, Vol. II: Experimental Approaches and Applications. Crasemann B (ed.), Academic Press, 84-121.

[15] Cazaux J, Le Gressus C (1991) Phenomena relating to charge in insulators: Macroscopic effects and microscopic causes. Scanning Microsc. **5**, 17-28.

[16] Cazaux J, Lehuede P (1992) Some physical descriptions of the charging effects of insulators under incident particle bombardment. J. of Electron Spectroscopy and Related Phenomena **59**, 49-71.

[17] Chen MH, Crasemann B (1981) Widths of fluorescence yields of atomic L-shell vacancy states. Phys. Rev. A **24**, 177-182.

[18] Chen MH, Crasemann B (1984) M X-ray emission rates in Dirac-Fock approximation. Phys. Rev. A **30**, 170-176.

[19] Chryssoulis SL, Cabri LJ, Lennard W (1989). Calibration of the ion microprobe for quantitative trace precious metal analyses of ore minerals. Econ. Geol. **84**, 1684-1689.

[20] Darwin CG (1913) Cited in: Cauchois Y, Bonnelle C (1975). X-ray diffraction spectrometry. In: Atomic Inner-Shell Processes, Vol. II: Experimental Approaches and Applications. Crasemann B (ed.). Academic Press, 84-121.

[21] Doyle BL, Shafroth SM (1979) L_1-$L_{2,3}M_{4,5}$ Coster-Kronig transitions thresholds in the region $37 \leq Z \leq 56$. Phys. Rev. A **19**, 1433-1439.

[22] Doyle BL, Chambers WF, Christensen TM, Hall JM, Pepper GH (1979) Sine Θ settings for X-ray spectrometers. At. Data Nucl. Data Tables **24**, 373-493.

[23] Fabian D (1971) Soft X-ray band emission from solids. CRC Critical Reviews in Solid State Sciences, CRC Press, 255-316.

[24] Fialin M (1990) Some considerations on the use of $L\alpha$ series of transition metals in electron probe microanalysis: the example of zinc minerals. X-Ray Spectrom. **19**, 169-172.

[25] Fialin M, Remond G (1992) Problems with oxygen analysis in the system MgO-Al_2O_3-SiO_2 with the electron microprobe. In: Proc. 1992 Annual Meeting Electron Microscopy Society of America. San Francisco Press, 1624-1625.

[26] Fialin M, Henoc J, Maurice F, Remond G (1993) Quantitative analysis using soft X-ray spectrometry with the electron probe microanalyzer. Scanning Microscopy Suppl. **7**, 153-166.

[27] Finster J, Leonhardt G, Meisel A (1971) On the shape and width of the main lines of X-ray K emission of the 3d and 4d elements. J. Phys. (Paris) Colloque C4, **342**, 218-224.

[28] Fischer DW (1965) Effect of chemical combination on the X-ray emission spectra of oxygen and fluorine. J. Chem. Phys. **42**, 3814-3821.

[29] Fischer DW, Baun WL (1967a) The influence of sample self-absorption on wavelength shifts and shape changes in the soft X-ray region: The rare-earth M series. Adv. X-ray Analysis **11**, 230-240.

[30] Fischer DW, Baun WL (1967b) The influences of chemical combination and sample self-absorption on some long wavelength X-ray emission spectra. Norelco Reporter **XIV** (3-4). Philips Electronic Instrument, Special Issue: Ultra Soft X-Rays, 92-98.

[31] Hanzely S, Liefield RJ (1971) An L-series X-ray spectroscopic study of the valence bands in iron, cobalt, nickel, copper and zinc. In: Electronic Density of States. LH Bennett (ed.). National Bureau of Standards (USA), Spec. Publ. **323**, 319-327.

[32] Henke BL, Taniguchi K (1975) Valence band spectroscopy in the ultrasoft X-ray region (50 to 100 Å) Adv. X-Ray Anal. **19**, 627-641.

[33] Holliday JE (1967) The use of soft X-ray fine structure in bonding determination and light element analysis. Norelco Reporter **XIV** (3-4). Philips Electronic Instrument, Special Issue: Ultra Soft X-Rays, 84-91.

[34] Huang TC, Lim G (1986) Resolution of overlapping X-ray fluorescence peaks with the pseudo-Voigt function. Adv. X-Ray Anal. **29**, 461-468.

[35] Jamisson KA, Hall JM, Oltjen J, Woods CW, Kauffman RL, Gray TJ, Richard P (1976) Single-photon two electron-rearrangement transitions. Phys. Rev. A **14**, 937-945.

[36] Juslen H, Pessa M, Graeffe G (1979) $L\alpha$ X-ray spectra of elements between ^{40}Zr and ^{48}Cd. Phys. Rev. A **19**, 196-201.

[37] Kawai J, Maeda K (1991) Charge-transfer multiplet in the $L\alpha$ X-ray emission spectra of Copper (II) compounds. Spectrochimica Acta **46B**, 1243-1251.

[38] Keski-Rahkonen O, Ahopelto J (1980) The K $\rightarrow M^2$ radiative Auger effect in transition metals: II. J. Phys. C: Solid State Phys. **13**, 471-482.

[39] Keski-Rahkonen O, Krause MO (1977) Uranium M X-ray spectrum. Phys. Rev. A **15**, 959-966.

[40] Keski-Rahkonen O, Saijonmaa J, Suvanen M, Servomaa A (1977) $K\alpha^h$ hypersatellite spectra and K shell double photoionization cross sections of elemental Mg, V, Cr, Mn and Fe. Physica Spectra **16**, 105-108.

[41] Krause MO (1971) Rearrangement of inner shell ionized atoms. J. Phys. (Paris) Colloque C4, **32**,

67-75.

[42] Krause MO, Wuilleumier F, Nestor CW Jr (1972) Interpretation of the L X-ray emission spectrum of Zr. Phys. Rev. A **6**, 871-879.

[43] Laakkonen A, Graeffe G (1987) M X-ray linewidths of gold. J. Phys. (Paris) Colloque C9, **48**, 605-608.

[44] Lábár JL (1987) Effect of relative L-line intensity ratios on the accuracy of standardless X-ray microanalysis. X-Ray Spectrom. **16**, 33-36.

[45] Lábár JL (1991) Effects of non-radiative transitions on the number and depth distribution of generated X-ray photons. X-Ray Spectrom. **20**, 111-117.

[46] Leiro JA (1987) A new measurement of the $L\alpha_{1,2}$ X-ray emission spectrum of Zn and the K emission band of Zn and Ba. X-Ray Spectrom. **16**, 177-179.

[47] Marinenko RB (1991) Standards for electron probe microanalysis. In: Electron Probe Quantitation. Heinrich KFJ, Newbury DE (eds.). Plenum Press, New York, 251-260.

[48] Marion C, Vannier M (1983) Dosage par double mesure au microanalyseur à sonde électronique automatisé (Double X-ray intensity measurement with the automated electron probe microanalyzer). J. Microsc. Spectrosc. Electron. **8**, 31-46.

[49] Maskil N. Deutsch M (1988) X-ray K alpha satellites of copper. Phys. Rev. A **38**, 3467-3472.

[50] Massiot D (1985) Shape comparison of physical spectra: Application to Mossbauer spectra of silicate glasses. J. Non-crystal. Solids **69**, 371-380.

[51] Olsen DK, Moore CF, Richard P (1973) Characteristic L X-ray spectra from proton, α-particle, and oxygen bombardment of Sn. Phys. Rev. A **7**, 1244-1248.

[52] Packwood R (1991) A comprehensive theory of electron probe microanalysis. In: Electron Probe Quantitation. Heinrich KFJ, Newbury DE (eds.). Plenum Press, New York, 83-104.

[53] Packwood RH, Remond G (1992) The interpretation of X-ray and electron signals generated in thin or layered targets. Scanning Microsc. **6**, 367-384.

[54] Parratt LG (1936) $K\alpha$ satellites. Phys. Rev. **50**, 1-15.

[55] Parratt LG (1959) Electronic band structure of solids by X-ray spectroscopy. Rev. Mod. Phys. **31**, 616-645.

[56] Pouchou JL, Pichoir F (1984) Un nouveau modèle de calcul pour la microanalyse quantitative par spectrométrie de rayon X. Partie I: Application à l'analyse d'échantillons homogènes (A new model for quantitative X-ray microanalysis. Part I: Application to bulk specimens). La Recherche Aérospatiale **3**, 167-192.

[57] Pouchou JL, Pichoir F (1991) Quantitative analysis of homogeneous or stratified microvolumes applying the model PAP. In: Electron Probe Quantitation. Heinrich KFJ, Newbury DE (eds.). Plenum Press, New York. 31-76.

[58] Putila P, Juslen H, Graeffe G (1979) High resolution L alpha spectra of indium and tin. Physica Scripta **20**, 41-42.

[59] Randall CA, Parratt LG (1940) $L\alpha$ satellite lines for elements Mo(42) to Ba(56). Phys. Rev. A **57**, 786-791.

[60] Remond G, Campbell JL (1990) Spectral deconvolution of wavelength-dispersive X-ray spectra. In: Microbeam Analysis, 1990. San Francisco Press, 59-66.

[61] Remond G, Giraud R, Packwood RH (1984) The effect of volume and surface diffusion of impurities on the detection limit in microprobe analysis. Scanning Electron Microsc. **1984**; I: 151-166.

[62] Remond G, Coutures Ph, Gilles C, Massiot D (1989) Analytical description of X-ray peaks. Application to L X-ray spectra processing of lanthanide elements by means of the electron probe micro-analyzer. Scanning Microsc. **3**, 1059-1086.

[63] Remond G, Fialin M, Gilles C (1992a) The use of L X-ray spectra of the first series transition elements for quantitative analysis with the electron microprobe. In: Proc. 1992 Annual Meeting Electron Microscopy Society of America. San Francisco Press, 1626-1627.

[64] Remond G, Packwood RH, Gilles C, Chryssoulis S (1992b) Layered and ion implantation specimens as possible reference materials for the electron probe micro-analysis. In: Proc. 1992 Annual Meeting Electron Microscopy Society of America. San Francisco Press. 1652-1653.

[65] Renninger M (1937) "Umweganregung" eine bisher unbeachtete Wechsel wirkungserscheinung be Reumgitterinterferenzen. Zeit Phys. **106**, 141-176.

[66] Roeder PL (1985) Electron microprobe analysis of minerals for rare-earth elements. Use of calculated peak-overlap correction. Canad. Mineral. **23**, 263-271.

[67] Saijonmaa J, Keski-Rahkonen O (1978) Measurement of the electron double ionization cross section of the K shell in Cr and Fe. Phys. Spectra **17**, 451-455.

[68] Salem SI, Lee PL (1976) Experimental widths of X-ray lines. At. Data Nucl. Data Tables **18**, 234-241.

[69] Salem SI, Scott BL (1974) Splitting of the 4d 3/2 and 4d 5/2 levels in rare-earth elements and their oxides. Phys. Rev. A **29**, 690-696.

[70] Salem SI, Hockney GM, Lee PL (1976) Splitting of the 3p levels in the transition elements and their oxides. Phys. Rev. A **13**, 330-334.

[71] Schreiber TP, Wims AM (1982) Relative intensities of K and L shell X-ray line. In: Microbeam Analysis 1982. San Francisco Press. 161-166.

[72] Scofield JH (1973) Theoretical radiative transition rates for K and L shell X-rays. Univ. Calif.

Lawrence Livermore Laboratory Report, UCRL 51326. Livermore, California.

[73] Scofield JH (1974) Relativistic Hartree-Slater values for K and L X-ray emission rates. At. Data Nucl. Data Tables **14**, 121-137.

[74] Self PG, Norrish K, Milnes AR, Graham J, Robinson B (1990) Holes in the background in XRS. X-Ray Spectrom. **19**, 59-61.

[75] Servomaa A, Keski-Rahkonen 0 (1975) K → M_2 radiative Auger effect in transition metals: I. J. Phys. C. Solid State Phys. **8**, 4124-4130.

[76] Solberg TN (1982) Fluorine electron microprobe analysis: variations of X-ray peak shape. In: Microbeam Analysis 1982. San Francisco Press, 148-150.

[77] Srivastava KS (1980) Widths of conduction bands in metals. J. Electron Spectrosc. Rel. Phenom. **20**, 319-322.

[78] Srivastava KS, Srivastava AK, Husain KSM, Singh S (1983) Electron-electron interaction in the X-ray emission spectra of rare-earth elements and their oxides. Indian J. Pure App. Phys. **21**, 256-257.

[79] Tsutsumi K, Nakamori H, Ichikawa K (1976) X-ray Mn Kβ emission spectra of manganese oxides and manganates. Phys. Rev. B **13**, 929-933.

[80] Xu JQ (1990) Estimates of zirconium initial L-vacancy distribution created by 9 keV electrons and L_1-$L_{2,3}$ $M_{4,5}$ Coster-Kronig yields. J. Phys. B. At. Mol. Opt. Phys. **23**, 1423-1432.

Discussion with Reviewers

C. Bonnelle: The line shape of an X-ray peak is intermediate between Gaussian and Lorentzian distributions resulting from the convolution product of the Lorentzian distribution (intrinsic process of emission) with a Gaussian or a near-Gaussian distribution (instrumentation). Your approach, based on a sum rather than a convolution product of two distributions, should be justified.

J.L. Lábár: Equation 7 describes the "hole" in the reflectance of the LiF analyzer crystal as an additive term in the background. Since the reflectance of the LiF affects both the background and the X-ray peaks in the same way and to the same extent, I would prefer a description where the anomalous decrease in the detected intensity were represented by a multiplicative factor {say $F(\lambda,\lambda',\Gamma_H,H_H)$} instead; e.g.,

$$F(\lambda,\lambda',\Gamma_H,H_H) = 1 - H_H \exp\{-(\lambda-\lambda')/\Gamma_H\}^2. \quad (23)$$

A generated spectrum which is a sum of a linear background and peaks modelled with functions such as equation 1 should be multiplied with this factor, and the result should approach the measured spectrum. Would you agree? Why do you apply an additive term

separately to the background?

Authors: Because the instrumental response of a monochromator mounted according to the Johann type is not easily described by a unique analytical expression for a wide range of analyzed wavelengths, we approximated the convolution product describing the line shape of an X-ray peak (equation 10 in **Appendix**) by the sum of two analytical expressions. This approach was used by Phillips and Marlow studying the response of solid-state energy dispersive detectors to high energy mono-energetic incident radiations {Phillips GW, Marlow KW (1976). Automatic analysis of gama-ray spectra from germanium detectors. Nuclear Instruments and Methods **137**, 525-536}. According to those authors the **observed** line shape P(E), as a function of the analyzed photon energy E, can be described by :

$$P(E) = S(E) + D(E) + G(E). \quad (24)$$

The above expression is known as the **Hypermet function** where S(E) represents the Compton scattering of photons within the detector, D(E) expresses the phenomena of incomplete charge collection in the dead layer of the solid-state detector, and G(E) is the major Gaussian peak whose the width is large with respect to the intrinsic width of the diagram line. When using WDS, the line shape of an X-ray peak cannot be simply approximated by a Gaussian distribution. For consistency with the linear combination based Hypermet function, we also used a pseudo-Voigt function (equation 1) for describing the symmetrical diagram line shape assumed to be not distorted by instrumental effects. A summation of two Gaussian distributions has already been used for describing K and L X-ray peaks as illustrated by Salem and Scott [69] and by Salem et al. [70], respectively. The efficiency of an hybrid Gaussian and Lorentzian for describing any X-ray line shape has been demonstrated by Doyle and Shafroth [21] and by Huang and Lim [34] among others. Each function in the linear combination shown in equation 1 is weighted by a coefficient C_g for expressing the intermediate nature between Gaussian and Lorentzian shaped WDS X-ray peaks. The program we used was developed by D Massiot (Centre de Recherches sur la Physique des Hautes Températures, CNRS, Orléans, France). This program has also been successfully applied to the study of Mossbauer spectra [50], indicating that a pseudo-Voigt profile is a **flexible approximation** for describing the line shape of a variety of spectroscopic phenomena.

According to the Hypermet function mentioned above, the asymmetry of peaks resulting from the photon-detector interactions is treated by adding two analytical expressions, S(E) and D(E), to that describing the spectroscopic features. Several expressions for S(E) and

D(E) are available depending upon the analyzed photon energy domain and the type of detectors [12, 13].

As an example, for the experimental and instrumental conditions available with EPMA and SEM equipments, the incomplete charge collection phenomenon dominates the asymmetry of low energy X-ray peaks analyzed by means of a Si(Li) detector. The resulting tailing occurring on the low energy side of an EDS X-ray peak is often described by adding an exponential term to the major Gaussian shape {Fiori CE, Myklebust RL, Gorlen K (1981). Sequential Simplex: A procedure for resolving spectral interference in energy dispersive X-ray spectrometry. In: Energy Dispersive X-ray Spectrometry. Heinrich KFJ, Newbury DE, Myklebust RL, Fiori and CE (eds.). NBS Special Publication **604**, 233-272}.

Although the instrumental distortions are different in origins, the Gaussian offsets we added to the pseudo-Voigt function (equation 1) to describe a WDS X-ray line shape play the role of the S(E) and D(E) functions in the Hypermet function used for describing an X-ray peak analyzed with a solid-state detector. Adding Gaussian or pseudo-Voigt offsets to the major pseudo-Voigt diagram line profile is a sufficient approach to describe a complex peak containing several discrete spectroscopic features, e.g., diagram and non-diagram contribution (satellites, resonant lines). The instrumental distortion is not a discrete phenomenon, so a convolution product of the emission peak with the instrumental factor must be used to **continuously** modify the line profile of all discrete components. Consequently, the additive approach becomes questionable for correcting the asymmetry of peaks resulting from focusing defects. We fully agree with the above comment by Dr. Lábár suggesting that the use of a multiplicative factor rather than an additive term should be preferred for correcting instrumental distortions. Furthermore, the multiplicative factor should be used for correcting instrumental distortions affecting both the emission peak and the continuous emission.

Spectral decomposition procedure based on the pseudo-Voigt function (equation 1) and Gaussian offsets have been shown to be a sufficient approximation for describing WDS X-ray emission bands which are not distorted by instrumental effects. This work will be completed by deriving an analytical expression to be used as a multiplicative factor for correcting the distortions occurring at low Bragg angles as a result of focusing defects by the monochromator. Multiplying pseudo-Voigt profiles with the instrumental correction factor will provide a general fitting function for WDS data processing consistent with the usual procedure used with an EDS.

J.L. Lábár: How many independent variables are used in your fitting procedure? I understand that both the separation and the relative intensities of the α_1 and α_2 lines are fixed. Are the exact position of the α_1 line and the width of both lines also taken from data tables, or are they varied during the fitting procedure together with C_g? Are the position and width of the Gaussian offset also independent parameters in the fit if an offset is required? How do you determine these parameters? Is there an automatic search criterion or is it done manually by trial and error?

J.L. Pouchou: In the fitting procedure you fixed as coupled variables the α_2/α_1 intensity ratios for K, L and M lines using values derived from data tables. Are these values known with sufficient accuracy, taking into account the absorption effect and the influence of excitation at low overvoltage?

Authors: The peak position, peak width, and peak height are the **variables** of the Gaussian and the Lorentzian distributions in equation 1 used for describing each feature present in the observed emission band. The shape of each feature is determined by the value of the parameter C_g in equation 1, this value being kept as a constant during the fitting procedure. A first estimate of the C_g value is obtained by manually adjusting this parameter in order to obtain a satisfactorily subjective description of the low energy valley (long wavelength valley) of the peak assumed to be free of satellites and not to be distorted by instrumental effects. After all variables have been selected, a first fit is performed starting with the estimated C_g value. The fitting procedure is repeated by slightly varying the C_g value apart the first estimate in order to obtain the best quality of fit (equation 2). A typical situation requires the use of two pseudo-Voigt profiles (α_1 and α_2 components), two pseudo-Voigt or Gaussian offsets (asymmetry of peaks) and two parameters for the linear variation of the continuum intensity so that an average of fourteen variables are necessary for modelling the observed peak shape. For the α_1 and α_2 diagram bands, some variables can be coupled together, i.e., the peak positions, the peak widths, and the intensity ratios. The α_1 and α_2 peak widths are kept equal and set as coupled variables in the pseudo-Voigt profiles associated with the α_1 and α_2 components.

Before starting the data acquisition procedure, the spectrometers are initialized by analyzing an andradite specimen ($Ca_3Fe_2(SiO_4)_3$). The observed peak position for the Fe Kα, Ca Kα, Si Kα, and O Kα emission peaks are set to their theoretical peak positions initializing the LiF, PET, TAP and W/Si monochromators, respectively. After the spectrometers have been initialized, the measured peak positions for other elements are found to be consistent with their theoretical values, at least for X-ray peaks occurring at Bragg angles greater than 30° (the difference between the observed and theoretical data

is less than $5 \cdot 10^{-5}$ of the corresponding $\sin\theta$ value). Larger differences between measured and theoretical positions are frequently observed when analyzing strongly asymmetrical peak, e.g., $L\alpha$ lines of high Z elements using the LiF monochromator whose the peak distortion is dominated by instrumental factors (see Fig. 3). The theoretical α_1 and α_2 peak positions are used as a first estimate in the fitting procedure, these two values being kept as **coupled variables**, i.e., the calculated positions may differ from the theoretical values but the calculated ($\alpha_2 - \alpha_1$) distances remain equal to the theoretical distances. We verified that the calculated α_1 and α_2 peak positions remained within an uncertainty of about $5 \cdot 10^{-5}$ of the theoretical $\sin\theta$ values when using the theoretical or observed peak positions as first estimates in the fitting procedure.

In most cases, the uncertainty in calculated intensities derived from the experimental spectra has been shown to mainly depend on the choice of the C_g value modifying the shape of the peak tails and consequently the intensities of the pseudo-Voigt profiles. As a first estimate of the $\alpha2/\alpha1$ intensity ratios, we used data available in the literature [17, 18, 22]. We verified that keeping these estimated values as coupled or independent variables in the fitting procedure led to consistent calculated intensities. In the absence of a better knowledge for the response function of the monochromators, our fitting function cannot provide intensity ratios with a better accuracy than that of the nominal values given in most of the practical data tables available to the EPMAs users (see for example [22]).

For non-diagram bands, i.e., high energy satellites and instrumental distortions, all parameters involved in the offsets are kept as variables. Again the uncertainty in the tail shape resulting from focusing defects due to the monochromator led to a purely empirical choice for the C_g value to be used in equation 1. For asymmetrical shapes dominated by instrumental distortions (Bragg angles lower than 30°), data in the present study showed that a high energy Gaussian offset led to a better quality of fit than that obtained with a pseudo-Voigt offset. However, the addition of a Gaussian offset is only a mathematical solution treating the instrumental distortion as a spectroscopic feature and as mentioned above a correction based on a multiplicative term continuously modifying the shape of the emission band will be preferred.

For asymmetrical shapes dominated by high energy satellite bands (Bragg angles > 30°), it has been shown in the present study that the quality of fit only slightly changed when describing the high energy features with Gaussian offsets or with pseudo-Voigt profiles similar to those describing the parent diagram emission bands. We empirically verified that the best quality of fit was
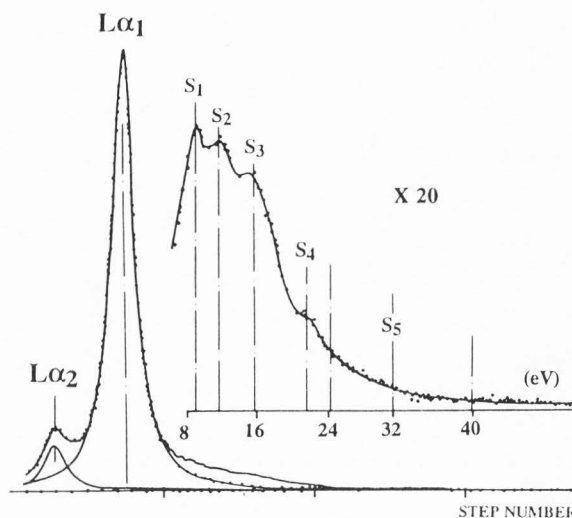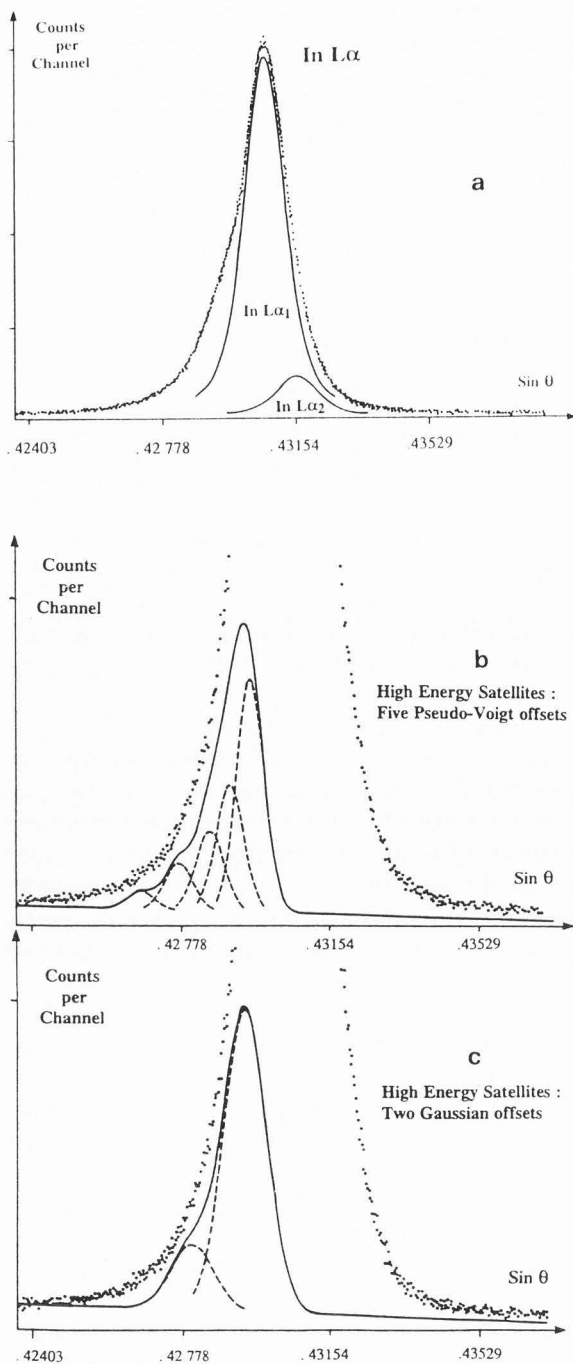

Figure 33. High energy resolution measurement of the In $L\alpha_{1,2}$ emission band carried out by Putila *et al.* [58].

---

obtained by keeping the width of the Gaussian offsets as **coupled variables** in the fitting procedure. When satellites and instrumental factors contributed simultaneously to the observed asymmetry (Bragg angles near 30°), the widths of the high energy offsets were kept as **independent variables**. In such a case, it was not possible to separate both effects, satellites versus instrumental factors

Because of the energy resolution of the monochromators used, only the **envelope** of satellites were detected. In the present work, two Gaussian offsets were added to the major pseudo-Voigt function for describing high energy satellites to $L\alpha$ emission lines. The effect upon the measured intensities, of the number of offsets used for describing the high energy tail is illustrated below for the case of the In $L\alpha_{1,2}$ peak emission band. As shown in Figure 33 (reprinted from Putila *et al.* [58]), four distinct high energy satellites have been detected distant by 8 eV, 12 eV, 16 eV, 22 eV, and a tail centered near 35 eV, from the In $L\alpha_1$ diagram line.

The In $L\alpha_{1,2}$ emission band was analyzed with a PET (002) monochromator (Fig. 34a). The C_g parameter was set equal to 0.55 in equation 1 describing the In $L\alpha_{1,2}$ diagram band. Consistent with the results in Figure 33, four Gaussian offsets of equal width were added to the high energy side of the peak. The maximum positions of the Gaussian offsets were kept as **coupled** variables so that their distances from the diagram line position remained equal to the energy separation distances between the S_1, S_2, S_3 and S_4 peaks and the In $L\alpha_1$ peak derived from the high energy measurements shown

in Figure 33. The difference between the calculated and the measured In $L\alpha_{1,2}$ spectra revealed the existence of a possible additional feature which may correspond to the tail marked S_5 in Figure 33. The quality of fit was obviously improved by adding a fifth Gaussian offset (Fig. 34b). However, as shown in Table 14, the very low intensity of this feature did not change appreciably the intensity of the total satellite band with respect to that derived from the fit with four offsets. As shown in Table 14, higher intensity ratios were calculated when five pseudo-Voigt offsets having a C_g value equal to that of the pseudo-Voigt shape of the parent diagram line was used instead of five Gaussian shaped profiles. This result demonstrates once again the importance of the C_g value to be used in the fitting function, i.e., the crucial need for a better knowledge of the instrumental response function.
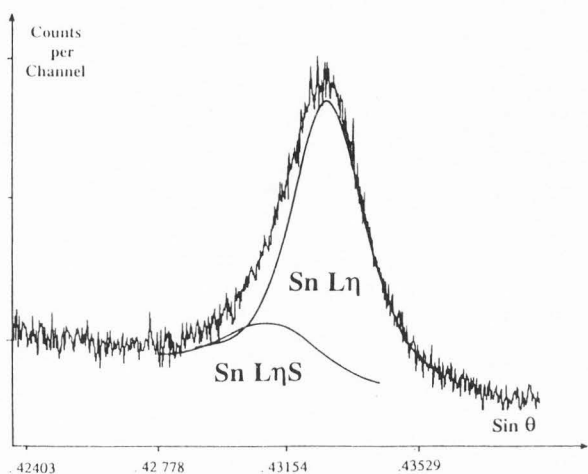
A detailed description of the fine structures to the high energy satellite bands is not available for all X-ray emission lines, and in most cases, it is not realistic to add a large number of high energy offsets as illustrated above for the case of the In $L\alpha_{1,2}$ emission band. In practice, because the energy resolution of the monochromators allows us to detect only the **envelope** of the satellite bands, **two Gaussian offsets** were empirically added to the pseudo-Voigt diagram emission band (Fig. 34c). As shown in Table 14, the relative intensities of the satellite lines described by two Gaussian offsets were in good agreement with the value derived from the fit based on five features having the same shape than that of the diagram line. This example illustrates empirically that our approach based on **Gaussian offsets** added to the **pseudo-Voigt fitting function** (equation 1) is a sufficient approximation for WDS spectral **decomposition** applied to quantitative analysis with the EPMA.

J.L. Lábár: An anomalous "hole" in the detected continuous intensity is described for a LiF analyzer crystal. Has a similar phenomenon also been observed for other X-ray reflector crystals (TAP, PET, etc.)?
Authors: The presence of the "hole" in the continuous emission was shown by many EPMA laboratories involved in the analysis of gold present at trace levels in a variety of minerals. Investigations on possible origins of the "hole" have been performed for the LiF (200) monochromator used for the analysis of the Au $L\alpha$ emission line. The more detailed analysis of "hole" positions resulting from multiple reflections within the LiF monochromator based on equation 22 has been discussed by Self *et al.* [74]. To our knowledge, no similar calculations have been performed for other monochromators. In our present work, no systematic measurements were made for detecting possible "holes" in the continuous emission analyzed with PET and TAP monochromators.

Figure 34. (a) In $L\alpha_{1,2}$ emission band obtained with a PET (002) monochromator (Johann mounting); (b) calculated high energy satellites described by five pseudo-Voigt profiles of equal widths and having the same energy separation distances than those indicated in Figure 33 for the S_1, S_2, S_3, S_4 and S_5 features from the In $L\alpha_1$ line; and (c) high energy satellites described by two Gaussian offsets of equal width.

Table 14. High energy satellite to the total In $L\alpha_{1,2}$ intensity ratios as a function of the fitting parameters.

Number of high energy offsets	Cg value in the pseudo-Voigt function (equation 1)		I(satellite) / I(InL$\alpha_{1,2}$) per cent
	Diagram line	Satellite bands	
4	0.55	1.00	15.50
5	0.55	1.00	15.60
5	0.55	0.55	17.90
2	0.55	1.00	17.80

Figure 35. Sn Lη emission band analyzed with a PET (002) monochromator.

J.L. Pouchou: In the present state of your expertise in this field, what would be your recommendations about the features that a good general purpose analysis program should include? Could you summarize which particular approach should be adopted in every typical case? **Authors:** As discussed by Fialin *et al.* [26], WDS quantitative analysis with the EPMA based on the peak height and peak area measurements are two complementary rather than competitive approaches for obtaining X-ray intensity values which are proportional to the number of emitting atoms. However, peak areas obtained by summing the number of counts measured by stepping the monochromators may cease to be applicable when chemical shift and strong self-absorption phenomena alter the shape and the intensity of an emission band. **Spectral decomposition** must also be used in presence of instrumental distortions as illustrated in text for the case of the analysis of gold (Au Lα) at trace levels. X-ray spectra processing, based on multiple least-square fitting techniques using theoretical reference spectra, should also be preferred to resolve peak overlaps rather than the use of predetermined correction factors. Such
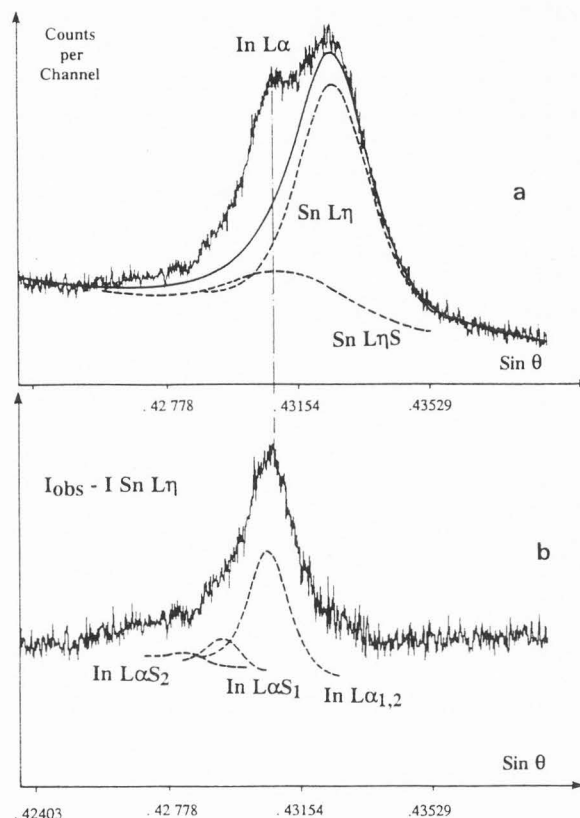
Figure 36. (a) Results of fit to the overlapping In Lα and Sn Lη emission bands measured at the surface of an indium bearing SnO_2 crystal; and (b) calculated In L$\alpha_{1,2}$ emission band extracted by subtracting the Sn Lη intensity from the total observed intensity.

----

a need for spectral decomposition procedure is illustrated below for the case of the analysis of indium bearing cassiterite minerals (SnO_2). The asymmetrical In L$\alpha_{1,2}$ emission band overlaps the Sn Lη line (L_2-M_1 transition) which has been also found to be asymmetrical as shown in Figure 35. Spectral decomposition of the complex emission band resulting from the In L$\alpha_{1,2}$ and Sn Lη components measured at the surface of a SnO_2

specimen, containing In at trace levels, is illustrated in Figure 36. In the present state, we used the spectral decomposition procedure to calculate correction factors to be applied to the experimental concentrations derived from the usual peak height measurement procedure. In the future, we hope to use on-line digital data acquisition and spectral decomposition procedures in order to process WDS spectra according to a least-square fitting technique using theoretical spectra as for the case of EDS spectra. For this purpose, there is a need for an accurate data base of Coster-Kronig transition probabilities and relative intensities of the X-ray lines in order to predict the shape and intensity of absorption free X-ray spectra of pure elements. However, as discussed above, the major difficulty in generating synthetic WDS spectra still lies in the absence of an accurate analytical description of the response function of the monochromator and more particularly, for the case of multilayer structures used for the analysis of soft X-rays.